MONASH University

# Computational modelling of Nano-resonators and coupled gain media

Warnakula Arachchiralalage Don Anton Tharindu Kumar Warnakula
BSc Eng (Hons)

A thesis submitted for the degree of Doctor of Philosophy at Monash University in year 2019

Department of Electrical and Computer Systems Engineering

# Summary

THe field of plasmonics, with its promise of nano-scale control of almost every aspect of our life, hides possibly the greatest potential to revolutionise the technology that drives modern society. From the incredibly accurate and minute sensing and imaging schemes to nano-scale control of electromagnetic fields, the possibilities of the technology is beyond most of our wildest imaginations. However, almost all of these possibilities are shrouded under the cloak of quantum mechanics; the physics of small things. While classical theories of physics are complex enough themselves, quantum mechanical theories are(sometimes quite literally), infinitely more complex. Hence some of our understanding of plasmonic systems and gain elements coupled to them, need to be derived from within numerical studies. This thesis is dedicated to building numerical methods to analyse and also actually analysing such plasmonic systems. In this thesis, we strive answer questions like, what happens to the surface plasmons living on a cylinder, when we fold it into a torus?; what happens to the electromagnetic field when two spheres with plasmons living on them are brought together?; what is the most efficient way to solve problems involving plasmons accounting for all quantum phenomena?, and a host of others. It is the author's humble attempt at pushing the boundaries of our knowledge on the behaviour of the elusive surface plasmons and their peculiar quantum effects.

# General Declaration

This thesis contains no material which has been accepted for the award of any other degree or diploma at any university or equivalent institution and that, to the best of my knowledge and belief, this thesis contains no material previously published or written by another person, except where due reference is made in the text of the thesis.

_____

Tharindu Warnakula

October 2019

# Publications During Enrollment

- Tharindu Warnakula, , Mark I. Stickman and Malin Premaratne. **Improved scheme for modeling a spaser made of identical gain elements.** JOSA B 35(6), 1397-1407, 2018.

- Tharindu Warnakula, Sarath D. Gunapala, Mark I. Stockman and Malin Premaratne. **Cavity quantum electrodynamic analysis of spasing in nanospherical dimers.** Phys. Rev. B 100(8), 085439, 2019.

- Tharindu Warnakula, Sarath D. Gunapala, Mark I. Stockman and Malin Premaratne. **Broken poloidal symmetry and poloidal plasmonic modes on tori** - Accepted for publication at Phys. Rev. B.

# Acknowledgements

Firstly, I would like to express my wholehearted gratitude to my Ph.D. supervisor and mentor, Prof. Malin Premaratne for all his support, kindness, encouragement and for believing in me throughout this journey, without whose timely guidance this thesis would not have been possible. I sincerely could not have asked for a better supervisor.

I would also like to express my gratitude to members past and present who helped me grow from a fresh-faced graduate in 2016 to the submission of my thesis. In no order, I would like to thank Dilusha, Chathurangi, Charith, Ashan, Sudaraka, Harini, Lakshitha, Champi, Dasuni, Viraj, Nisal, Kamani, Asha, Ravi, Tharaka and Sachinthana for being awesome colleagues and friends.

I sincerely acknowledge Monash University for providing me with all the support, facilities and financial assistance needed throughout my candidature. I would also like to thank all staff members including Ros, Emiliy, Maria and Geoff at the Department of Electrical and Computer Systems Engineering for their support throughout my Ph.D.

I would also like to thank my aunts and uncles in Melbourne and my cousins who made my time here homely and colourful. I would like to thank Charissa for her support and love through the past 2.5 years. Without her encouragement, this document would have been far less than it is. Last, but certainly not least, I'm much indebted to my beloved parents Kumar and Anusha Warnakula, sister Thilini for their unconditional love, understanding, and support.

This thesis is dedicated to my parents Anusha and Kumar, the strongest people I know. They say good times create weak men. I will work hard to prove that wrong for the sake of the good times you have given me.

# Contents

# List of Figures

# Chapter 1
# Introduction

## 1.1 Background and Motivation

The main constitutive element of any plasmonic systems is the plasmonic resonator; the object on which the plasmonic oscillations take place. Based upon applications, the plasmonic system may interact with additional gain media placed in proximity. In the earliest descriptions of plasmons and their applications, the plasmon resonators and the gain media interacting with them, were treated as classical physical objects and the treatments amounted to basic mean field theories. These theories, based on the requirements of the times with respect to accuracy and precision, were adequate for a long time. However, due to the extremely small length scales of the plasmonic resonators and the increasing demand for more precise characterisation on plasmonic systems, the quantum mechanical descriptions of plasmonics systems have become not only desirable, but absolutely mandatory for certain systems. Systems intimately dealing with light at the nano or micro length scales such as, quantum computing setups [1,2], photonic-plasmonic circuits [3,4], chemical and biological sensing systems [5,6], and energy harvesting systems [7,8] have seen vast improvements due to the increasing understanding of the quantum rules that govern them. In this thesis, I aim to contribute to the global effort by researchers the world over in developing the required tools to analyse plasmonic nano-resonators and coupled gain media,

and to use these tools and numerical techniques to study the behaviour of such systems.

## 1.2 Research Aims

**Studying the response of hybridized plasmonic systems coupled to gain media**

In this stage, we aim to focus on the so-called hybridized plasmonic setups, which are systems comprising multiple spatially separated plasmonic resonators interacting through their near field electromagnetic forces. We plan to take the nanospherical dimer spaser as the simplest example of such systems and analyse its behaviour in the presence of gain media chromophores. We aim to perform the analysis semi-analytically to allow for physical intuition and to allow for future extension into much more complex hybridized plasmonic systems using the same techniques and equations we develop.

**Studying the plasmonic response of nano-tori**

In this stage, we aim to study the complete plasmonic response of a nano-torus. The torus nanoparticle has been used extensively in recent years due to their high tunability and field confinement properties as compared to spherical nanoparticles. While the spherical nano-particle and its plasmonic response is extremely well understood, the torus, as a nanoresonator, is still not understood completely. Almost all studies of the torus have focused on the so-called toroidal modes ignoring the poloidal modes structure. We will study the poloidal modes on the torus and the associated symmetries and broken symmetries and their effect on the modes generated. Through this, we aim to complete the total characterisation of plasmonic modes on a torus particle.

**Development of an exact and efficient quantum solver for the coupled resonator and identical emitter model**

In this stage, we aim to develop the most efficient solver currently available for solving the quantum model describing the interactions of a resonator with identical emitter chromophores. The quantum description of such systems are known to be extremely complex due to the exponential scaling of dimensions of problem. We plan to use symmetries within the quantum equations to simplify the complexity and also use the most efficient data structures and algorithms to build an efficient shared-memory parallelised solver that reduces the computational complexity of solving such problems by orders of magnitude. We also plan to use the solver as a tool for making predictions regarding the behaviour of certain quantum systems that have been inaccessible to exact calculation up to now.

## 1.3 Thesis Outline

This thesis comprises 10 chapters which are organized as follows:

Chapter 1 introduces the thesis and presents the background and motivation for the research problem tackled along with the research aims.

Chapters 2, 3 and 4 are then designed to allow the reader a glimpse into the analytical tools used in characterising plasmonic systems. Chapter 2 gives a short overview of surface plasmons as a physical phenomenon. Starting with a brief review of history, we discuss the main types of surface plasmon phenomena. Chapter 3 discusses the oldest and most well-known plasmonic structure: the sphere, and its plasmonic response. We discuss the various methods used to study such structures and present the analytical derivation. In Chapter 4, we discuss the phenomenon of plasmon hybridization and derive the relevant analytical results regarding plasmons modes on a nanopsherical dimer.

In Chapter 5, we present our results on the structure of the poloidal modes of

a toroidal nanoparticle. We also show the complete structure of the modes on a torus.

In Chapter 6, we take a detour to introduce the concept of spasing and its importance in the field of plasmonics. We establish the spaser as the quintessential nanoresonator-emitter model in the plasmonic regime.

Chapter 7 presents the results on the quantum nanresonator-emitter solver we develop. We start off with background on the quantum description of such systems and delve deep into the efficiency improvement we made by utilising a symmetry hidden within the equations.

In Chapter 8, in anticipation of Chapter 9, we present the quantization technique for hybrid plasmon systems. We specifically quantize the lowest order modes of the nanospherical dimer and also derive the coupling strengths between them and emitter chromophores. Using the quantization we perform, in Chapter 9, we present the complete model of the nanospherical dimer based spaser. We present and compare spasing output for various dimer configurations and separation distances. Finally in chapter 10, we summarize the research contributions of the thesis and outline the prospective future research stemming from these contributions.

# Chapter 2

# Surface Plasmons

Figure 2.1: The Lycurgus cup made of dichroic glass by the ancient Romans. In daylight, when light is reflected off the cup, it appears in green, whereas when light is shone within the cup and transmitted through the glass, it appears in red. Image available under the Creative Commons Attribution 2.5 Generic license.

## 2.1 History of surface plasmons

Surface plasmons are excitations in the free electrons within a material, at the material interface with an external medium. These excitations, which are essentially oscillating charge waves, create electromagnetic fields near the interface. This phenomenon was predicted by Rufus Ritchie in 1957 [9] and since then, the field of study concerned with the manipulation of these oscillating charges has grown by leaps and bounds, and is today known in general as plasmonics. The most interesting effects of plasmons are usually detectable in the micro- and nano-scale when the charge oscillations are confined to length scales much smaller than the wavelength of the associated electric fields. The resonance frequency of these charge waves actually dictate the interactions of the plasmons with external fields. The resonance frequencies in turn are dictated by the properties of the material supporting the plasmon oscillations. For noble metals like silver and gold, the frequencies lie in the visible region of the electromagnetic spectrum, making them useful for a great range of applications.

Historically, however, there exist evidence of palsmonic effects being sued inadvertently in many settings. One such example, the Lycurgus cup, is shown in Fig. 2.1. This cup is made of a dichroic glass, which is glass dispersed with gold and silver nanoparticles. When light is incident on the cup at different angles, the visible color is altered depending on whether the nanoparticles were excited or not. When excited, the nanoparticles will absorb a certain portion of the incident light spectrum, altering the visible color.

There are three main manifestations of the plasmonic effects in materials: the localised surface plasmons, surface plasmon polaritons, and surface lattice resonances. In the next section, we will briefly discuss these forms of existence of plasmons.

## 2.2 Modes of existence of surface plasmons

### 2.2.1 Localised Surface Plasmons(LSP)

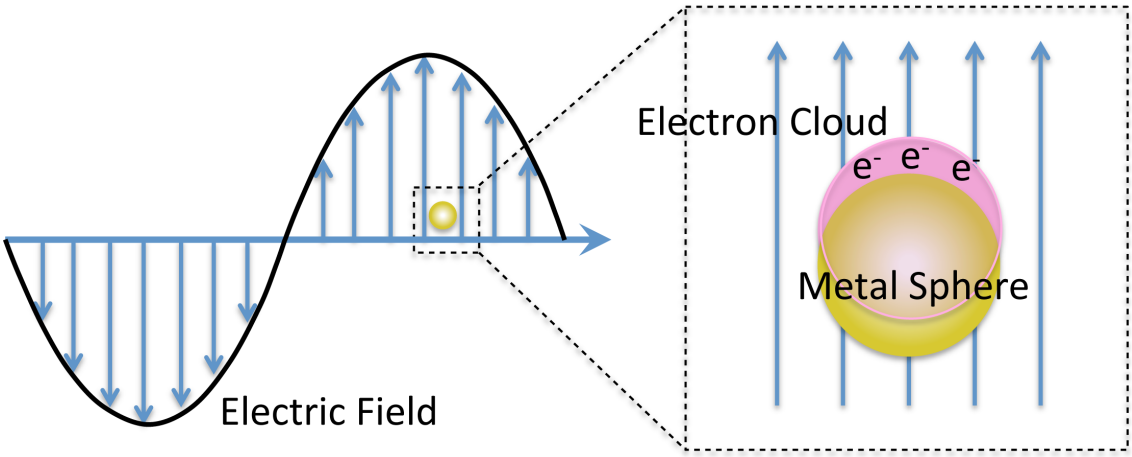


Figure 2.2: The form of localised plasmon resonances on a spherical nanoparticle under the influence of a sinusoidal external electric field excitation. Image available under the Creative Commons Attribution-Share Alike 4.0 International license.

The localised surface plasmon is the purest form of the plasmons. They are the general localised excitations of the oscillating electron waves at the surface of a nanoparticle. The oscillations take place perpendicular to the surface of the particle and there is no lateral movement. These can be excited by any form of appropriate energy transfer such as electron beams or electric fields.

### 2.2.2 Surface plasmon polaritons(SPP)

These are the travelling wave counterparts of the surface plasmons. They form waves travelling along the surface of plasmonic particles. These waves are evanescent in nature and dissipate quite rapidly. As shown in Fig. 2.3, the waves travel along the surface through the excitation by electrons or an electric field(photons). However, if photons are to be used, special structures such as the Kretschmann

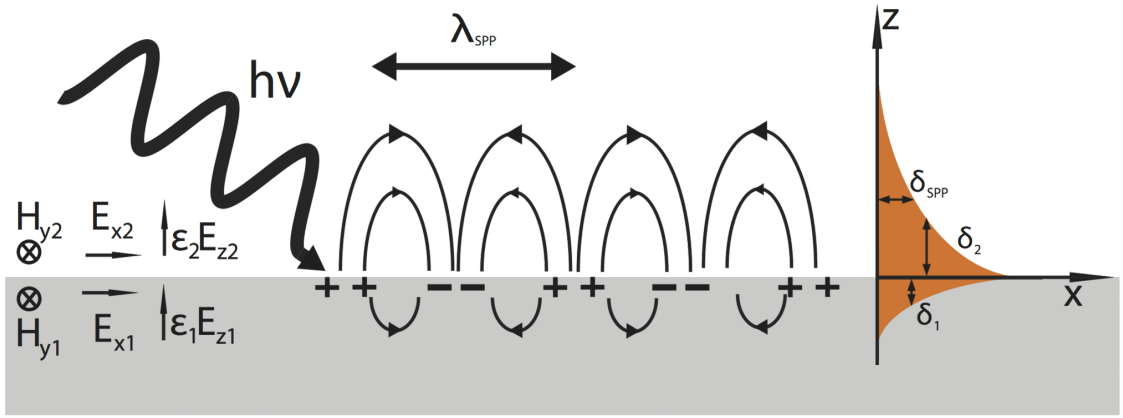


Figure 2.3: Surface plasmon polaritons may be excited by photons as shown. The graph on the right plots the penetration depth of the electric field into the material and the external environment. The field dissipates rapidly along the surface.

arrangement [10] needs to be used to accommodate the momentum mismatch between photons and plasmons. Also shown in the figure distribution of the electric field within the material and the external medium. As can be seen, the electromagnetic field extends further into the external medium as compared to the material.

### 2.2.3 Surface lattice resonances(SLR)

Surface lattice resonance is a relatively new phenomenon that makes use of the constructive interference effects of plasmonic particles [11]. Plasmonic particles placed in a lattice with lattice separation at the order of the wavelength of the generated electromagnetic field has been shown to exhibit extremely narrow and intense plasmonic resonances. This structure has enabled the construction of high-resolution sensors and extremely coherent and narrow lasing sources.

# Chapter 3

# Surface plasmon resonances on a sphere

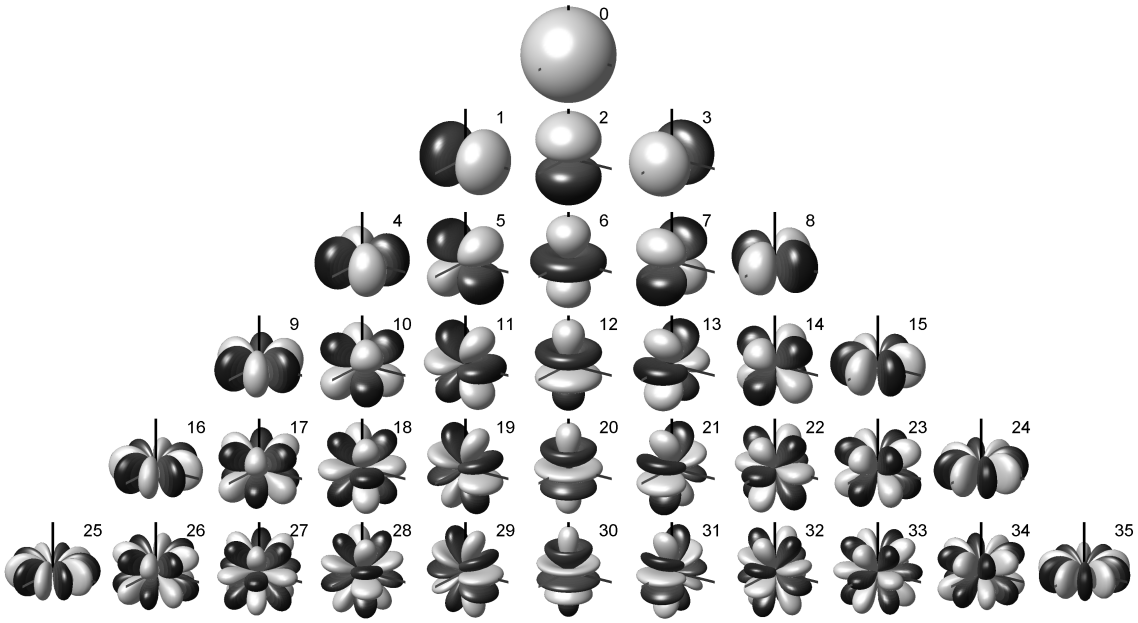


Figure 3.1: Illustration of the spherical harmonics ladder. Note that the plots indicate the angular distribution of charges on a sphere. The white portions indicate positive charges while the dark portions are negative charges. Image made available under the Creative Commons Attribution-Share Alike 3.0 Unported license by Dr. F. Zotter.

Given the importance of the applications of the surface plasmons and associated phenomena, the question of studying the surface plasmon behaviour in different nano-particles became a very important question. The simplest of all

particles, the spherical particle was the central structure of interest. However, as it turned out, the problem of surface plasmon behaviour and the scattering characteristics were effectively solved roughly half a century before the existence of surface plasmons were postulated. The complete solutions are know to be the so-called Mie solutions of Maxwell's equations.

Gustav Mie solved the question of the interaction between a dielectric sphere and a plane wave in 1908 [12]. He was able to derive analytical expressions for the scattering, absorption and extinctions taking place along with the associated cross sections. As it turns out, for dielectrics with negative real parts of permittivity at the frequency of incident light, the extinction peaks correspond exactly to the resonance frequencies of surface plasmon modes on a sphere. This provided an excellent basis for the initiation of the study of surface plasmon spectra on spheres and similar objects.

## 3.1 The Mie solution of the sphere

In the quasi-static approximation, the scalar electric potential $\Phi$ can be calculated through the Laplace equation as,

$$\nabla^2 \Phi = 0. \tag{3.1}$$

This equation was solved by Mie for a particle of radius $a$, under an electric field $\mathbf{E} = \mathbf{E_0}\hat{\mathbf{z}}$ in the $z$ direction. Given that $\epsilon$ is the dielectric constant of the particle and $\epsilon_b$ is the dielectric constant of the background medium, the general solution in spherical coordinates is exactly separable and can be given as(see Appendix A),

$$\Phi(r,\theta,\phi) = \sum_{l=0}^{\infty} \sum_{m=-l}^{l} \left[ A_l^m r^l + B_l^m \left(\frac{1}{r}\right)^{l+1} \right] Y_l^m(\theta,\phi) e^{im\phi}, \tag{3.2}$$

where the coefficients $A_l^m$ and $B_m^l$ are determined by boundary conditions and $Y_l^m(x)$ are the spherical harmonics. The terms in the summation are often referred to as the solid harmonics. The $r^l$ terms correspond to the solutions inside the sphere while the $r^{-l}$ terms correspond to the potential outside the sphere. This solution is sometimes represented in terms of the so-called associated Legendre polynomials $P_l^m$,

$$Y_l^m(\theta,\phi) = (-1)^m \sqrt{\frac{(2l+1)}{4\pi}\frac{(l-m)!}{(l+m)!}} P_l^m(\cos(\theta)) e^{im\phi}. \tag{3.3}$$

The form of the spherical harmonics is represented as angular plots in Fig. 3.1. Each row of the figure corresponds to different $l$ values while the m values vary along the rows. Using the boundary conditions pertaining to the incident field $\mathbf{E} = \mathbf{E_0}\hat{\mathbf{z}}$, the solutions can be shown to be of the form,

$$\Phi(r,\theta) = \begin{cases} -\frac{3\epsilon_b}{2\epsilon_b+\epsilon} E_0 r\cos(\theta), & \text{for } r < a \\ \frac{\epsilon-\epsilon_b}{2\epsilon_b+\epsilon} a^3 E_0 \frac{1}{r^2}\cos(\theta) - E_0 r\cos(\theta), & \text{for } r \geq a \end{cases} \tag{3.4}$$

Looking at the form the potential for $r \geq a$, we can derive the form of the dipole moment of the particle as,

$$P = \frac{\epsilon-\epsilon_b}{2\epsilon_b+\epsilon} a^3 E_0. \tag{3.5}$$

This form of the dipole moment then allows for the determination of the scattering and absorption cross sections and other quantities such as the sphere polarizability $\alpha$,

$$\alpha = \frac{\epsilon-\epsilon_b}{2\epsilon_b+\epsilon}. \tag{3.6}$$

This polarizability allows for the expression of the dipole response of a spherical particle to incident electromagnetic radiation simply as,

$$P = \alpha a^3 E_0. \tag{3.7}$$

## 3.2 Surface integral formulation and the surface plasmon modes on a sphere

While the Laplace equation and the associated boundary value problem has been the main tool in analysing the surface plasmon modes on structures, there is an alternate integral formulation of the boundary value problem that implicitly incorporates the boundary conditions into the problem. This method uses the so-called Neumann-Poincare operator. First proposed by Poincare [13] and Neumann [14] in the context of an extremal value problem, the NP operator has recently received much attention in plasmonics as a convenient alternative to the Laplace equation based methods [15]. The surface charge plasmonic modes of a bounded structure occupying the domain $\Omega$ in $\mathbb{R}^3$ and bounded by $\partial\Omega$ with surface elements $\sigma$ are described as eigenfunctions of the Neumann-Poincare operator,

$$\mathcal{K}^*[\phi](\mathbf{x}) = p.v.\frac{\lambda}{2\pi}\int_{\partial\Omega}\frac{(\mathbf{x}-\mathbf{y})\cdot\nu_{\mathbf{x}}}{|\mathbf{x}-\mathbf{y}|^3}\phi(\mathbf{y})d\sigma(\mathbf{y}). \tag{3.8}$$

The resonant permittivities $\epsilon$ are related to the eigenvalues $2\pi/\lambda$ of the operator as,

$$\lambda = \frac{\epsilon - \epsilon_b}{\epsilon + \epsilon_b}. \tag{3.9}$$

$\epsilon_b$ is the permittivity of the surrounding space($\mathbb{R}^3 \setminus \Omega$). It is known that the spectrum of the operator in a smooth domain is real, discrete and that $\lambda = 1$ is one of the eigenvalues. All other eigenvalues have $|\lambda| > 1$ [15]. If we let $\omega_C$ be the frequency at which $\mathrm{Re}\{\epsilon\} = -1$ of the plasmonic medium, then positive eigenvalues correspond to resonance frequencies $\omega < \omega_C$ and negative eigenval-

ues correspond to frequencies $\omega > \omega_C$. We use the subscript $C$ here since it is at that very frequency that the transverse plasmonic modes of an infinite cylinder are located.

In this formulation, the surface charge eigenfunctions are known to be furnished by the spherical harmonics $Y_l^m(\theta, \phi)$ with eigenvalues $\lambda = (2l + 1)$. The modes with same $l$ value have the same frequency. The $Y_1^m$'s form the three dipole active modes in the three independent directions while the $Y_2^m$'s form the five quadrupoles and similarly for other higher order multipoles on the sphere.

# Chapter 4

# Surface plasmon resonances on nano-spherical dimers

Nano-spherical dimers are one of the first of the so-called hybrid structures to be analysed in plasmonics. The effects of spatial proximity of particles supporting plasmons have been of considerable interest and the unique properties of such systems have been used in many applications. Plasmonic resonators placed close to each other have been known modify each other's plasmonic response by mainly shifting the resonance frequencies. The proximity of the resonators also result in a confinement effect which tends to confine the electromagnetic fields of the resonators in the space in between the two resonators. This concentration of electromagnetic energy in turn is useful in a wide range of applications such as imaging systems [16], sensing [17] and many others. The theoretical study of plasmon responses of nanospherical dimers was pioneered by Nordlander and colleagues [18] and they managed to show how the modes can be conveniently expressed as hybridized single sphere modes. In this chapter, we study the structure and form of these modes. While we will not delve deep into the exact analytical expressions, we will derive an alternative convenient formulation based on the dipole moments and polarizabilities of individual nanospheres.

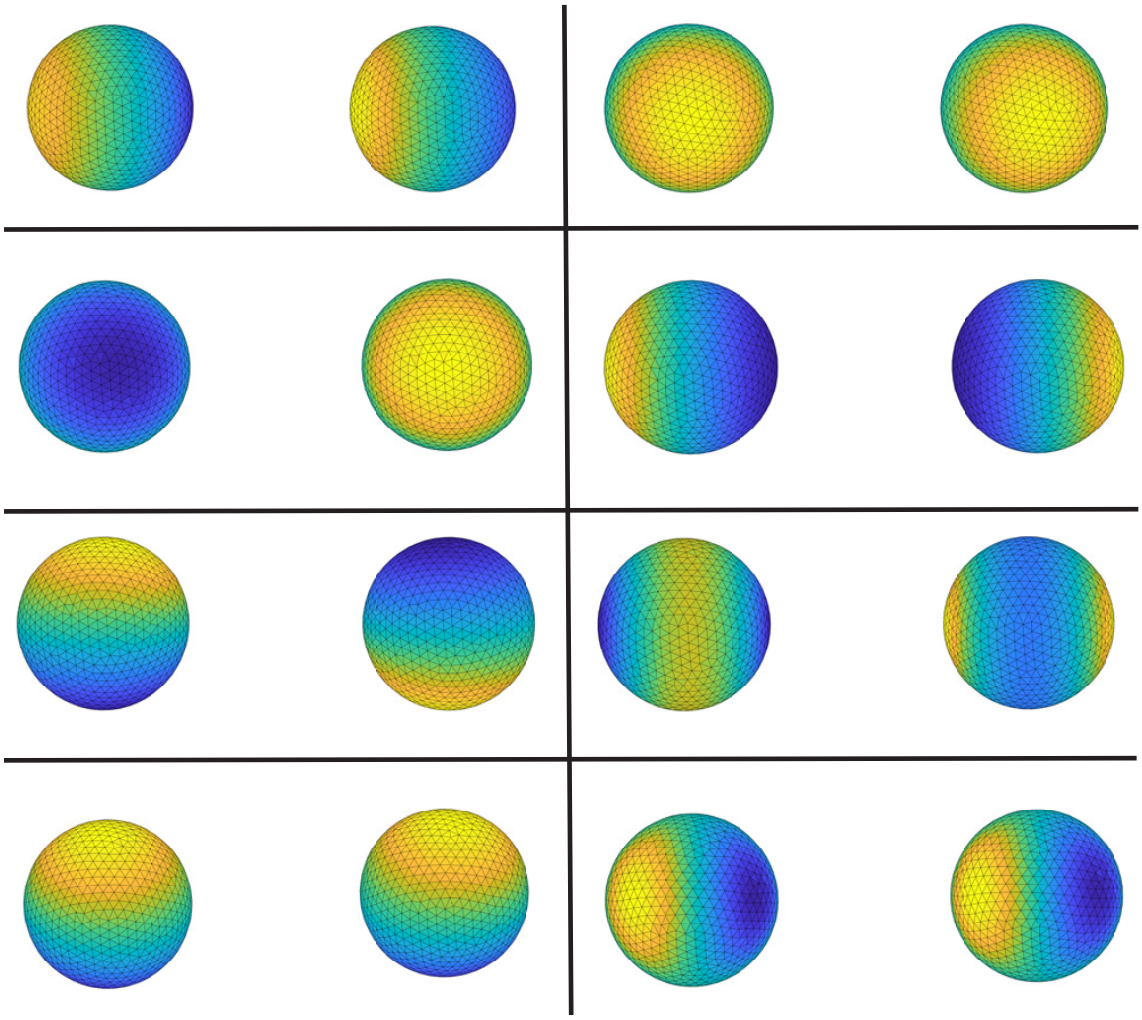

Figure 4.1: Illustration of the 8 lowest order modes on a nanospherical dimer. The radii of the spheres is $R = 10\,\text{nm}$ and the separation between the centers $D = 40\,\text{nm}$. Note that of the first six modes, only 4 are independent due to symmetry. These are also exactly modes that can be shown to result from the hybridization of the singlet nanosphere dipole charge modes.

## 4.1 The plasmon modes on nanospherical dimers

We can solve the Laplace equation or the NP operator equations to derive the plasmon modes on spherical dimers, in the exact same way we derived the form of the plasmon modes of a singlet nanosphere in chapter 3. The lowest order surface charge modes are shown in figure 4.1 for nanosphere dimers of radius

$R = 10\,\text{nm}$ at separation $R = 30\,\text{nm}$. While solutions can be presented in terms of the usual solid harmonics, the equations and expressions derived are extremely complex and rarely useful.

However, a much more useful approach has been made possible by the plasmon hybridization method [18]. The plasmon hybridization method has shown that, to a good approximation, the modes of a dimer may be shown to be modes formed by the interaction and hybridization of modes on single spheres. For example, the lowest order modes may be seen as arising out of the interaction of the lowest order dipole modes on a sphere. Due to the symmetry present, the 3 dipole modes on each sphere hybridize to form the 4 lowest order modes on a nanospherical dimer. Figure 4.2 presents the hybridized resonance modes. The hybridization causes the resonance frequencies to also shift in the manner as indicated by the vertical axis.

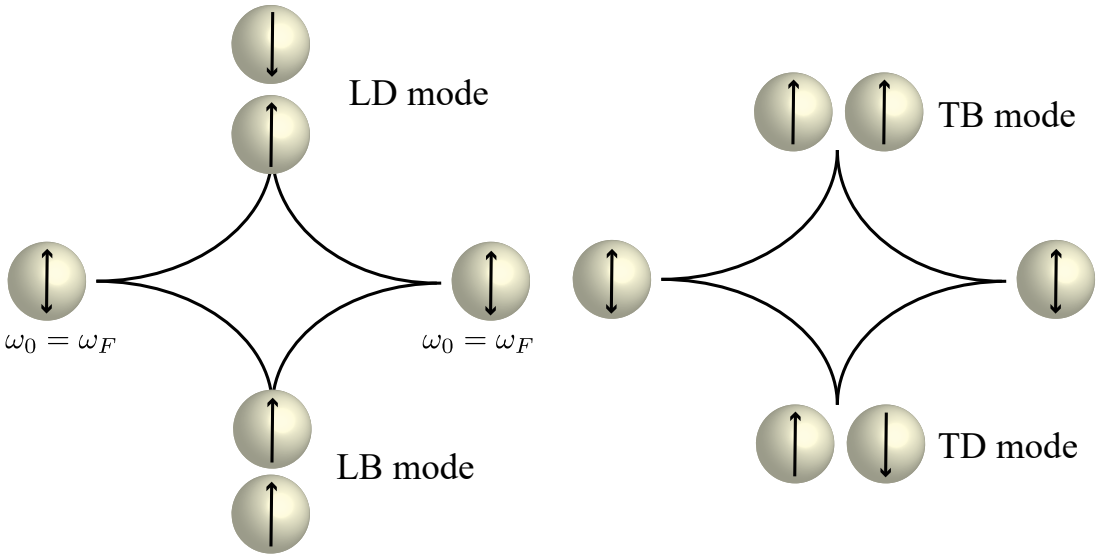


Figure 4.2: The hybridization of the dipole modes of a spherical nanoparticle forms the lowest order modes of a nanospherical dimer. (a) The longitudinal modes; Longitudinal Dark(LD) and Longitudinal Bright(LB). (b) The transverse modes; Transverse Dark(TD) and Transverse Bright(TB)

Two of the charge modes formed have a vector-like structure indicating that

they are dipole active, or bright. This essentially indicates that the charge distribution on the dimer is such that a non-zero dipole moment exists. This also implies that the modes emit dipole radiation into the far-field. This underlies their "bright" character. The dark modes are dipole inactive since they do not possess a net dipole moment. But they do posses a net quadrupolar moment. However, for small particles, the quadrupolar radiation is insignificant and they do not radiate into the far field. Thus the term "dark". For small particles, all higher order multipolar charge distributions are considered dark due to the lack of radiation into the far field.

The modes may also be classified according to the relative orientation of the dipoles with respect to the dimer axis: longitudinal for parallel dipole and dimer axis, and transverse for the perpendicular case. Apart from these modes, there are a host of other dipole inactive dark modes in a nanospherical dimer setup. But much of the behaviour of the dimers is dictated by these lowest order modes. These modes can be derived using the Laplace equation formalism, the NP operator formalism, or the plasmon hybridization formalism [18].

## 4.2 Dipole approximation and plasmon hybridization

As shown in the earlier section, the main operational modes in a nanospherical dimer may be derived as a combination of dipole modes in a singlet nanosphere. Using this simple approach, an approximation may be derived for the hybrid modes in a nanospherical dimer.

Throughout this section, we will denote the center coordinate of the spheres by $\mathbf{r}_1$ and $\mathbf{r}_2$, and their separation along the axis joining the centers to be $D$. As shown in Fig. 4.3, the radii of the spheres will be taken to be equal to $R$ and the relative permittivity of the metal will be denoted by $\epsilon_m$. We mainly consider the metal to be silver and use the permittivities given by Jiang *et al.* [19]. These values

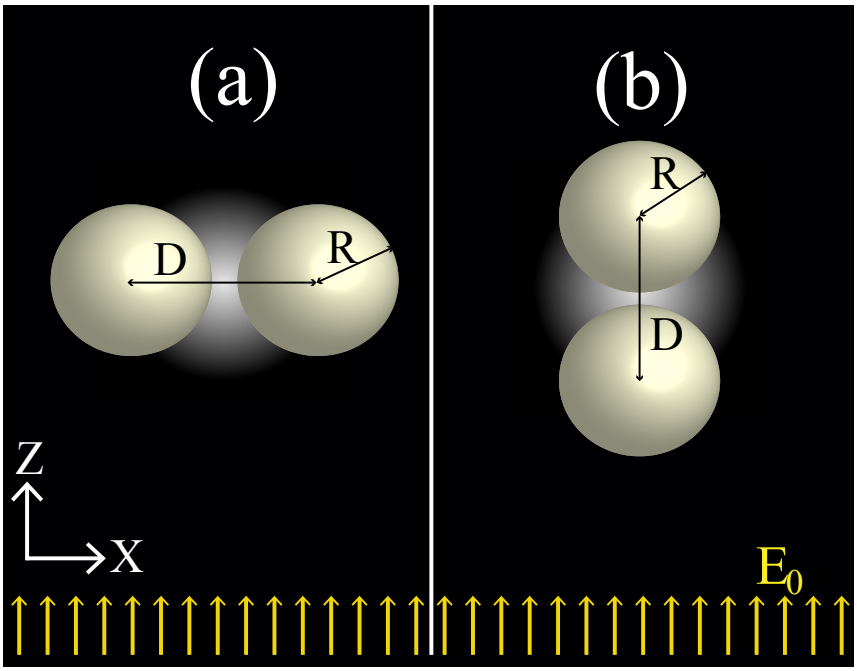


Figure 4.3: The two dimer setups (a)transverse and (b)longitudinal. We orient the external electric field and hence the dipole moments along the z-axis as shown. The y-axis can be determined from the right hand rule.

are an improvement over the often used Johnson and Christy [20] measurements and have been derived under extremely controlled settings. We denote the relative permittivity of the medium in which the system is placed in by $\epsilon_b$. In both the transverse and longitudinal setups, we will consider the external electric field to be oriented along the z-direction. This forces the dipole moments in both setups to be oriented along the z-direction. For the transverse setup, the two spheres will be placed along the x-axis causing the electric field to be perpendicular to the axis joining the spheres. In the longitudinal setup, the spheres are arranged along the z-direction and the electric field is parallel to the axis joining the spheres.

The dipole moment arising in a spherical metal nanoparticle in the presence of an external electric field $\mathbf{E}_0(t) = \mathrm{Re}\{\mathbf{E}_0 e^{-i\omega t}\}$ can be given as [21],

$$\mathbf{P} = \alpha R^3 \mathbf{E}_0, \tag{4.1}$$

where $R$ is the radius of the sphere and the polarizability of the metallic sphere is given by,

$$\alpha = \frac{\epsilon_m - \epsilon_b}{\epsilon_m + 2\epsilon_b}. \tag{4.2}$$

Note that we use the quasi-static approximation and hence, the field is independent of the position vector $\mathbf{r}$ and the amplitude can be given by the constant vector $\mathbf{E}_0$. The resonance condition for such a nanosphere is determined by the real part of the denominator equalling to zero, $\mathrm{Re}\{\epsilon_m\} = -2\epsilon_b$. For a sphere placed inside a vacuum, this condition is the well known resonance condition, $\mathrm{Re}\{\epsilon_m\} = -2$. This dipole moment in turn induces an electric field outside the sphere given by,

$$\mathbf{E}_{\text{induced}} = \frac{[3(\mathbf{P}\cdot\mathbf{r})\mathbf{r} - |\mathbf{r}|^2\mathbf{P}]}{|\mathbf{r}|^5}. \tag{4.3}$$

Next we turn to the problem of analysing the resonances in metal sphere dimers. Using Eqs. (4.1) and (4.3), we can assign dipole moments to each of the two spheres and calculate the retarded electric fields at each sphere due to the other. Requiring the field values to be self-consistent gives us a solution for the dipole moments of each of the spheres. Subsequently we use these dipole moment values to quantize the electric field in the dimer system. This approach only considers the dipole modes of the dimer system and neglects all other higher order modes.

**Plasmonic Resonances in transverse dimers**

Now we derive the resonance form of a transverse dimer setup. We assume the size of the system to be much smaller compared to the wavelength of light and hence the complete system sees an external electric field value independent of position $\mathbf{r}$ given by, $\mathbf{E}_0(t) = \mathrm{Re}\{\mathbf{E}_0 e^{-i\omega t}\}\hat{\mathbf{z}}$, where $E_0$ is the constant amplitude of the electric filed in the z-direction. We specifically choose this directionality of the

external electric field to focus on the dipole moments and the plasmon oscillations along the z-direction. The total electric field within the system can be written in the time harmonic approximation as, $\mathbf{E}(t) = \mathrm{Re}\{\mathbf{E}e^{-i\omega t}\}$. The two spheres have identical polarizability values $\alpha$, radii $R$, permittivities $\epsilon_m$, separation $D$ and dipole moments in the z-direction denoted by $P_1$ and $P_2$. Given $E_1$ and $E_2$ to be the electric field amplitudes in the z-direction on the two spheres, for the electric field outside the two spheres we can write,

$$\mathbf{E}(\mathbf{r}) = \mathbf{E}_0 + \alpha[E_1\mathbf{G}(\mathbf{r};\mathbf{r}_1) + E_2\mathbf{G}(\mathbf{r};\mathbf{r}_2)], \tag{4.4}$$

using the dyadic Green's function forms $\mathbf{G}(\mathbf{r};\mathbf{r}_d)$,

$$\mathbf{G}(\mathbf{r};\mathbf{r}_d) = \frac{R^3\{3[\hat{\mathbf{z}}\cdot(\mathbf{r}-\mathbf{r}_d)](\mathbf{r}-\mathbf{r}_d) - |\mathbf{r}-\mathbf{r}_d|^2\hat{\mathbf{z}}\}}{|\mathbf{r}-\mathbf{r}_d|^5}, \tag{4.5}$$

for $d = 1, 2$. The center coordinates of the spheres are given by, $\mathbf{r}_1 = [-D/2, 0, 0]$ and $\mathbf{r}_2 = [D/2, 0, 0]$. At the exact locations of the spheres, Eq. (4.4) gives,

$$E_1 = E_0 - \frac{P_2}{D^3}, \tag{4.6a}$$

$$E_2 = E_0 - \frac{P_1}{D^3}. \tag{4.6b}$$

Using $P_1 = \alpha R^3 E_1$ and $P_2 = \alpha R^3 E_2$, we can write two simultaneous linear equations for $E_1$ and $E_2$. Solving these would give us the exact values of the dipole moments to be,

$$P_1 = P_2 = \frac{\alpha R^3 E_0}{1 + \frac{\alpha R^3}{D^3}}. \tag{4.7}$$

Comparing this equation to (4.1), this equation can be interpreted as a modification of the effective polarizability of the nanospheres to $\alpha_{\text{eff}} = \frac{\alpha}{1+\frac{\alpha R^3}{D^3}}$. The electric fields inside the two spheres($d = 1, 2$) can be given by [21],

$$E_{d,\text{internal}} = E_d \frac{3\epsilon_b}{\epsilon_m + 2\epsilon_b} = E_d \alpha \frac{3}{\epsilon_m - \epsilon_b} \approx -\alpha E_d. \tag{4.8}$$

The last approximation is valid near resonance due to the fact that $\text{Re}\{\epsilon_m\} \approx -2\epsilon_b$.

Next we turn to the problem of quantizing the dimer electromagnetic field. Currently we have derived the electric field as generated by an external field. To derive the localised plasmon field, we need to find the localised solution of Maxwell's equations. To do this, following [22], we stimulate the system with an impulse of the form $\mathbf{E}_{\text{impulse}} = E_0 \delta(t) \hat{\mathbf{z}}$ instead of a constant external field. After $t = 0$, the response that remains in the system will be exactly the localised solution,

$$\mathbf{E}_{\text{dimer}}(\mathbf{r}, \omega) = \frac{\alpha E_0}{1 + \frac{\alpha R^3}{D^3}} [\mathbf{G}(\mathbf{r}; \mathbf{r}_1) + \mathbf{G}(\mathbf{r}; \mathbf{r}_2)]. \tag{4.9}$$

The Drude model for permittivities of silver, given the plasma frequency $\omega_p$ and decay rate $\gamma_0$ and the core permittivity $\epsilon_{\text{core}}$, can be written as [23],

$$\epsilon_m = \epsilon_{\text{core}} - \frac{\omega_p^2}{\omega(\omega + i\gamma_0)}. \tag{4.10}$$

Assuming this model holds with $\epsilon_{\text{core}} = 1$, and assuming that the external environment to be the vacuum($\epsilon_b = 1$), we can write the effective polarizability $\alpha_{\text{eff}}$ as,

$$\begin{aligned} \alpha_{\text{eff}} &= \frac{\epsilon_m - \epsilon_b}{(\epsilon_m - \epsilon_b)(1 + \frac{R^3}{D^3}) + 3\epsilon_b} \\ &= \frac{\omega_F^2}{\omega_F^2(1 + \frac{R^3}{D^3}) - (\omega^2 + i\omega\gamma_0)}. \end{aligned} \tag{4.11}$$

Here, $\omega_F = \omega_p / \sqrt{2\epsilon_b + 1} = \omega_p / \sqrt{3}$ is the Fröhlich frequency in the vacuum.

Defining $\omega_0 = \sqrt{(1 + \frac{R^3}{D^3})}\omega_F$ and making the standard approximation $\omega \sim \omega_F \sim \omega_0 \gg \gamma_0$, this allows us to rewrite Eq. (4.11) as,

$$\alpha_{\text{eff}} \approx \frac{\omega_F/2}{(\omega_0 - \omega) - i\gamma_0/2}.$$

Using this, we can rewrite Eq. (4.9) as,

$$\mathbf{E}_{\text{dimer}}(\mathbf{r}, \omega) = \frac{\omega_F E_0/2}{\omega_0 - i\gamma_0/2 - \omega}[\mathbf{G}(\mathbf{r}; \mathbf{r}_1) + \mathbf{G}(\mathbf{r}; \mathbf{r}_2)]. \tag{4.12}$$

This equation exactly predicts a resonant system with frequency $\omega_0$ and damping $\gamma_0/2$. In the time domain this translates to,

$$\mathbf{E}_{\text{dimer}}(\mathbf{r}, t) = \frac{\omega_F E_0}{2}[\mathbf{G}(\mathbf{r}; \mathbf{r}_1) + \mathbf{G}_(\mathbf{r}; \mathbf{r}_2)] \sin(\omega_0 t) e^{-\gamma_0 t/2}. \tag{4.13}$$

For a singlet nanosphere, the dipole resonance frequency is located at the Fröhlich frequency($\omega_F$). But for the bright mode of a transverse dimer, we see that the earlier analysis predicts a shifting of the resonance frequency. Furthermore, we see that this shift is exactly a blue shift. We also note that while this result was derived with the assumption of $\epsilon_{\text{core}} = 1$, for silver, this is not valid in general. The general expression only clutter the presentation with no added rigor, so we have opted for the simpler result. In particular, the general expression does not alter the form of the quantized field equation nor the calculated field intensities and coupling rate values. Please see Appendix F for the general form.

As mentioned earlier, since we excite the the system with a field in the z-direction, we only consider the dipole mode oriented along the z-direction. Since the dipole modes are orthogonally directed, such a procedure is justified and easily generalised to the case of a field in an arbitrary direction. Defining $\beta =$

$\frac{\omega_F E_0}{2}$, the total energy $W$ in this mode can be calculated as,

$$W = \frac{\beta^2}{8\pi} \sin^2(\omega_0 t) \mathcal{W}(D), \tag{4.14}$$

where,

$$\mathcal{W}(D) = \int |\mathbf{G}(\mathbf{r}; \mathbf{r}_1) + \mathbf{G}(\mathbf{r}; \mathbf{r}_1)|^2 \, \mathrm{Re} \left\{ \frac{d}{d\omega}(\omega\epsilon) \Big|_{\omega=\omega_0} \right\} d^3\mathbf{r}, \tag{4.15}$$

The extra derivative factor in the expression precisely accounts for the energy in dispersive media [24]. Note that this integration extends over infinite space. Defining normalisation factor,

$$N = \sqrt{\frac{8\pi\hbar\omega_0}{\mathcal{W}(D)}}, \tag{4.16}$$

and normalised amplitude,

$$B = \frac{\beta}{N}, \tag{4.17}$$

enables us to write the total potential energy stored in the electric field as,

$$W = \hbar\omega_0 B^2 \sin^2(\omega_0 t). \tag{4.18}$$

**Plasmonic Resonances in longitudinal dimers**

Now we turn to the question of longitudinal dimers. The equations and formulas applying to the longitudinal dimers remain approximately equal to the transverse. The main difference arises from the geometry of the setup, where, as dictated by Eq. (4.3), the electric fields at the position of the spheres can be expressed as, $E_1 = E_0 + \frac{2P_2}{D^3}$ and $E_2 = E_0 + \frac{2P_1}{D^3}$. These equations give,

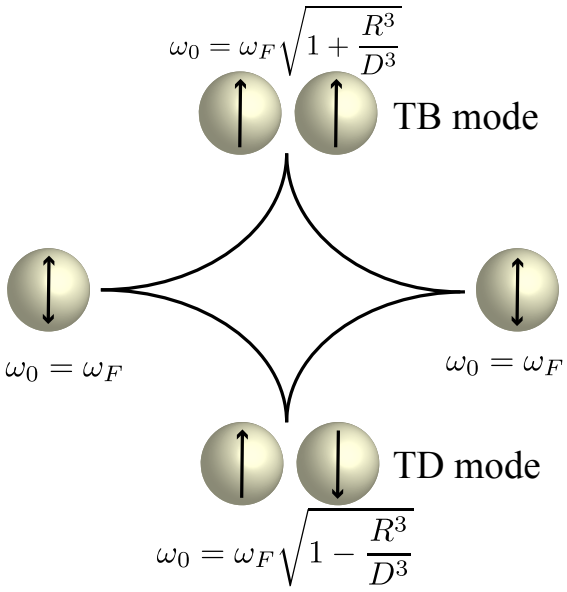


Figure 4.4: The two dimer setups (a)transverse and (b)longitudinal. We orient the external electric field and hence the dipole moments along the z-axis as shown. The y-axis can be determined from the right hand rule.

$$P_1 = P_2 = \frac{\alpha R^3 E_0}{1 - 2\frac{\alpha R^3}{D^3}}. \tag{4.19}$$

The effective polarizability of the dimers get modified to,

$$\alpha_{\text{eff}} = \frac{\alpha}{1 - 2\frac{\alpha R^3}{D^3}}. \tag{4.20}$$

Using this form and following a similar procedure as we did in Eqs. (4.11) and (4.12), the electric field of the dimer system in the frequency domain can thus be obtained as,

$$\mathbf{E}_{\text{dimer}}(\mathbf{r}, \omega) = \frac{\omega_F E_0/2}{\omega_0 - i\gamma_0/2 - \omega}[\mathbf{G}(\mathbf{r}; \mathbf{r}_1) + \mathbf{G}(\mathbf{r}; \mathbf{r}_1)], \tag{4.21}$$

where $\omega_0 = \sqrt{1 - 2\frac{R^3}{D^3}}\omega_F$. Note that in the above equations, the $\mathbf{G}(\mathbf{r}; \mathbf{r}_1)$ and $\mathbf{G}(\mathbf{r}; \mathbf{r}_2)$ differ from that of the transverse setup by virtue of the difference in $\mathbf{r}_1$ and

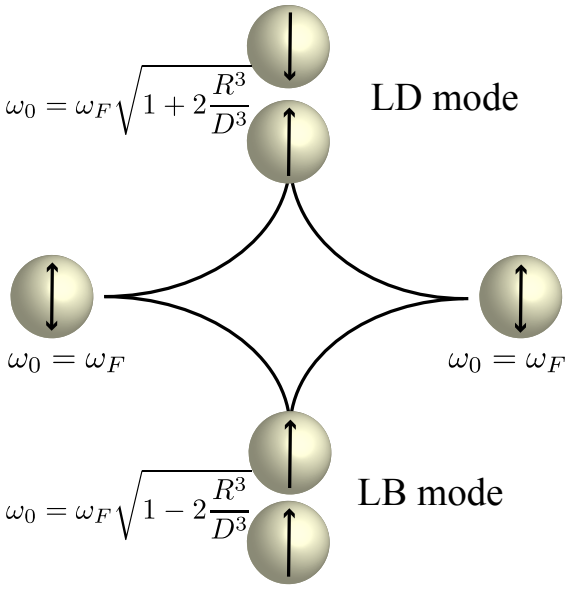


Figure 4.5: The two dimer setups (a)transverse and (b)longitudinal. We orient the external electric field and hence the dipole moments along the z-axis as shown. The y-axis can be determined from the right hand rule.

$\mathbf{r}_2$. For the longitudinal setup, $\mathbf{r}_1 = [0, 0, D/2]$ and $\mathbf{r}_2 = [0, 0, -D/2]$. The total energy in the electric field can be shown to have the same form as the transverse configuration given in Equation (8.1).

An exactly similar procedure may be followed to derive the dark mode resonance frequencies and electric fields in the dimer setup. These results are summarised in figures 4.4 and 4.5.

Next we turn to the extinction profiles of the dimer setups to extract the exact resonance frequencies. The extinction efficiency for dimer setups can be given by [25],

$$C_{\text{ext}} = \frac{4\pi k}{S_d E_0^2} \sum_i \text{Im}\left\{E_0.P_i\right\}. \tag{4.22}$$

Here, the cross sectional area $S_d = \pi R^2 + 2RD$ for transverse dimers and $S_d = \pi R^2$ for longitudinal dimers. The sum runs over the two dipoles. We note here that since our formulation only considers the near-field, the extinction cross

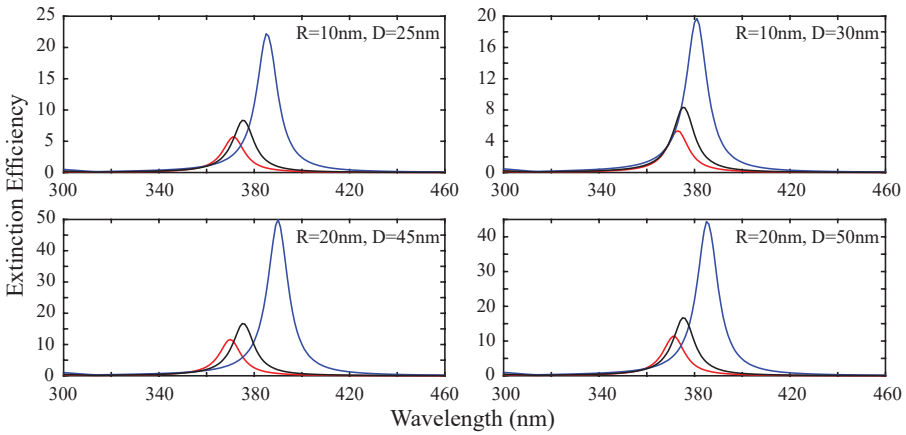


Figure 4.6: The extinction efficiencies for the singlet(black), transverse dimer(red) and longitudinal dimer(blue)setups for various nanosphere sizes and separations. (a) R=10 nm and D=25 nm; (b) R=10 nm and D=30 nm; (c) R=20 nm and D=45 nm; (d) R=20 nm and D=50 nm.

sections presented are equivalent to absorption cross sections. Figure 4.6 plots the extinction cross sections for singlet, transverse dimer and longitudinal dimer configurations for 10 nm and 20 nm silver spheres. As expected, when the dimers are further apart, the extinction efficiencies decrease. We also find that the 20 nm sphere setups have larger extinction compared to the 10 nm spheres at resonance. As far as the linewidths are concerned, all spheres have similar or comparable linewidth as calculated as a FWHM value of $\approx$ 11 nm. This is as predicted by Eqs. (4.12) and (4.21), where we see that the linewidth for both dimer setups are equal to the singlet linewidth $\gamma_0/2$.

In addition to that, increase in extinction efficiency and the shifting of the resonance frequency are observed in the dimer setups as expected. The transverse dimer bright mode, being an anti-bonding mode, experiences a blue shift while the longitudinal dimer experiences a red shift on account of its bright mode being a bonding mode. The equations we derived for the resonance frequency during the quantization of the dimer systems also predict a similar pattern. To study the accuracy of these formulas derived in the dipole approximation, in Fig. 4.7 we

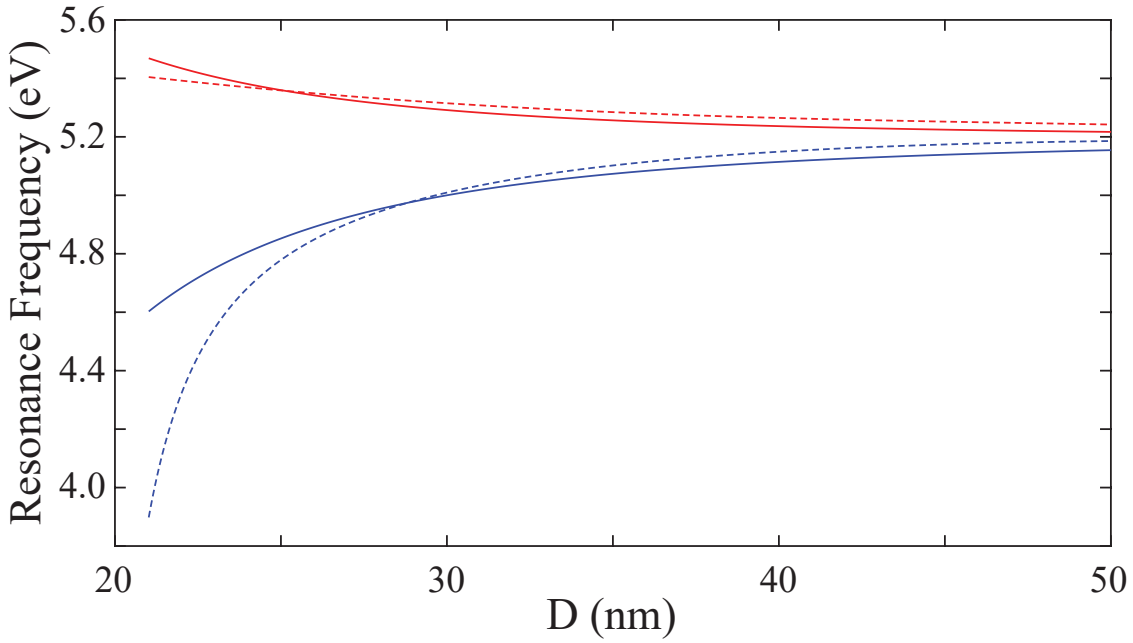


Figure 4.7: The predicted resonance frequencies for the transverse dimer(red) and longitudinal dimer(blue) configurations by the formula we derive(solid lines) and the predictions of the full multipole theory(dashed lines).

plot the resonance frequencies as predicted by the formulas($\omega_0 = \sqrt{1 - 2\frac{\alpha R^3}{D^3}}\omega_F$ for the longitudinal dimer and $\omega_0 = \sqrt{1 + \frac{\alpha R^3}{D^3}}\omega_F$ for the transverse), with those as predicted by the full multipole calculations of plasmon hybridization theory [26]. The multipole predictions are derived assuming a Drude model with plasma frequency $\omega_p = 9\,\text{eV}$ for 10nm silver spheres. We observe that the formulas do in fact predict the resonance frequencies reasonably well for separations $D > 5\,\text{nm}$. At shorter distances, the effects of multipoles and other electron cloud distortion based effects play a significant role. Transverse and longitudinal dimers actually experience asymmetric shifting of the resonance frequency due to the presence of the factor of 2 in the formula for the longitudinal resonance frequency.

# Chapter 5

# Surface plasmon resonances on nano-tori

As was discussed earlier, the plasmonic structure of the simplest of nano-structures, the sphere, was analysed over a century ago [12] and it was shown that the electromagnetic field modes generated take the form of the so called solid harmonics. The charges on the surface of a sphere take the form of spherical harmonics [15]. The spherical harmonics thus result in the 3-fold degenerate dipole modes, 5-fold degenerate quadrupolar modes and all the other higher order modes. The structure and behaviour of these modes are understood perfectly and a summary of these is presented in Figure 5.1(a). $\omega_F$ in the Figure is the so-called Fröhlich frequency, at which value the permittivity of the material *epsilon* is such that $\mathrm{Re}\{\epsilon\} = -2$. $\omega_C$ is the frequency at which $\mathrm{Re}\{\epsilon\} = -1$. One important factor to note about the modes on a sphere is that they are orthogonal: the surface charge modes over the surface of the sphere are orthogonal to each other. This means that given a specific excitation scheme, there is more than one specific combination of modes that will be excited.

Beyond the sphere, in terms of genus, the representative structure in the next level of topological hierarchy is the torus. In plasmonic applications, the torus structure has shown to be incredibly useful as a primary nano-structure allowing for enhanced tuning capabilities compared to spheres [27]. Torus structures have high field confinement in the center and also modes with non-zero magnetic

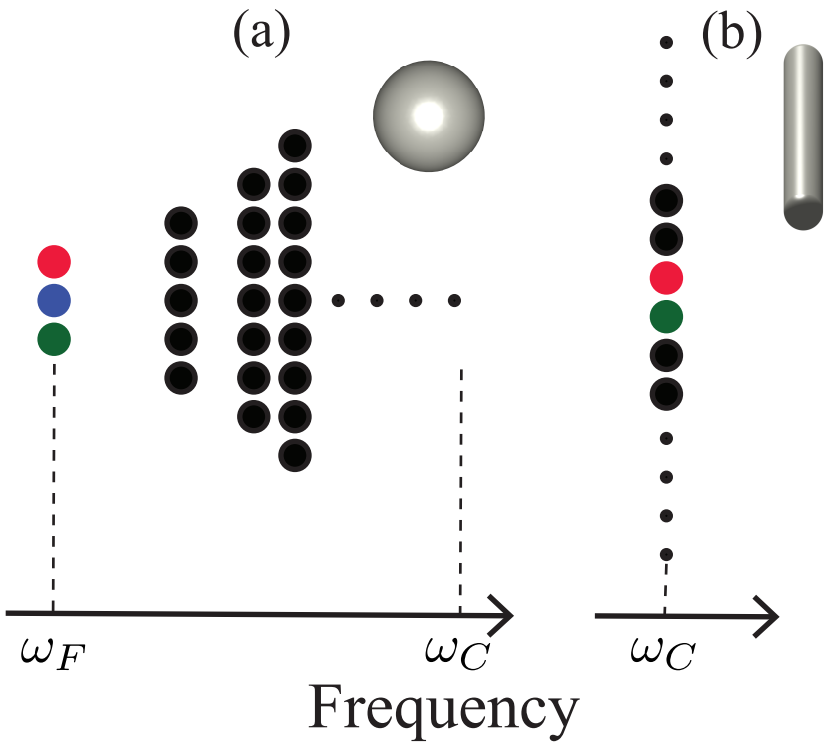


Figure 5.1: (a)The plasmonic modes of a sphere and (b) transverse plasmonic modes of a cylinder. The dipole modes are shown in color while the dark modes are black. The dipole x-mode is shown in red, the y-mode in blue and the z-mode in green. The cylinder axis is assumed to be oriented along the y-axis.

dipole moment [28]. It has been known for a while that the Laplace equation is approximately separable in toroidal coordinates [29]. The first attempts at solving the Laplace equation on a torus surface was carried out in [30, 31] in the context of toroidal plasma analysis. In the plasmonic domain, the first attempt at an analysis was done in [28] under certain assumptions. The first complete analysis of the problem was carried out in [32] and [33]. It was also in [32], that the existence of poloidal modes(azimuthally symmetric modes) were first demonstrated. The existence of an infinite class of such modes were shown. In addition this, plasmonic analyses of modes on a torus were carried out in [27] and [34] within the framework of plasmon hybridization. This formalism described the plasmonic modes on a torus surface as arising from hybridisation of primitive plasmons on the inner and outer surface of a torus. However, almost all of these studies focused mainly on toroidal modes, or modes with charge variations in the x-y plane, for a torus with axis along the z-direction. In this chapter, we shall focus on the poloidal modes, or modes whose variations are strictly along direction of the torus axis, and show that the poloidal structure results in numerous amazing hidden properties.

Seemingly unrelated to these developments in fields of physics, it was recently demonstrated that the spectrum of the so-called Neumann-Poincare(NP) operator on the surface of a torus possesses an infinite number of a negative eigenvalues [35]. The eigenfunctions of the NP operator for a given surface are known to furnish the surface charge plasmonic eigenmodes of a particle bounded by that surface, in the quasi-static approximation [15]. The eigenvalues correspond to the resonant permittivities. As we shall show, these eigenmodes with negative eigenvalues actually include an infinite set of poloidal modes which are different to the ones shown to exist in [32]. We shall show that the complete set of poloidal plasmonic modes on a torus may be described as two infinite sets of modes: one set as discovered in [32] with positive NP eigenvalues, and another set with nega-

tive eigenvalues which we demonstrate here for the first time. We will show that these two sets arise from the breaking of the poloidal symmetry when a cylinder is folded to form a torus. By our analysis of these poloidal modes, we complete our understanding of plasmonic modes on a torus.

In the first section of this chapter we establish the coordinate systems and derive an approximate equation for the negative NP-eigenvalue poloidal modes. In the next section we solve the NP equation numerically and show the existence of the dual set of poloidal modes and establish the symmetry broken structure and show that the modes converge to the modes of a cylinder in the low aspect ratio limit. In the final section we solve Maxwell's equations and study how the modes overlap and behave under scattering and extinction studies.

## 5.1 Analytical characterisation

Let's first set up the coordinate system on a torus. The toroidal coordinates $(\xi, \eta, \phi)$ as shown in Figure 5.2 are usually the coordinates used to study the structures on toroidal surfaces. We also note a very interesting property of the toroidal coordinate system here. Performing a geometric inversion of the toroidal coordinates with center at $O$ and radius $r_0$ furnishes a conformal map from the torus onto itself. This transformation can also be thought of approximately as a transformation taking the outside surface portion of the torus to in the inside and vice versa. The toroidal coordinates themselves are orthogonal. However, the Laplace equation is only approximately separable in toroidal coordinates. This property was known for a long time and the electric potential field can be expressed as an expansion in terms of the toroidal harmonics [36],

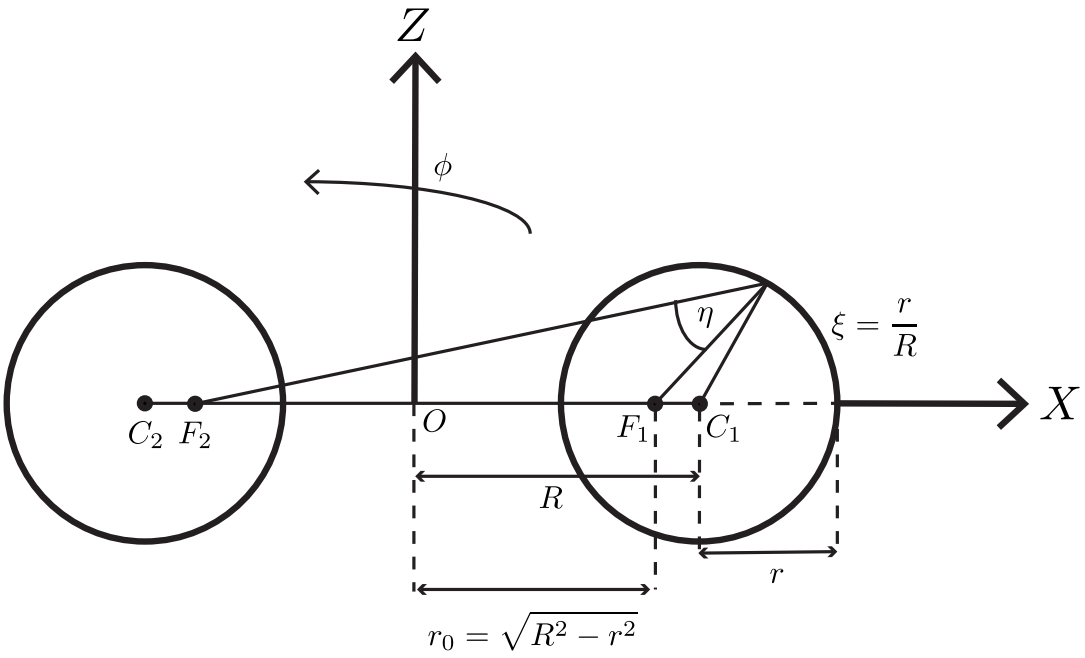


Figure 5.2: The toroidal coordinate system and the natural coordinate system on a torus.

$$\Phi(\xi,\eta,\phi) = \sqrt{1-\xi\cos(\eta)}\sum_{m,n}\left\{\begin{array}{c} T_{mn} \\ S_{mn} \end{array}\right\} \times \left\{\begin{array}{c} \cos(m\eta) \\ \sin(m\eta) \end{array}\right\} \times \left\{\begin{array}{c} \cos(n\phi) \\ \sin(n\phi) \end{array}\right\}, \tag{5.1}$$

where $T_{mn} = \xi^{-1/2}Q^n_{m-1/2}(1/\xi)$ and $S_{mn} = \xi^{-1/2}P^n_{m-1/2}(1/\xi)$ with $Q^\alpha_\beta$ and $P^\alpha_\beta$ as the associate Legendre functions. The curly braces indicate that any one of the functions within may be chosen to form a valid mode. This equation can be viewed as a modal expansion. The azimuthal direction in a torus is usually referred to as the toroidal direction and the modes that vary in that direction are referred to as toroidal modes. These modes have $m = 0$. On the other hand, the direction as labelled by $\eta$ or $\theta$ is the poloidal direction and the modes are referred to as poloidal modes($n = 0$). All other modes are non-trivial superpositions of toroidal and poloidal modes.

As can be seen, the solution is separable in the azimuthal coordinate $\phi$ due to the corresponding exact symmetry of the torus. This means that the terms in Eq. (5.1) with different $n$ values are orthogonal. However, the $\xi$ and $\eta$ coordinates are intrinsically coupled and hence the modes with different $m$ values are not orthogonal. Hence, in general, the toroidal plasmonic response will be a mixture of modes with different $m$ values.

To study the structure of the poloidal modes, we turn to a different formulation of the Laplace equation and the associated boundary value problem: the Neumann-Poincare(NP) operator. First proposed by Poincare [13] and Neumann [14] in the context of an extremal value problem, the NP operator has recently received much attention in plasmonics as a convenient alternative to the Laplace equation based methods [15]. The surface charge plasmonic modes of a bounded structure occupying the domain $\Omega$ in $\mathbb{R}^3$ and bounded by $\partial\Omega$ with surface elements $\sigma$ are described as eigenfunctions of the adjoint Neumann-Poincare operator,

$$\mathcal{K}^*[\phi](\mathbf{x}) = p.v.\frac{\lambda}{2\pi}\int_{\partial\Omega}\frac{(\mathbf{x}-\mathbf{y})\cdot\nu_{\mathbf{x}}}{|\mathbf{x}-\mathbf{y}|^3}\phi(\mathbf{y})d\sigma(\mathbf{y}). \tag{5.2}$$

The resonant permittivities $\epsilon$ are related to the eigenvalues $2\pi/\lambda$ of the operator as,

$$\lambda = \frac{\epsilon-\epsilon_b}{\epsilon+\epsilon_b}. \tag{5.3}$$

$\epsilon_b$ is the permittivity of the surrounding space($\mathbb{R}^3 \setminus \Omega$). It is known that the spectrum of the operator in a smooth domain is real, discrete and that $\lambda = 1$ is one of the eigenvalues. All other eigenvalues have $|\lambda| > 1$ [15]. If we let $\omega_C$ be the frequency at which $\mathrm{Re}\{\epsilon\} = -1$ of the plasmonic medium, then positive eigenvalues correspond to resonance frequencies $\omega < \omega_C$ and negative eigenvalues correspond to frequencies $\omega > \omega_C$. We use the subscript $C$ here since it is at that

very frequency that the transverse plasmonic modes of a cylinder are located(See Figure 1).

We can re-write the NP operator in toroidal coordinates as,

$$\begin{aligned}\mathcal{K}^*[\sigma](\eta,\phi) = &\int \frac{\kappa\alpha(\eta,\eta')\sigma(\eta',\phi')}{(\mu(\phi-\phi')-\cos(\eta-\eta'))^{1/2}}d\eta' d\phi' \\ &- \int \frac{\kappa\alpha(\eta,\eta')\psi(\eta)}{\xi^2}\frac{\sigma(\eta',\phi')(1-\cos(\phi-\phi'))}{(\mu(\phi-\phi')-\cos(\eta-\eta'))^{3/2}}d\eta' d\phi',\end{aligned} \tag{5.4}$$

where $\psi(\eta) = 1-\xi\cos(\eta)$, $\mu(\phi) = 1/\xi^2 + (1-1/\xi^2)\cos(\phi)$, $\kappa = (1-\xi^2)\psi(\eta)^{1/2}/(8\pi\sqrt{2}\xi\psi(\eta')^{3/2})$ and $\alpha(\eta,\eta') = \psi(\eta)^{1/2}/\psi(\eta')^{3/2}$.

Observing Eqn. (5.4), we see that the kernel is a function of $\phi-\phi'$. This is a signature of the exact circular symmetry of the system and indicates that $e^{ik\phi}$, where $k$ is an integer, are possible eigenfunctions. However, the $\eta$ dependence of the system is much more complicated. While the denominator of the kernel contains terms dependent on $\eta-\eta'$, there are other terms that seemingly do not. This structure indicates that the symmetry in the $\eta$ direction is not exact for the torus. The pre-factor terms in Eqn. (5.4) also indicates that the terms of the form $\psi(\eta)^{3/2}$ also seem to be part of the eigenfunctions of the operator. Using these observations we can hypothesise, without loss of generality, that the eigenfunctions should be of the form,

$$\sigma(\eta,\phi) = \psi(\eta)^{3/2}e^{ik\phi}g(\eta). \tag{5.5}$$

With this form, the operator equation reduces to,

$$\begin{aligned}\mathcal{K}^*[\sigma](\eta,\phi) = \kappa\psi(\eta)^{3/2}&\int \frac{1}{\psi(\eta)}\frac{g(\eta')e^{-ik\phi'}}{(\mu(\phi')-\cos(\eta-\eta'))^{1/2}}d\eta' d\phi' \\ &- \frac{\kappa\psi(\eta)^{3/2}}{\xi^2}\int \frac{g(\eta')e^{-ik\phi'}(1-\cos(\phi'))}{(\mu(\phi')-\cos(\eta-\eta'))^{1/2}}d\eta' d\phi',\end{aligned} \tag{5.6}$$

With the inevitable symmetry breaking of the $\psi(\eta)$ functions removed, the kernel still carries a term $1/\psi(\eta)$, that breaks the $\eta$ symmetry of the resulting eigenfunction. To observe the behaviour of the kernel for small $\xi$, we can expand the $1/\psi(\eta)$ term in powers of $\xi$ (This is valid since $|\xi\cos(\eta)| < 1$).

$$\frac{1}{\psi(\eta)} = 1 + \xi\cos(\eta) + \xi^2\cos^2(\eta) + O(\xi^3). \tag{5.7}$$

Taking only the lowest order perturbation, we can rewrite the kernel as,

$$\begin{aligned}\mathcal{K}^*[\sigma](\eta,\phi) = \kappa\psi(\eta)^{3/2}\int \frac{g(\eta')e^{-ik\phi'}}{(\mu(\phi') - \cos(\eta-\eta'))^{1/2}}d\eta' d\phi' \\ - \frac{\kappa\psi(\eta)^{3/2}}{\xi^2}\int \frac{g(\eta')e^{-ik\phi'}(1-\cos(\phi'))}{(\mu(\phi') - \cos(\eta-\eta'))^{1/2}}d\eta' d\phi'.\end{aligned} \tag{5.8}$$

This kernel has exact $\eta$-symmetry and hence we can describe the eigenfunction $g(\eta) = e^{il\eta}$. This gives us the form of the approximate eigenfunctions as,

$$\sigma(\eta,\phi) = \psi(\eta)^{3/2}e^{ik\phi}e^{il\eta}. \tag{5.9}$$

This implies that, apart from the $\psi(\eta)$ term, the eigenfunctions have sinusoidal dependence on both angular variables $\eta$ and $\phi$. Since we are exclusively interested in poloidal modes, we set $k = 0$ and derive the following modes,

$$\sigma_l^S(\eta) = \psi(\eta)^{3/2}\sin(l\eta), \tag{5.10a}$$

$$\sigma_l^C(\eta) = \psi(\eta)^{3/2}\cos(l\eta). \tag{5.10b}$$

$\sigma_l^S$ is antisymmetic and hence will have a net dipole moment while $\sigma_l^C$ will be dark. We plot both charge distributions in Figure 5.3. As can be seen, the charges are mainly localised to the internal "gap" of the torus. We term these modes Internal modes, or I-modes due to this behaviour. We also label the individual

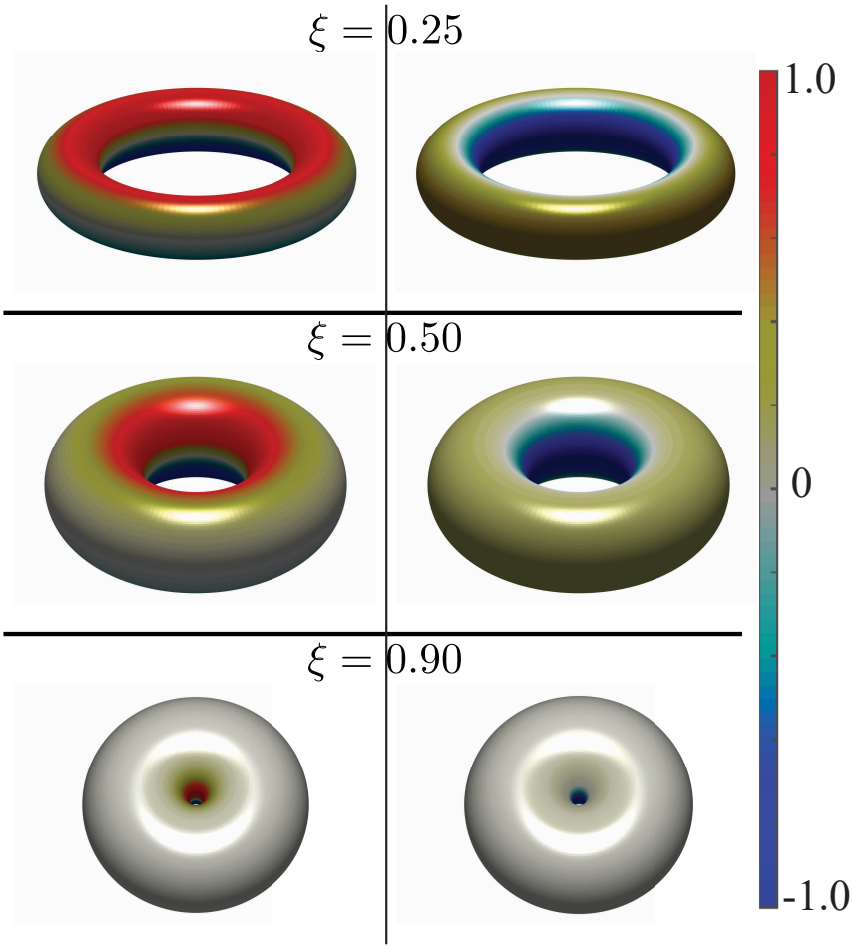


Figure 5.3: The charge distributions of the $IC_1$ and $IS_1$ modes as described by Eqns. (5.10) at various aspect ratios.

modes as either $IS_l$ or $IC_l$ modes, depending on the sine or cosine structure. We further observe from Eqns. (5.10), that for smaller $\xi$, the two modes reduce to the usual sine and cosine cylinder modes. As shown in Figure 5.3, for larger $\xi$ values, the charge distributions of the modes seem to accumulate near the $\eta = \pi$ point.

## 5.2 Numerical characterisation

Now we turn to the numerical solution of the NP operator equation. For this purpose, we can re-interpret Eq. (5.2) as an equation involving solid angles between discretized surface elements $\{\mathbf{x_i}\}$ [15],

$$X_i = \frac{\lambda}{2\pi} \sum_i \omega_{ij} X_j. \tag{5.11}$$

Here, $X_i$ is the total charge on the $i^{th}$ surface element and $\omega_{ij}$ is the solid angle subtended on the $i^{th}$ surface element, by the $j^{th}$ element. The problem can thus be cast in the form of an eigenvalue equation and solved efficiently. We solve this equation and discover the existence of the I-modes we analytically derived earlier. We show the lowest order modes for $\xi = 0.5$ in Figure 5.4(a). The eigenvalues of these modes turn out to be all negative and hence the resonance frequencies $\omega > \omega_C$. The negativity of the eigenvalues may be linked to the negative Gaussian curvature of the inside surface of the torus, where the charge distribution of these I-modes are concentrated. Given a surface element $\delta_i$ on the inside surface of a torus, the $\omega_{ij}$ angles subtended by most other surface elements $\delta_j$ on the inside surface are negative. Hence the sum of Eq. (5.11) is negative, resulting in a negative eigenvalue. We also note here that in [37], it was proven that given a smooth surface with a region with negative Gaussian curvature, the NP spectrum of that surface, or of the surface formed by an inversion, has negative eigenvalues. Given the natural inversion from the torus onto itself that we

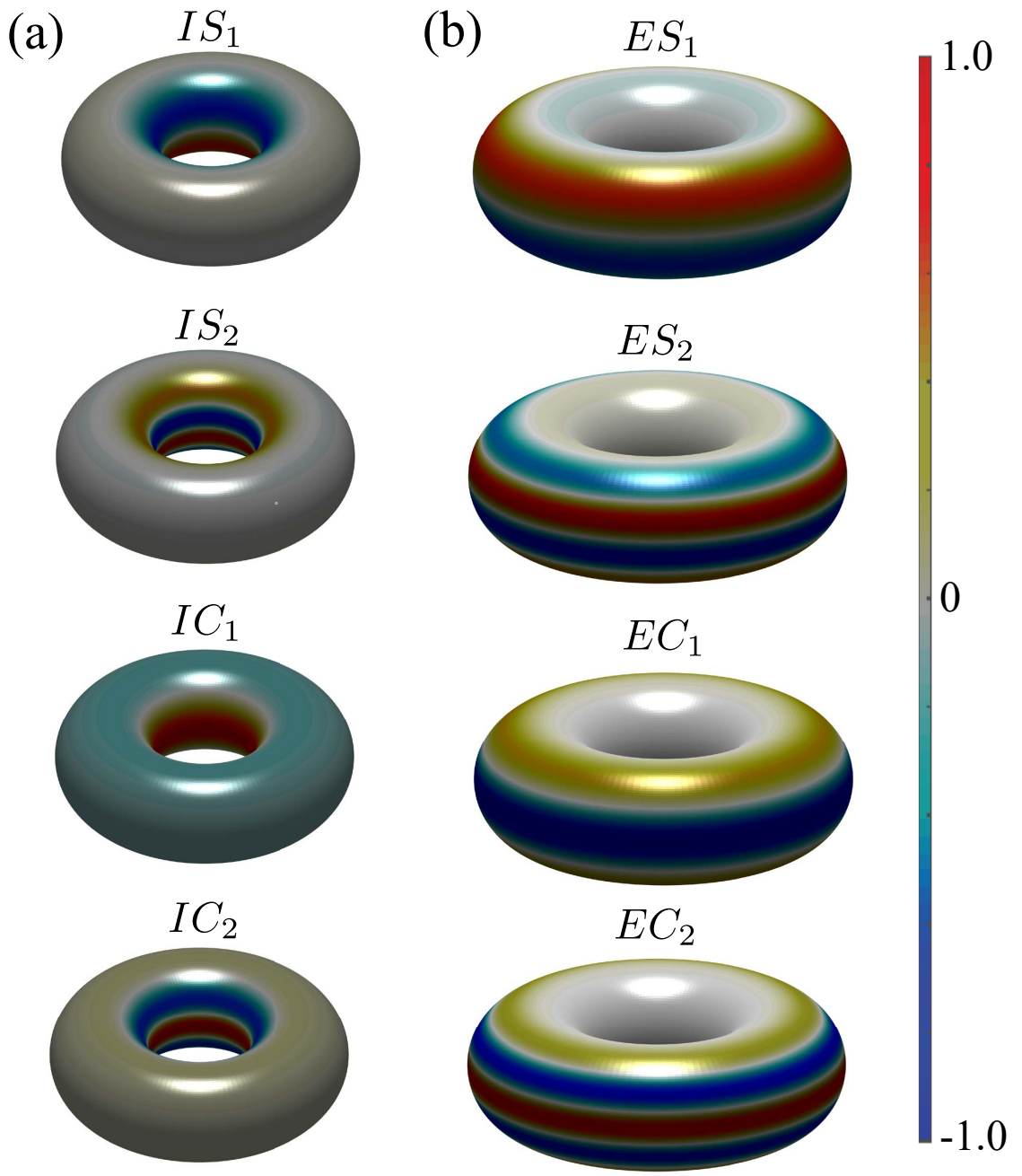


Figure 5.4: The charge distributions for the lowest order I- and E-modes at $\xi = 0.5$.

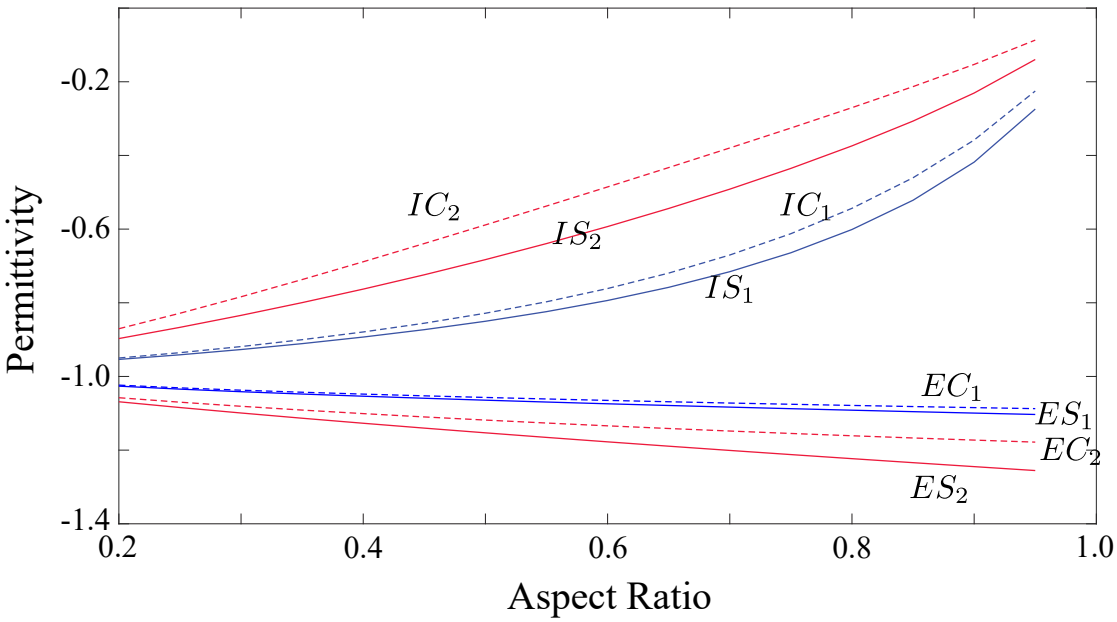


Figure 5.5: The resonance permittivity values of the lowest order I- and E-modes at various aspect ratios.

described earlier, this suggests that the NP spectrum of the torus will contain negative eigenvalues. This observation also reinforces the importance of the negative curvature portion of the surface to the existence of the negative eigenvalue mode and the corresponding I-mode.

In addition to these modes, we discover another set of modes with charge distributions concentrated on the outside surface of the torus. These modes have positive eigenvalues. The positive eigenvalues can be linked to the positive curvature of the outside surface of the torus where the charges are concentrated. We label these modes Exterior modes, or E-modes. Similar to the I-modes we also label them based on the symmetry or asymmetry structure with labels $ES_l$ and $EC_l$. Figure 5.4(b) displays the lowest order of these modes for $\xi = 0.5$. Unlike the I-modes, the E-modes do not display a strong variation of the extent of the charge distribution with changing $\xi$. There is however a very minor effect of accumulating towards the $\eta = 0$ point with increasing $\xi$.

Next we study the resonance permittivities of the two sets of poloidal modes. As can be seen, the I-modes have permittivities $\epsilon > -1$ while the E-modes have $\epsilon < -1$. In [32], the solution of the Laplace equation only established the existence of the lower branches corresponding to the E-modes. We also note that the permittivities tend to $-1$ as the aspect ratio $\xi$ is reduced. This is due to the fact that in the infinitely thin torus limit, the torus structure tends, at least locally, to that of an infinite cylinder. In that limit, the poloidal modes tend to the transverse plasmonic modes of a cylinder(shown in Figure 5.1(b)). We note that all of the transverse modes of a cylinder are located at frequency $\omega_C$. Hence, this graph hints that the two sets of modes may be considered as originating from the splitting of the transverse modes of a cylinder.

We confirm this hypothesis in Figure 5.6, where we plot the charge distribution of the $ES_1$ and $IS_1$ modes at different $\xi$. We see that both of the charge distributions tend towards the charge distribution of a transverse z-dipole mode of a cylinder for smaller $\xi$. This re-establishes that the two sets of modes are actually manifestations of the symmetry breaking that occurs when a cylinder is folded to form a torus. We also study the distribution of the charges over the torus surface at different aspect ratios in Fig. 5.7. This shows that at lower aspect ratios, the charge distributions tend towards the $\theta = \pi/2$ position where the transverse z-dipole mode of a cylinder lies.

Next we show the actual distribution of the mode frequencies and the splitting that occurs when the cylinder is folded into the torus in Figure 5.8.

Next we study the dipole moments of the asymmetric modes we have discovered. The dipole moments of dipole-active modes dictate the majority of the interactions the particle will have with incident light. We plot the first two I- and E-modes in Figure 5.9. The E-modes show a linear variation in the dipole moment. This can be understood by considering that the charge distribution shape of the E-modes remain virtually the same while the minor radius of the torus in-

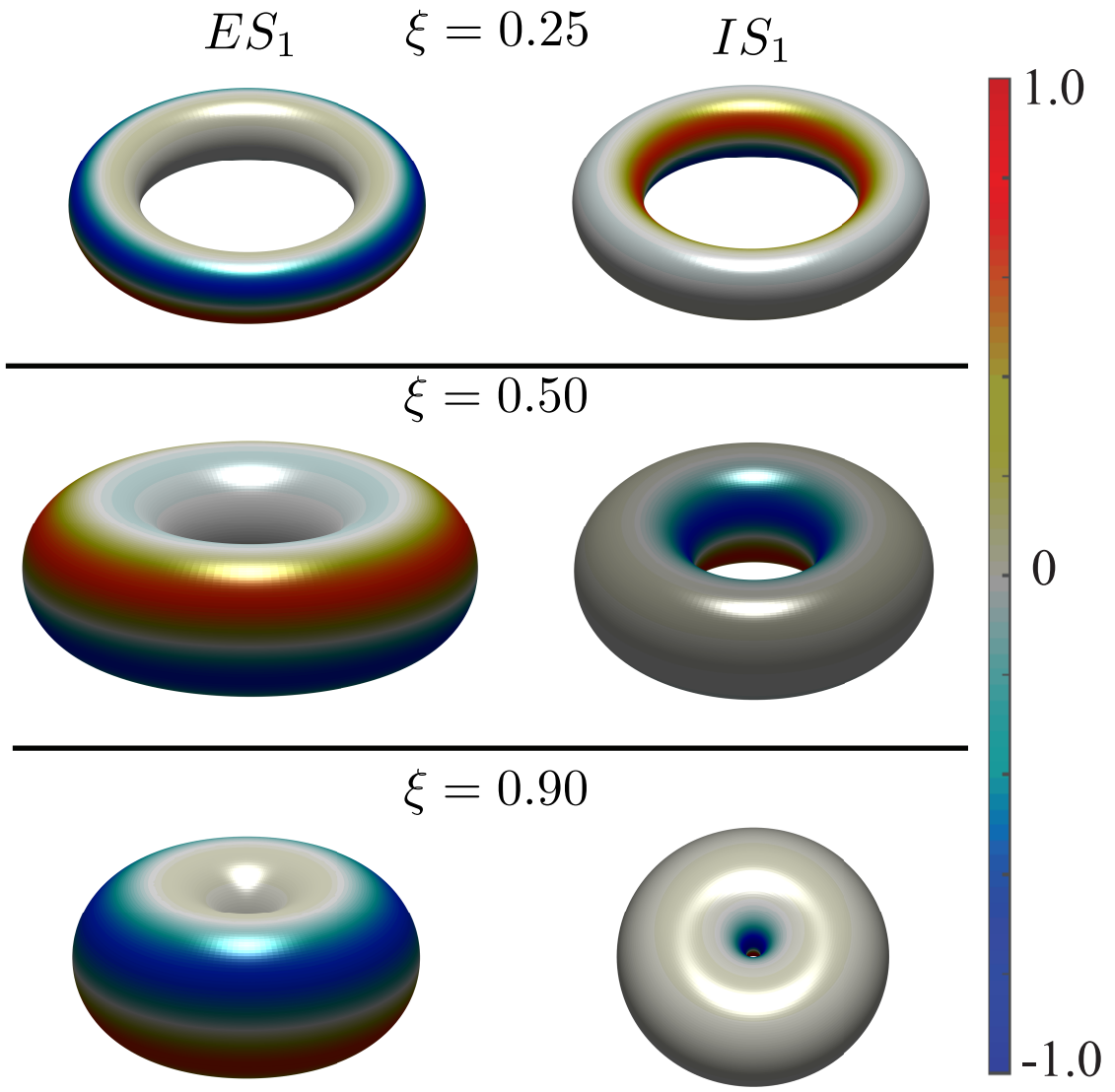


Figure 5.6: The charge distributions of the $ES_1$ and $IS_1$ modes as at various aspect ratios.

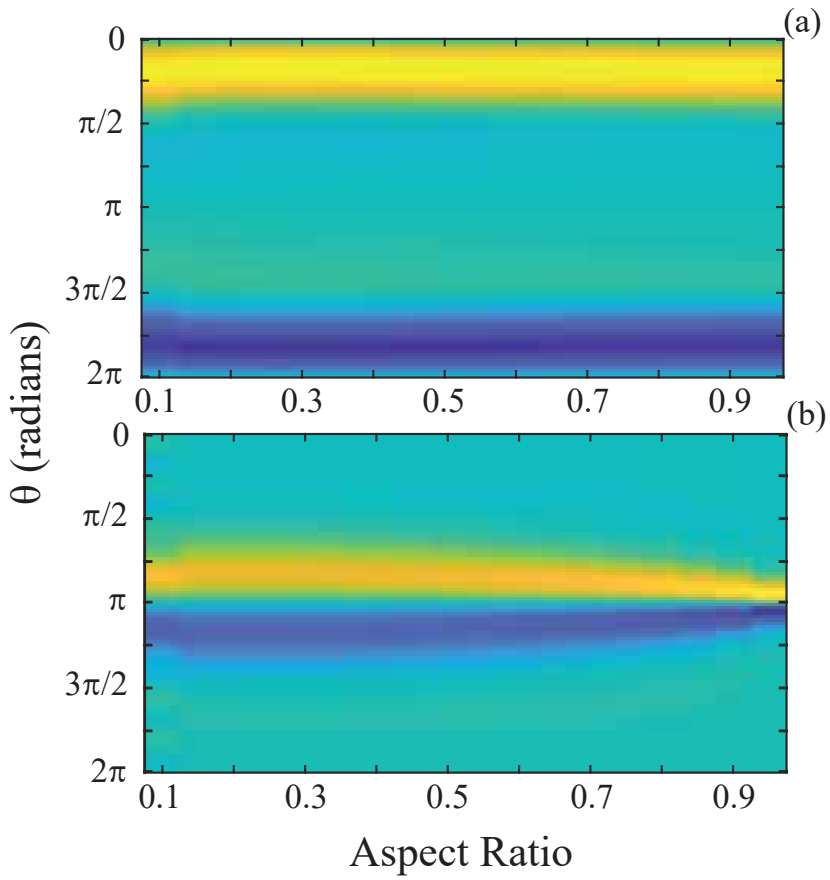


Figure 5.7: The charge distributions of the (a)$ES_1$ and (b)$IS_1$ modes as at various aspect ratios over the torus surface at different $\theta$ angle values.

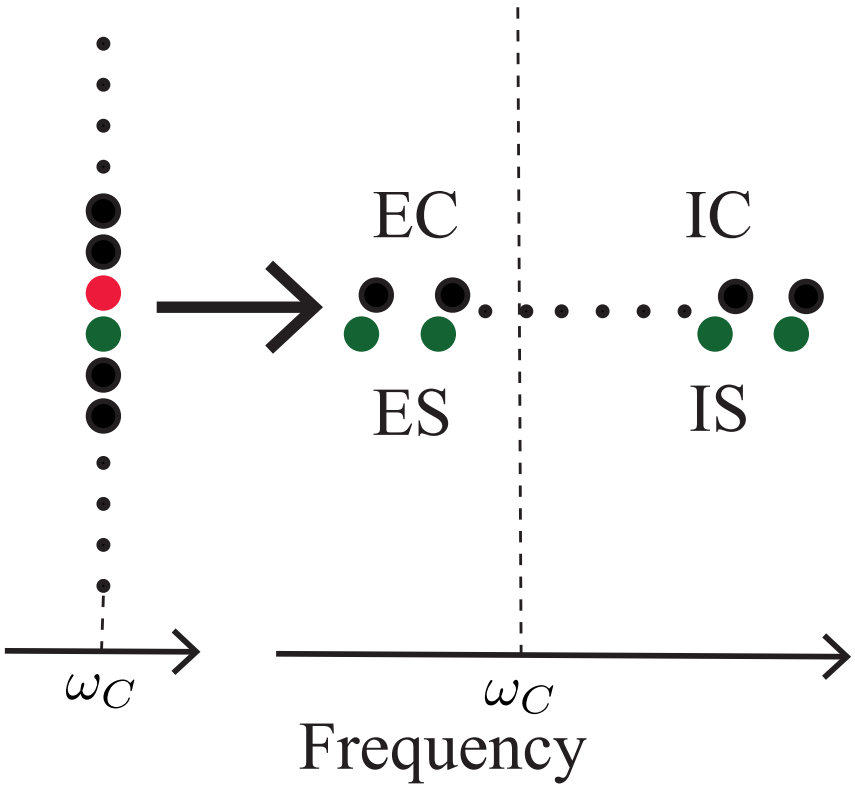


Figure 5.8: The splitting of the cylinder transverse modes into the torus poloidal modes.

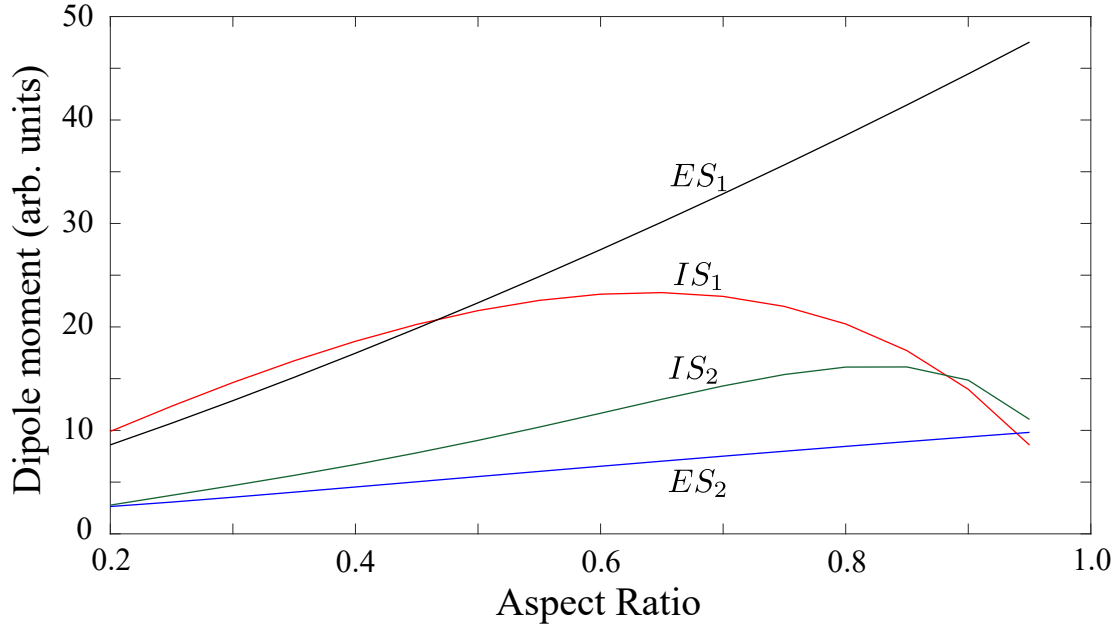


Figure 5.9: The dipole moments of the lowest order dipole active I- and E-modes at various aspect ratios.

creases. This results in a linear increase of the dipole moment with $\xi$. On the other hand, the I-modes display a linear progression at low $\xi$ values. But for higher $\xi$, the charge distribution accumulation at $\eta = \pi$ causes a reduction in the spread of the charges in the z-direction leading to smaller dipole moment values.

With the complete characterization of the poloidal modes we have established up to now, we are ready to present the full spectrum of the torus eigenmodes. In Figure 5.10, we present the full spectrum of the torus which is the counterpart of the spectrum of the sphere given in Figure 5.1. The z-dipole modes are denoted in green, with the x-modes in red and y-modes in blue. The I-modes are the highest frequency modes in this figure. For smaller $\xi$ values, the I-modes will recede into the dark mode continuum and for larger $\xi$ values, more I-modes emerge from within the dark modes. The E-modes remain hidden deeply within the dark modes. Their detuning from $\omega_C$ is also smaller as compared to the corresponding I-modes. The toroidal modes with dipole moment in x- and y-directions are

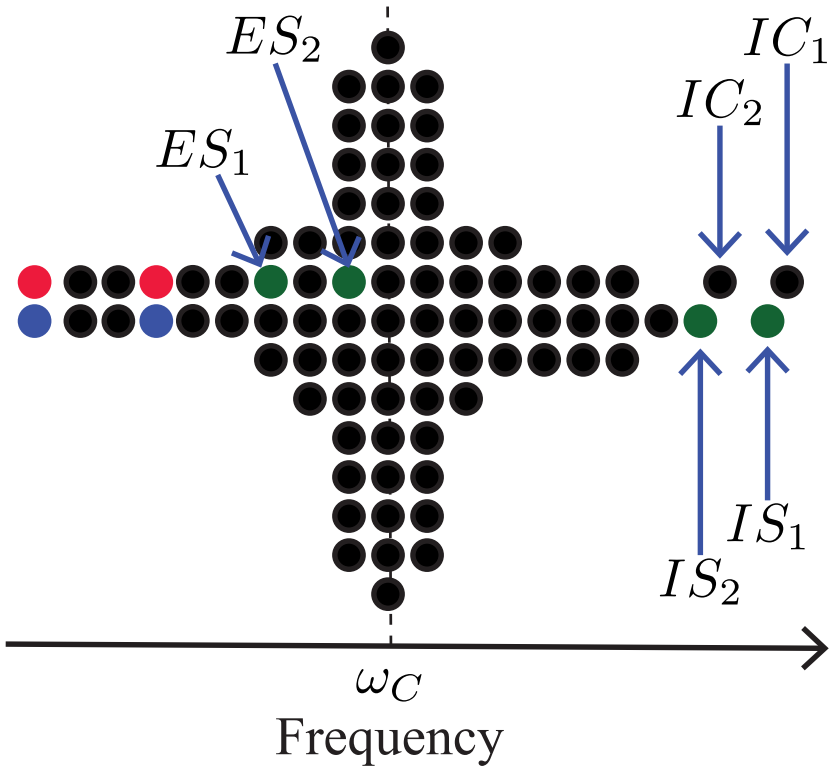


Figure 5.10: The complete spectrum of a torus. The dipole modes are shown in color while the dark modes are black. The dipole x-mode is shown in red, the y-mode in blue and the z-mode in green.

the lowest frequency modes on the torus. Unlike the I-modes, they remain the lowest frequency modes irrespective of the value of $\xi$. Higher order dipole-active toroidal modes arise from the superposition of the toroidal modes with symmetric poloidal modes. The first of these dipole active modes are also shown in the figure. All of these modes tend towards $\omega_C$ for smaller $\xi$.

## 5.3 Maxwell's equations based analysis

While we have performed an analysis of the complete modal structure of the poloidal modes, one important factor that affects the relevance of these modes to understanding the behaviour of toroidal particles under electric fields, is the fact that the modes are not orthogonal. For a spherical particle, the derived modes are completely orthogonal and hence they can be analysed individually. However, on a torus, the poloidal modes are all coupled to each other such that all $ES_l$ and $IS_l$ modes are coupled to each other. Similarly the $IC_l$ and $EC_l$ are coupled as well. Hence, in general, it is a linear combination of these modes that will be excited depending on the excitation source. However, if the modes are detuned far enough in frequency space, and the excitation source is at a specific frequency, only the modes local to the excitation frequency will be excited. As we saw earlier, the lower order $IS$ modes are quite detuned from the rest of the torus spectrum for high enough values of $\xi$. Hence they may be excited individually under such conditions.

To study this behaviour, we solve Maxwell's equations under quasi-static conditions. For this, we utilise the versatile MNPBEM toolbox [38]. The torus is placed with its axis along the z-direction. The particle is illuminated by a plane wave polarised in the z-direction. We plot the scattering and extinction cross sections in Figure 5.11 for a torus of aspect ratio 0.8. To model particle properties we use the experimental permittivity values for silver as obtained from [19]. We

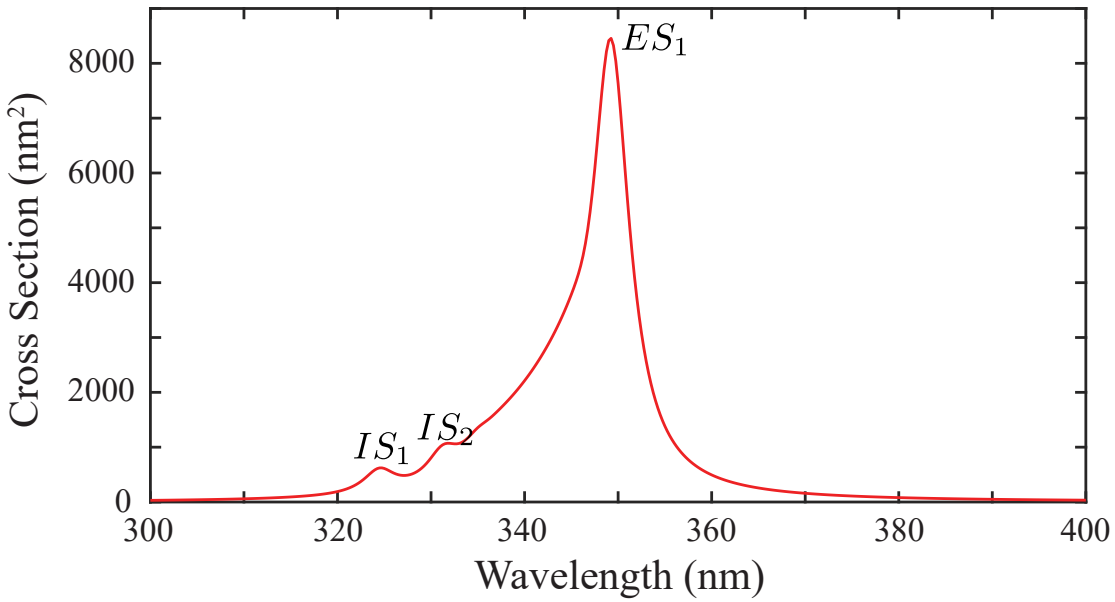


Figure 5.11: (a) The extinction cross sections for a torus with aspect ratio $\xi = 0.8$. The locations of some of the lowest order dipole active E- and I-modes are indicated by vertical bars.(b) The actual charge distributions as derived from solving Maxwell's equations under quasi-static conditions at various wavelengths.

fit that data into a Drude model and use the parameters uncovered to model the silver material. The $\omega_C$ for silver in this model lies near 343 nm. The frequencies predicted for the lowest order I- and E-modes by the numerical solution of the NP equations are also indicated in the figure. The extinction peaks correspond exactly to the dipole active lowest order modes. As expected from the higher dipole moment in Figure 5.9, the $ES_1$ mode dominates the spectrum. The $IS_1$ and $IS_2$ modes are also sufficiently detuned to be visibly separate. The rest of the E- and I-modes are overshadowed by the $ES_1$ mode response. For higher aspect ratios, more I-modes emerge from the shadow of the $ES_1$ mode. However, the dipole moments of the I-modes decrease rapidly at higher aspect ratios causing the overall response to diminish. Hence, as far as the utility of the dipole-active I-modes go, a balance needs to be stricken between obtaining a higher dipole moment and ensuring that the mode is sufficiently detuned to be visible individually.

This balance occurs around $\xi = 0.7$ to $\xi = 0.8$.

We also studied the actual induced charge distributions at each of the extinction frequency levels and verified that the induced charges resemble the charges as predicted by the NP equations(not shown). We note that while the $ES_1$ mode lies in the middle of multiple other dark and bright modes(as shown in Figure 5.10), due to its extremely high dipole moment, the E-mode dominates the interaction pattern of the torus with light polarised in the z-direction.

## 5.4 Summary and conclusion

In this chapter, we have presented our results on the poloidal plasmonic modes of a toroidal nanoparticle. We have shown the existence of two main branches of poloidal modes and that these arise from the breaking of the symmetry that occurs when an infinite cylinder is folded to create a torus. The transverse cylinder modes get split into the dual-infinity of poloidal modes on the torus resulting in the structure we observe. We also show that the poloidal modes approach the cylindrical modes in the low aspect ratio limit.

We also note that the modes we discover, the E- and the I-modes, display not only frequency localisation, but also localisation in physical space. E-modes are localised on the outside surface while the I-modes are on the inner surface with the electric fields localised accordingly. This implies that the torus carries a set of modes localised in both frequency and physical space, allowing for either frequency tuning of spatial aspects or spatial tuning of frequency aspects. This interesting modal structure is not present in other simple plasmonic structures like spheres and rods.

We have also laid the groundwork for a discussion on how the plasmonic modes of a structure may be modified by breaking of symmetries. Specifically, structures constructed by the revolution of a 2-dimensional regular shape around

a fixed axis may be studied. Elliptic cylinders, and torus-like objects with elliptical cross sections would be an excellent starting point for such investigations. While the symmetry structure of a cylinder in the polar direction in a continuous symmetry, the elliptic cylinder displays a discrete symmetry around its axis. This implies that the formation of the elliptical cross sectioned torus-like structure results in a breaking of a discrete symmetry. Thus, such an investigation will also make clear the differences between discrete and continuous symmetry breaking in plasmonic objects.

The results of this chapter have been accepted for publication at Physical Review B.

# Chapter 6
# Spasers

SPASER(Surface Plasmon Amplification by Stimulated Emission of Radiation) [23], is a device capable of generating extremely localised coherent plasmons at the nanoscale. Conceptually conceived as a nanoscale manifestation of the laser, such devices have been shown to have applications in ultramicroscopy [39], detection and spectroscopy of biological and chemical agents [40], and various other biomedical applications including cancer therapy [41]. Operating at the nanoscale, a spaser can localise light, bypassing the diffraction limit when a conventional laser dimension becomes subwavelength. It achieves this by replacing the photons in a conventional laser by plasmons, a bosonic manifestation of the coherent electronic oscillations in materials(most often a noble metal like silver or gold) under electromagnetic fields. It replaces the feedback cavity of a laser with a nanoscale particle or structure capable of supporting the plasmon modes.

A spaser, similar to a laser, operates on the concept of stimulated emission. The theory of stimulated emission suggest that the probability amplitude for an electron to de-excite emitting a photon is proportional to the number of similar bosons(photons) already present in the background field [42]. This suggests that if a gain medium could be pumped, and only a small number of similar photons could be built up, the higher quantum probability of de-excitation works as a positive feedback loop creating an avalanche of self-similar photons. Due to the similarity of these photons, the created electromagnetic field is extremely

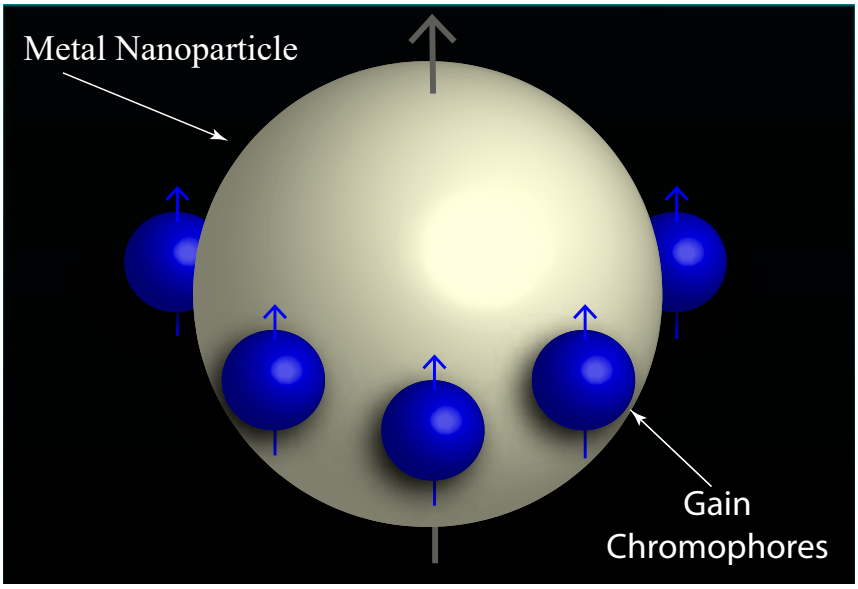


Figure 6.1: A depiction of the general plasmon-chromophore setup. The Metal Nanoparticle is at the center with the chromophores surrounding it forming an isotropic setup. This is important when we impose the assumption that the chromophores are identical. The arrows depict the assumed orientations of the dipole moments.

coherent. Replacing the background electric field with a background plasmonic medium gets us to the spaser. The oscillating electrons create an extremely coherent electric field near the spaser while the nano-scale size of the device makes the field extremely localised. Due to the length scale involved, much of the exact analysis needs to be done using exact quantum field theoretic formulations. I would also like to stress here that while the results I focus on the spaser as the central device of interest in the coming chapters, the theory and the methods I develop are applicable to any bosonic resonator coupled to fermionic gain media.

In cavity quantum electrodynamics, the model usually used to describe such coupled systems is the open Dicke model. In the next sections, we shall explore the Dicke model in detail. Without loss of generality and to establish notation and terminology used in this chapter, we present the version of the model that corresponds to two-level emitter chromophores pumped incoherently, while being

coupled to a single plasmon mode. Fig. (6.1) shows the basic arrangement of the physical system. A single Metal-Nanoparticle acts as the plasmon cavity while a constellation of chromophores are isotropically distributed around it. The dipole moments are all assumed to be collinear. The dissipative and dephasing effects of the chromophores and the plasmon mode are taken into account. The interactions between chromophores are neglected. The coupling between every chromophore and the plasmon mode is assumed to be identical and constant. The Dicke Hamil-

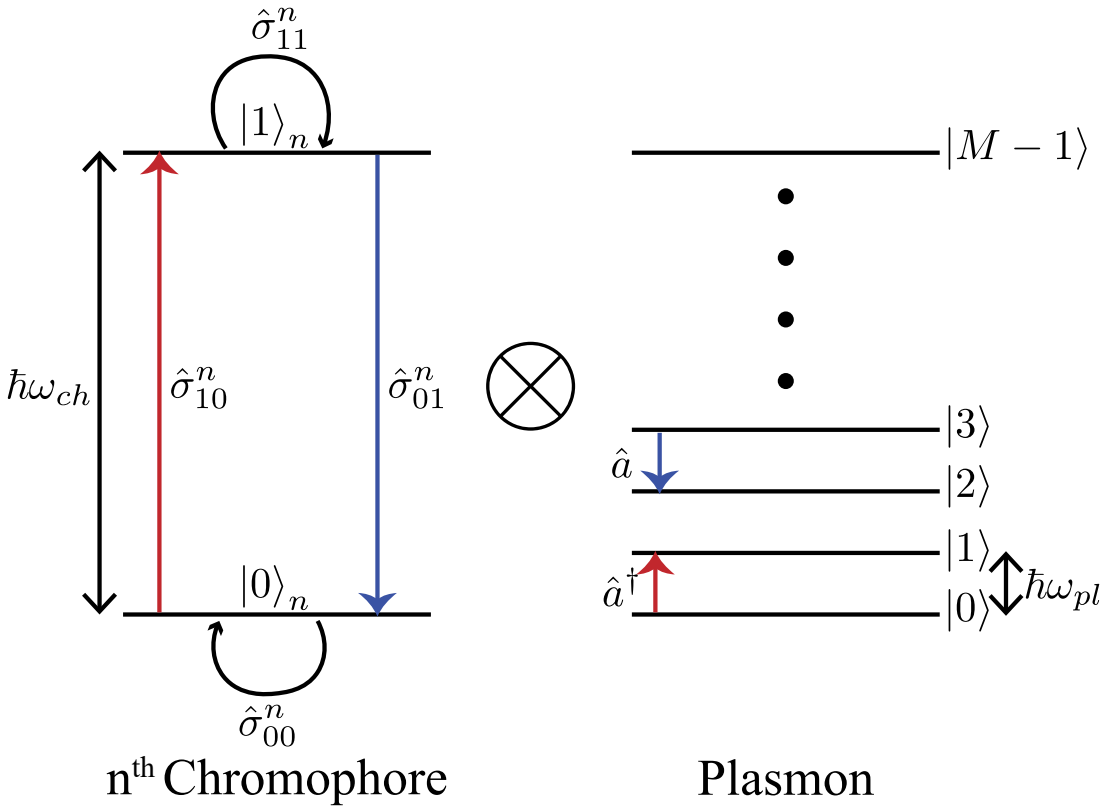


Figure 6.2: The transitions among various energy levels of a two-level chromophore system and the plasmon mode. The various operators that perform the transitions are depicted as well; $\sigma^n_{01}$ and $\hat{\sigma}^n_{10}$ for two-level systems and $\hat{a}$, $\hat{a}^\dagger$ for the plasmon system. Note that these transitions only hold for ket-vector forms. For bra-vector forms, these transitions are exactly reversed. The $\otimes$ symbol signifies the coupling of the Chromophore state vector and the Plasmon state vector through a direct product.

tonian [43] describes the evolution of the coupled chromophore-plasmon system with no interactions with the external environment taken into account. This is referred to as a closed quantum system and the equations follow the familiar unitary evolution of quantum mechanics. The Lindblad dissipators [44] modify this system to include terms that are non-unitary to include disruptive external events such as decays, pumpings and dephasings. This modified system is referred to as an open quantum system since unlike the the closed system (which is assumed to be 'closed' out from the external environment), this system is assumed to be openly coupled to an external environment which is modelled as a large bath [45]. This leads to a more realistic model containing more complex dynamics.

## 6.1 The Dicke model

In the (closed)Dicke model, the chromophore constellation, indexed by integers from 1 to $N$, is described in terms of a basis with states: $|0\rangle_n$= the ground state of the $n^{th}$ emitter and $|1\rangle_n$ = the excited state of the $n^{th}$ emitter. The operators describing transitions of the $n^{th}$ emitter can be written as, $\hat{\sigma}^n_{00} = |0\rangle_n \langle 0|_n$, $\hat{\sigma}^n_{01} = |0\rangle_n \langle 1|_n$, $\hat{\sigma}^n_{10} = |1\rangle_n \langle 0|_n$ and $\hat{\sigma}^n_{11} = |1\rangle_n \langle 1|_n$. The creation (annihilation) operator of the plasmon number state is $\hat{a}^\dagger$ ($a$). The coupling constant between the cavity mode and each chromophore is $g$ and $\hbar$ is the modified Planck's constant, $\omega_{pl}$ is the plasmon resonance frequency and $\omega_{ch}$ is the frequency corresponding to the energy gap between the ground and excited states of the two level systems. The energy level diagram for a two-level system coupled to a single plasmon mode is shown in Fig. (6.2). The composite vector of the system is formed by a straightforward direct product. The actions of the operators $\hat{\sigma}^n_{pq}$, $\hat{a}$ and $\hat{a}^\dagger$ on the chromophore and plasmon systems are also depicted in Fig. (6.2). A qualitative understanding of these processes will be useful in later derivations. The

Hamiltonian of this system reads,

$$\begin{aligned}\hat{H} &= \hbar\omega_{pl}\hat{a}^{\dagger}\hat{a} \quad \text{Free Hamiltonian of plasmon mode} \\ &+ \hbar\omega_{ch}\sum_{n=1}^{N}\hat{\sigma}_{11}^{n} \quad \text{Free Hamiltonian of chromophores} \\ &+ g\hbar(\hat{a}+\hat{a}^{\dagger})\sum_{n=1}^{N}(\hat{\sigma}_{01}^{n}+\hat{\sigma}_{10}^{n}) \quad \text{Interaction Hamiltonian.}\end{aligned}$$

The first term calculates the total energy of the plasmon mode. Here, $\hbar\omega_{pl}$ is the quantized single plasmon energy and $\hat{a}^{\dagger}\hat{a}$ is the plasmon number operator which counts the number state of the plasmon mode. The second term represents the total energy of the chromophores. The energy contribution of each chromophore is equal to $\hbar\omega_{ch}$ or 0 depending on whether the chromophore is excited ($|1\rangle_n$) or not ($|0\rangle_n$), respectively. $\hat{\sigma}_{11}^{n}$ returns is the identity operator on chromophores in state $|1\rangle_n$ and it destroys state $|0\rangle_n$. The final term in the Hamiltonian represents the interaction energy between the chromophore system and the plasmon mode.

Often, the interaction portion of the Dicke Hamiltonian is simplified using the so-called rotating wave approximation (RWA) [46] to yield the rotating wave approximated interaction Hamiltonian, $H_{RWA}$:

$$\hat{H}_{RWA} = \hbar g\sum_{n=1}^{N}(\hat{a}^{\dagger}\hat{\sigma}_{01}^{n}+\hat{a}\hat{\sigma}_{10}^{n}). \tag{6.1}$$

The RWA approximation has proven to be extremely useful [47] and does not significantly alter the results due to the extremely small matrix elements associated with the terms that are discarded. However, the RWA has been shown to fail to make accurate predictions when the coupling between the emitters and the cavity is strong [48]. Not using the RWA has also shown to predict interesting phenomena in such diverse areas as quantum chaos [49], spontaneous emission theory [50] and qubit-oscillator coupling [51]. But the dimensionality reduction

proposed in [52] is not affected by whether RWA is used or not. The formalism still holds while adding extra terms to the equations. Using this RWA form of the Hamiltonian, the equation of motion for the density matrix can be derived for the full density matrix of the closed system through [23],

$$\dot{\hat{\rho}} = \frac{1}{i\hbar}[\hat{H}, \hat{\rho}]. \tag{6.2}$$

## 6.2 Dissipations and the open Dicke model

Whilst the closed Dicke Model accounts for a lot a of the naturally occurring phenomena, it does not take into account the possibility of dissipation due to the unavoidable couplings of the system to the environment. These effects can be systematically modelled using the Lindblad equation and it's associated Lindblad dissipators [45]. The model modified using these dissipators are referred to as the open Dicke model. The Lindblad dissipator formalism allows for the codification of spontaneous events that result from various incoherent couplings of the system to the environment. These events are modelled as non-unitary evolution terms added to the original density matrix evolution equation 6.2. Every such spontaneous event can be described under the Lindblad formalism using the operator that describes the effect of the event on the system ($\hat{A}_j$), and the mean rate at which this event occurs ($\gamma$). For example, the incoherent pumping of the $n^{th}$ chromophore from level **0** to level **1** at a rate of 2 Hz in our model can be codified by $\hat{A}_j = \hat{\sigma}^n_{10}$ - which is the level **0** to level **1** transition operator in our model, and $\gamma = 2$. Hence, in the interaction picture, the open system Hamiltonian can be expressed as,

$$H_{RWA} = \hbar g \sum_{n=1}^{N} (\hat{a}^\dagger \hat{\sigma}^n_{01} + \hat{a}\hat{\sigma}^n_{10}) + \sum_j D[\hat{A}_j]\hat{\rho}. \tag{6.3}$$

Here the $D[\hat{A}_j]$ represent the Lindblad super-operators acting on the density matrix. It has been shown that a Lindblad super-operator can be generally represented as,

$$D[\hat{A}_j]\rho = \frac{\gamma}{2}(2\hat{A}_j\rho\hat{A}_j^\dagger - \rho\hat{A}_j\hat{A}_j^\dagger - \hat{A}_j^\dagger\hat{A}_j\rho). \tag{6.4}$$

And using the various forms for the $\hat{A}_j$, incoherent/dissipative processes such as Incoherent Pumping ($\hat{A}_j = \hat{\sigma}_{10}^n$), Spontaneous Plasmon Decay ($\hat{A}_j = \hat{a}$) and Radiative Spontaneous Decay of Chromophores ($\hat{A}_j = \hat{\sigma}_{01}^n$) can be modelled.

We can vectorize the density matrix elements and express the final equation to be solved in this open Dicke model in the form,

$$\dot{\hat{\mathcal{Q}}} = A\hat{\mathcal{Q}}. \tag{6.5}$$

Here, matrix $A$ is a large, sparse, constant, asymmetric matrix consisting of constant values. This equation can be easily solved using a multitude of methods if not for the extreme size of the problem.

## 6.3 Computational Complexity

Due to nature of the density matrix, the open system Dicke Model has exponentially scaling dimensions. To see this, consider the density matrix of a general $N$ chromophore system with the plasmon number state truncated to length $M$. The number of elements in the chromophore subspace state vector would be $2^N$ due to each chromophore having 2 degrees of freedom. This is a direct consequence of each chromophore having 2 energy levels and hence two possible states. The plasmon state theoretically has infinite degrees of freedom and due to the finite computational resources, truncating the size of the plasmon number states is essential. Usually, choosing the highest value such that the system properties are accurate to within a required precision is done. But this is non-trivial since the

calculation of system properties usually require an estimate of $M$ (we present our solution to the problem of determining an optimal value for $M$ in the next chapter). The plasmon subspace vector would thus have size $M$ due to having $M$ possible states. Thus the total state vector dimensions would be $2^N \times M$. The full density matrix would thus have dimensions $(2^N \times M) \times (2^N \times M) = 4^N \times M^2$. This renders the full system intractable to any numerical method and hence has no value in utilizing it for any practical predictions or insights.

# Chapter 7
# Solving spasing systems

As mentioned in the previous section, the open Dicke model can be formulated as a set of first order constant coefficient differential equations of dimensions $4^N \times M^2$. Hence the problem becomes one of solving a very large system of differential equations. But solving such a system becomes ridiculously tedious beyond a couple of chromophores: for example, a system with $N = 10$ chromophores and a plasmon state cut-off at $M = 100$ requires so much computational space that the storage of the matrix $A$ alone would require over 7 TB of data. This renders the full system intractable to any numerical method and hence has no value in utilizing it for any practical predictions or insights. Despite this, there exist methods to solve the system of equations for extremely small system sizes. These methods are summarised in Appedix C.

However, it has been known for some time now that polynomial scaling is achievable in the context of identical chromophores [53, 54] ($O(N^3)$). Most recently, work done on Generalized Dicke basis states from a group theoretic point of view, has demonstrated an exploitable symmetry within the dissipative two-level system [55] which effectively results in polynomial scaling of the dimensions of the problem. Hartmann [55] uses the fundamental representation of the SU(4) group originally devised to explain the flavour quark model of particle physics, to derive a representation of fully-symmetrical states, which essentially means states that are symmetric under interchange of chromophores. In general,

such states would be formed by linear combinations of pure-states that are related by the symmetry operation of chromophore interchange. The representation used in [55] succeeds in describing such states using just 3 quantum numbers, which leads to the effective $O(N^3)$ scaling of the density matrix size.

This knowledge has led to related work that directly uses this symmetry to reduce the dimensions of the problem significantly. Richter *et al.* [52] have been successful in using this reduction to obtain solutions for emitter-cavity problems with up to 30 emitters within reasonable time periods using high performance computing platforms [52].

## 7.1 Density Matrix Representation and the identical emitter approximation

In this section we shall discuss the form the density matrix takes when the indistinguishability of chromophores are taken into account. The restructuring of the density matrix in this new form will shed light on the reduction of the density matrix size of the problem from exponential to cubic in the number of emitters and quadratic in the number of plasmon number states. The general tensor product chromophore-plasmon quantum state can be expressed as follows,

$$|x\rangle = \{\prod_n |x_n\rangle_n\} \otimes |k\rangle \,, \tag{7.1}$$

where $|k\rangle$ is the plasmon number state and $|x_n\rangle_n$ is the state of emitter $n$ with $x_n = \{0, 1\}$ depending on whether emitter $n$ is grounded or excited respectively. The tensor product of these states indicate the independent presence of all the different chromophores and the plasmon mode together. Mathematically this tensor product signifies the amalgamation of the independent Hilbert Spaces associated with the different chromophores and the plasmon mode. This allows us to treat

the composite system as one single entity. Using this, the form of the density matrix can be represented as,

$$\begin{aligned}\hat{\rho} &= |x\rangle \langle y| \,. \\ &= \{\prod_n |x_n\rangle_n\} \otimes |k\rangle \{\prod_n \langle y_n|_n\} \otimes \langle p| \\ &= |x_1\rangle_1 |x_2\rangle_2 ... |x_N\rangle_N |k\rangle \langle y_1|_1 \langle y_2|_2 ... \langle y_N|_N \langle p| \,.\end{aligned} \tag{7.2}$$

But this is exactly the basis with exponential dimensions we presented earlier and cannot be used for numerical simulations. By using the fully-symmetrised states, we can describe a general density matrix element using the notation proposed in [52].

To see how this is possible, consider the following. We can obviously describe the complete chromophore system in Eq. (7.2) by describing the complete set of values of $\{x_n,y_n\}$. But $\{x_n,y_n\}$ can only take 4 different values, $(0,0)$, $(0,1)$, $(1,0)$ and $(1,1)$. Since all chromophores are identical, we can discard all information about the identity of the emitters and keep count of the cardinalities of each of the sets with different values of $\{x_n,y_n\}$. Under this formalism we define the quantities $\{n_{uv}\}$ as $n_{uv}$ = number of emitters $|\alpha\rangle_n \langle\beta|_n$ with $\alpha = u$ in $|x\rangle$ and $\beta = v$ in $|y\rangle$. Note that these quantities add up to $N$ and so, $n_{00} = N - n_{11} - n_{10} - n_{01}$. Using this notation, the modified density matrix can be described as follows (discarding the redundant information in $n_{00}$):

$$\hat{\rho} = \hat{\rho}[n_{11}, n_{01}, n_{10}; k, p] = |n_{11}, n_{10}, n_{01}, k\rangle \langle n_{11}, n_{10}, n_{01}, p| \,. \tag{7.3}$$

These numbers are related to the three quantum numbers derived by Hartmann $\{q, q_3, \sigma_3\}$ [55] through,

$$q = \frac{n_{11} + n_{00}}{2} = \frac{N - n_{10} - n_{01}}{2}, \tag{7.4a}$$

$$q_3 = \frac{n_{11} - n_{00}}{2} = \frac{n_{11} + n_{10} + n_{01} - N}{2}, \tag{7.4b}$$

$$\sigma_3 = \frac{n_{10} - n_{01}}{2}. \tag{7.4c}$$

The density matrix described using the above quantum numbers are reminiscent of the traditional Dicke basis quantum numbers. They have been aptly named "Generalised Dicke States" [55].

In Eq. 7.3, $\hat{\rho}[n_{11}, n_{01}, n_{10}; k, p] = |n_{11}, n_{10}, n_{01}, k\rangle \langle n_{11}, n_{10}, n_{01}, p|$ denotes any one of the density matrix components that satisfy the conditions dictated by the $n_{11}$, $n_{01}$, $n_{10}$, $k$ and $p$ values. This method of denoting any of a number of density matrix components by a single modified component is justified, since all of the density matrix elements of the full system with the same $n_{uv}$ and photon number states have identical values.The number of such similar density elements can be calculated to be the number of different ways in which 4 distinguishable sets of objects, corresponding to the 4 different $n_{uv}$, whose numbers add up to $N$, can be arranged in a row. The objects are indistinguishable within the sets. The type of object assigned to the $n^{th}$ position in the row determines the $\{x_n,y_n\}$ value pair of the density matrix element. This quantity can be expressed using the multinomial coefficient,

$$\mathcal{C}(n_{11}, n_{01}, n_{10}) = \frac{N!}{n_{11}!n_{01}!n_{10}!(N - n_{11} - n_{10} - n_{01})!}, \tag{7.5}$$

where $N$ is the total number of chromophores.

Since we aggregate all of the density matrix elements related to each other by the symmetry relation, the modified basis elements of the density matrix needs to be scaled by $\mathcal{C}(n_{11}, n_{01}, n_{10})$ to reflect their true value. Hence the true modified basis for the density matrix system can be expressed as,

$$\hat{\mathcal{P}}[n_{11}, n_{01}, n_{10}; k, p] = \mathcal{C}(n_{11}, n_{01}, n_{10}) \times \hat{\rho}[n_{11}, n_{01}, n_{10}; k, p]. \tag{7.6}$$

Consider a two-chromophore system as a concrete example. Due to the indistin-

guishability of the chromophores, we can use the modified density matrix form $\hat{\mathcal{P}}[n_{11}, n_{01}, n_{10}; k, p]$. Consider the component $\hat{\mathcal{P}}[1,1,0;k,p]$. While this is a single component in the modified picture, it stands for the sum of two different but identically valued (again, due to the chromophores themselves being identical) density matrix elements,

$$\begin{aligned}\hat{\mathcal{P}}[1,1,0;k,p] &= \mathcal{C}(1,1,0) \times \hat{\rho}[1,1,0;k,p] \\ &= |1\rangle_1 |0\rangle_2 \langle 1|_1 \langle 1|_2 + |0\rangle_1 |1\rangle_2 \langle 1|_1 \langle 1|_2 .\end{aligned} \tag{7.7}$$

This basis has shown to be complete for the Lindblad dissipator based equations modelling identical chromophores [55]. Using this basis, it can also be shown that the portion contributed by the incoherent pumping at rate $P$, to the evolution equations can be expressed in the following form (in the interaction picture), The interaction Hamiltonian contribution:

$$\begin{aligned}\dot{\mathcal{P}}[n_{11}, n_{01}, n_{10}; k, p] = ig\{&(n_{01}+1)\sqrt{k+1}\mathcal{P}[n_{11}-1, n_{01}+1, n_{10}; k+1, p] \\ &+ (n_{00}+1)\sqrt{k+1}\mathcal{P}[n_{11}, n_{01}, n_{10}-1; k+1, p] \\ &+ (n_{10}+1)\sqrt{k}\mathcal{P}[n_{11}, n_{01}, n_{10}+1; k-1, p] \\ &+ (n_{11}+1)\sqrt{k}\mathcal{P}[n_{11}+1, n_{01}-1, n_{10}; k-1, p] \\ &- (n_{10}+1)\sqrt{p+1}\mathcal{P}[n_{11}-1, n_{01}, n_{10}+1; k, p+1] \\ &- (n_{00}+1)\sqrt{p+1}\mathcal{P}[n_{11}, n_{01}-1, n_{10}; k, p+1] \\ &- (n_{01}+1)\sqrt{p}\mathcal{P}[n_{11}, n_{01}+1, n_{10}; k, p-1] \\ &- (n_{11}+1)\sqrt{p}\mathcal{P}[n_{11}+1, n_{01}, n_{10}-1; k, p-1]\}\end{aligned} \tag{7.8a}$$

$$\begin{aligned}\dot{\hat{\mathcal{P}}}[n_{11}, n_{01}, n_{10}; k, p] = \frac{P}{2}\{&2(n_{00}+1)\hat{\mathcal{P}}[n_{11}-1, n_{01}, n_{10}; k, p] \\ &- (2n_{00}+n_{01}+n_{10})\hat{\mathcal{P}}[n_{11}, n_{01}, n_{10}; k, p]\}.\end{aligned} \tag{7.8b}$$

Spontaneous Plasmon Decay:

$$\begin{aligned}\dot{\mathcal{P}}[n_{11}, n_{01}, n_{10}; k, p] = \frac{\gamma_{pl}}{2}\{2\sqrt{(k+1)(p+1)}\mathcal{P}[n_{11}, n_{01}, n_{10}; k+1, p+1] \\ - (k+p)\mathcal{P}[n_{11}, n_{01}, n_{10}; k, p]\}\end{aligned} \tag{7.8c}$$

Radiative Spontaneous Decay of Chromophores:

$$\begin{aligned}\dot{\mathcal{P}}[n_{11}, n_{01}, n_{10}; k, p] = \frac{\gamma_{ch}}{2}\{2(n_{11}+1)\mathcal{P}[n_{11}+1, n_{01}, n_{10}; k, p] \\ - (2n_{11} + n_{01} + n_{10})\mathcal{P}[n_{11}, n_{01}, n_{10}; k, p]\}\end{aligned} \tag{7.8d}$$

We have assumed $g =$ coupling constant between the plasmon and a chromophore, $P =$ incoherent pumping rate of chromophores, $\gamma_{ch} =$ chromophore spontaneous decay rate and $\gamma_{pl} =$ cavity plasmon decay rate. All of these values are system dependent parameters that depend on the materials and the geometry of the setup.

In this modified density matrix model, the dimensionality of the chromophore subspace is heavily reduced from the exponential dimensions of the full system to polynomially scaling dimensions. The number of elements in the density matrix is equal to the cardinality of the set $\{(n_{11}, n_{01}, n_{10}) : n_{11} + n_{01} + n_{10} \leq N \wedge n_{11}, n_{01}, n_{10} \geq 0\}$. Combinatorial analysis gives the answer to be equal to $\binom{N+3}{3}$, or,

$$\frac{N^3 + 6N^2 + 11N + 6}{6}. \tag{7.9}$$

This demonstrates the $O(N^3)$ scaling of the modified density matrix. The dimensionality of the plasmon subspace can be deduced from the different possible values of the variables $k$ and $p$. For each $k$ value, $p$ takes on $M$ different values. $k$ itself can take on $M$ independent values. Hence the plasmon subspace has number of elements equal to $M \times M = M^2$. Since the plasmon and chromophore subspaces are independent, the total dimensions of the modified density matrix

as described by Eq. (7.6) is equal to,

$$C_{full} = \frac{N^3 + 6N^2 + 11N + 6}{6} \times M^2. \tag{7.10}$$

The Open Quantum System we have presented up to now uses various assumptions and approximations. The three main ones are, the Born Markov Approximation (BMA), the Rotating Wave Approximation (RWA) and the Identical emitter approximation.

The Born Approximation allows us to consider the environment as approximately constant throughout the interaction period. This implies that while the system is affected by the environment, a significant reciprocal effect does not occur on the environment. This is a fair assumption especially when the external environment is not too tightly confined. In such a cases when the environment does indeed depend on the system, a more complex quantum description would be needed treating both the system and the environment as systems of interest.

The Markov Assumption implies that the timescale of decays in the system is far greater than the interaction timescale. This allows for the environment to lose memory of the system fast enough so that interactions and dissipations remain purely system state-dependent. Similar to the Born approximation, the violation of the Markov approximation would significantly convolute the description of the system requiring a formalism that treats both the environment and system together as a whole instead of as a smaller subsystem existing within an unchanging bath.

These two approximations are collectively referred to as the Born-Markov Approximation (BMA), it is inherited due to the use of the Lindblad formalism. The Lindblad formalism uses results from Quantum Measurement Theory to decouple the system-environment coupling by leveraging the consequences of the BMA [45].

The Identical Emitter Assumption arises from the problem statement itself. All parameters describing emitters are assumed to be identical. This also entails the assumption that all the states the system goes through in its time evolution is symmetric with respect to emitter interchange. Specifically, only initial states that are completely symmetric and that do not distinguish between emitters are allowed. Given that, as demonstrated in [55], any intermediate state of the system will be fully symmetric as well. However, this approximation will be violated in cases where molecules are not symmetrically placed with respect to the nanoparticle. Hence, the methods of this chapter would not be useful and other approximation schemes such as the Reduced Density Matrix(RDM) [56] approach will have to be sought.

In addition to this, we make the assumption that all chromophores are identical with identical energy levels. This is not valid for practical dye chromophores. There is slight variations in the energy levels and the energy separations in a chromophore population. It has been shown that the random variations in the energy levels actually do not change the basic form of the dynamics [57]. Such effects can be easily incorporated by using a modified energy level scale based on the actual energy level distribution.

### 7.1.1 Solution Algorithm for the Equations

Equations (7.8) form a set of first order coupled ordinary differential equations in the dependent variable $\hat{\mathcal{P}}[n_{11}, n_{01}, n_{10}; k, p]$. There are $C_{full}$ number of elements in this dependent variable as given by Eq. (7.10). The main solution algorithm we use is expressed in Algorithm (2).

The first step in the solution scheme involves calculating the maximum estimated size of the plasmon number state. For estimating the maximum value of the plasmon number state, we use the Reduced Density Matrix (RDM) equation

technique for identical chromophores as developed in [56]. Using the plasmon distribution peak value $M_{peak}$ value as calculated through that method, we use the following equations to estimate the value of $M$;

$$M_{peak} = \frac{N(P - \gamma_{ch})}{2\gamma_{pl}} - \frac{P + \gamma_{ch}{}^2}{8g^2}, \tag{7.11a}$$

$$M = \lceil M_{peak} \times 2 \rceil. \tag{7.11b}$$

This aids in bypassing a trial and error method which requires us to test out various values for $M$ until a suitable value is found. We note here that this implies an $O(N)$ scaling of the size of the plasmon subspace. It is also worth noting that this value of $M_{peak}$ gives a gross estimate of the mean plasmon value for peaked distributions.

Next, we re-cast the problem in linear algebraic form to be able to handle the multiple dimensions of the problem efficiently. Hence, we linearize the elements of $\mathcal{P}$, which amounts to determining where each element goes when the elements of $\mathcal{P}$ are arranged as a vector (we shall refer to the position indices of the vector by $\theta$). In other words, we need to determine an indexing scheme for the ordering of the elements of $\mathcal{P}$. Ideally, an indexing scheme should be able to deterministically calculate the $\{n_{11}, n_{01}, n_{10}, k, p\}$ tuple given $\theta$ and vice versa. But in our problem, indexing is non-trivial because the internal variables $n_{11}$, $n_{01}$ and $n_{10}$ are dependent through the inequality $n_{11} + n_{01} + n_{10} \leq N$ ($k$ and $p$ do not impose this difficulty because they take on values independently of each other). Had $n_{11}$, $n_{01}$ and $n_{10}$ been independent, indexing and mapping the elements of $\mathcal{P}$ to a sequential scheme would have been straightforward. But, as things stand, storing these elements in a sequential storage scheme on a computer and simultaneously accessing them in constant time are not both trivial. Thus, we make a choice by opting to store elements of the variable sequentially in our simulations. This forces us to maintain a mapping $\{n_{11}, n_{01}, n_{10}, k, p\} \mapsto \theta$ in a separate vari-

able. The mapping we used is expressed in Algorithm 1. This sequential storage strategy of the vectorized $\mathcal{P}$ allows us to perform linear algebraic routines on it much more efficiently. Utilizing this vectorization scheme, the general form of the equations of motion for the density matrix can be expressed compactly as:

$$\dot{\hat{\mathcal{Q}}} = A\hat{\mathcal{Q}}, \tag{7.12}$$

where $\hat{\mathcal{Q}}$ is the vectorized version of the modified density matrix $\hat{\mathcal{P}}$, and $A$ is the Jacobian matrix of the system indicating the dependencies between the various $\hat{\mathcal{P}}$ elements and the exact complex valued weight of these dependencies. Values of $A$ are completely determined by the Eqs. (7.8) and it turns out to be a constant, complex valued, extremely sparse (with at most 13 non-zeros per row), non-Hermitian, square matrix. The general form and order of the elements of $\mathcal{P}$ are illustrated in Fig. (7.1). The form of matrix $A$ is illustrated in Fig. (7.2).

**Algorithm 1** Mapper

```
1: procedure CreateMap(N, M)        ▷ Calculate the index mapping for an N chromophore system with a plasmon state cutoff of size M
2:     Map ← Initial empty map
3:     θ = 0
4:     for n11=0 to N do
5:         for n01=0 to N − n11 do
6:             for n10=0 to N − n01 − n11 do
7:                 for k=0 to M − 1 do
8:                     for p=0 to M − 1 do
9:                         Map ← {{n11, n01, n10, k, p}, i}
10:                        θ = θ + 1
11:                    end for
12:                end for
13:            end for
14:        end for
15:    end for
16:    return Map                    ▷ The final Map
17: end procedure
```

$$\hat{\mathcal{P}}(n_{11}, n_{01}, n_{10}; k, p) = \begin{bmatrix} \mathcal{P}(0,0,0;0,0) \\ \mathcal{P}(0,0,0;0,1) \\ \mathcal{P}(0,0,0;0,2) \\ \vdots \\ \mathcal{P}(0,0,0;0,M-1) \\ \mathcal{P}(0,0,0;1,0) \\ \vdots \\ \mathcal{P}(0,0,0;M-1,M-1) \\ \vdots \\ \mathcal{P}(1,0,0;0,0) \\ \vdots \\ \mathcal{P}(1,1,0;0,0) \\ \vdots \\ \mathcal{P}(1,1,1;0,0) \\ \vdots \\ \mathcal{P}(1,1,N-2;0,0) \\ \vdots \\ \mathcal{P}(N,0,0;0,0) \\ \vdots \\ \mathcal{P}(N,0,0;M-1,M-1) \end{bmatrix}$$

Figure 7.1: The ordering of the linearized version of the modified density matrix elements is shown. The ordering is determined according to Algorithm 1. While this scheme enables storing the density matrix elements in a linear storage scheme with constant time access, retrieving the positioning of individual density matrix elements is not trivial. We propose maintaining a Map variable for storing the individual position information.

Only the top-left corner of the matrix is shown here and the rest of the elements can be inferred by the ordering scheme given in Algorithm 1. Due to the form of the Eqs. 7.8, $A$ turns out to be an extremely sparse(with at most 13 non-zeros per-row), non-Hermitian, complex valued, square matrix.

Right after the indices are set up, we calculate the Jacobian matrix $A$ and perform a bandwidth reducing reordering of the matrix elements. This improves the efficiency of the matrix-vector product in Eqs. (7.12) by improving cache performance [58]. Reordering requires modifying the mapping we already maintain

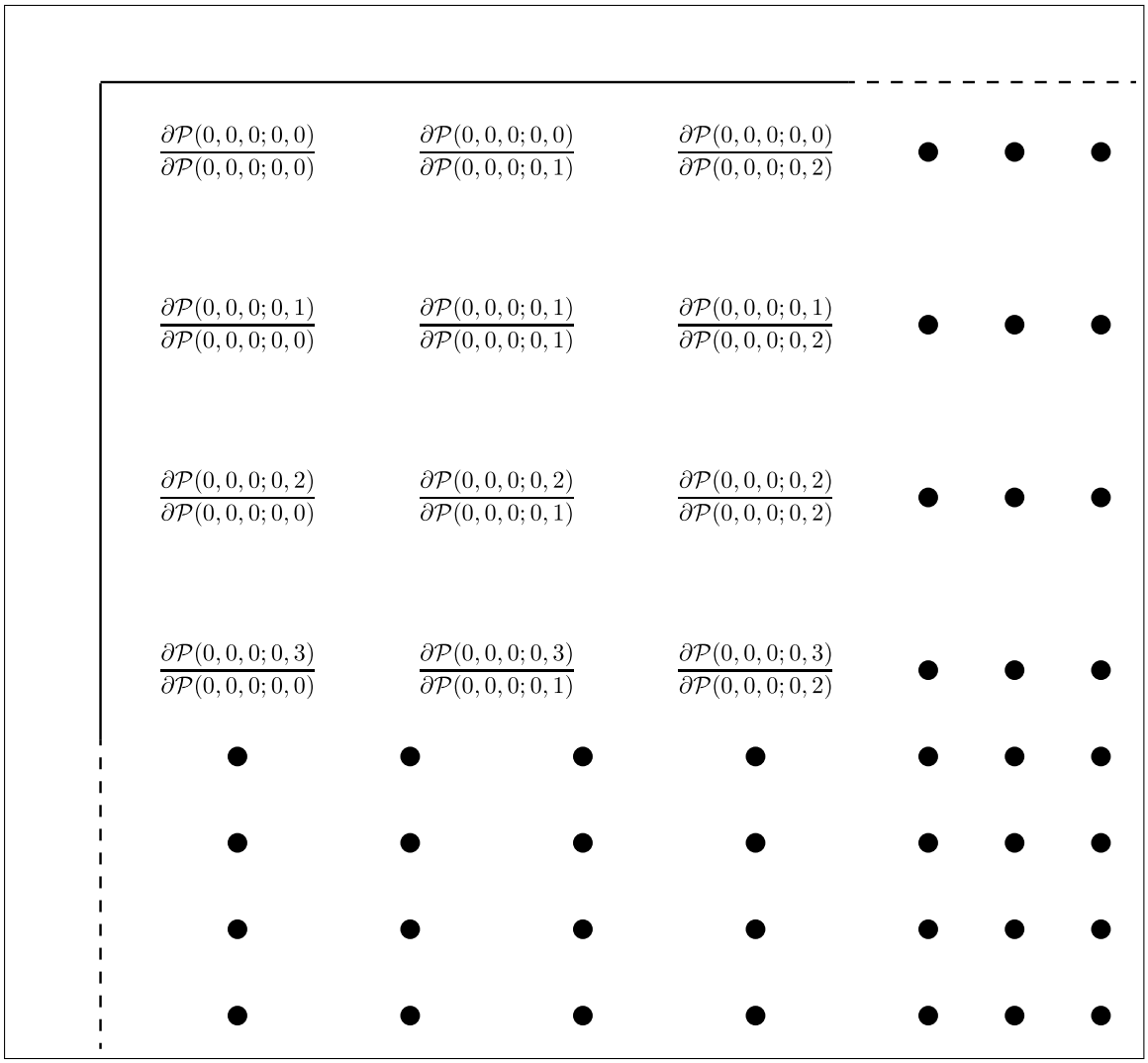


Figure 7.2: The general form of the Jacobian matrix $A$. The partial derivative values are obtained from the system of Eqs. 7.8. Here, only the top-left corner of the matrix is shown for clarity. The ordering of the elements is determined by Algorithm 1 as with the vectorized density matrix. The values of this matrix are complex valued constants for a given Spasing setup. Note that most of the values are zero making the matrix significantly sparse.

and the order of elements in both $\hat{\mathcal{Q}}$ and $A$. Afterwards, we calculate the initial density matrix which is taken to be the thermodynamic ground state in all our simulations.

Next, we solve the equations as a system of first order differential equations

using time-stepping. Eqs. (7.12) are used to evaluate $\hat{\mathcal{Q}}(t+\delta t)$ using the $\hat{\mathcal{Q}}(t)$ value from the previous iteration. Various Runge-Kutta schemes, with constant or adaptive step sizing can be used. To solve for the steady state density matrix, the integration can be run until the density matrix values converge. The basic setup of this method when using an adaptive Runge-Kutta scheme is shown in Algorithm 2. As indicated by Eqs. (7.12), the equations of motion for a general

**Algorithm 2** Adaptive Runge-Kutta based Steady State Solver

**procedure** RK-STEADY-STATE($N, P, SystemParameters$) ▷ Calculate steady state solution of an $N$ chromophore system pumped incoherently at rate $P$
  $M \leftarrow$ RDM estimated plasmon number state size
  $Map \leftarrow CreateMap(N, M)$
  $A \leftarrow$ Jacobian matrix
  $Map \leftarrow Reordering(A)$ ▷ Calculate a reordering of the indices of matrix $A$ to reduce bandwidth.
  $Reorder(A)$ ▷ Reorder $A$ according to the new ordering.
  $\rho(t=0) \leftarrow$ Initial ground state distribution
  $t_{next} = t_{previous} = 0$
  $\rho(t_{next}) = \rho(t_{previous})$
  **do**
    $t_{previous} = t_{next}$
    $\rho(t_{previous}) = \rho(t_{next})$
    $t_{next}, \rho(t_{next}) \leftarrow RK - TimeStepper(A, \rho(t_{previous}))$
  **while** $\rho(t_{previous}) \neq \rho(t_{next})$ ▷ While not converged
  **return** $\rho(t_{final}) = \rho(t_{next})$ ▷ Final steady state density matrix
**end procedure**

density variable component $\hat{\mathcal{Q}}[n_{11}, n_{01}, n_{10}; k, p]$ are built off of linear operations on the internal variables of $\hat{\mathcal{Q}}$ resulting in "dependency connections" between different $\hat{\mathcal{Q}}(\cdot)$ components. We will be using the terminology "connection" to illustrate this dependency between the components. Since each density variable increases or decreases in value dependent on the value of other density matrix elements "connected" to it, and because total density is conserved (equal to 1), Eqs. (7.12) can be interpreted as an equation expressing the flow/exchange of density between different density matrix elements.

Further information on the solver and the techniques used is avaialble in Appendix E.

## 7.2 Modified identical emitter approximation

In the exact numerical model that we presented so far, the dimensions of the plasmon subspace of the density matrix is $M^2$ where $M$ is the size of the truncated plasmon number state. But the inherent symmetries of the equations allow for the reduction of this size down to $O(M)$ under special conditions. To see this, consider the following argument: Take a general component of the density matrix model $\hat{\mathcal{Q}}[n_{11}, n_{01}, n_{10}; k, p]$. If we define $\kappa_2(\hat{\mathcal{Q}}) = (n_{01} - n_{10}) - (k - p)$, it is clear that in all equations, $\dot{\hat{\mathcal{Q}}}$ is only connected to other density components with the same $\kappa_2(\cdot)$ value. It is easy to see that this relationship satisfies the three requirements of an equivalence relation: reflexivity, symmetry and transitivity due to $\kappa_2(\cdot)$ being a many-to-one real valued function $\kappa_2 : \{(n_{11}, n_{01}, n_{10}) : n_{11} + n_{01} + n_{10} \leq N \wedge n_{11}, n_{01}, n_{10} \leq 0\} \mapsto \mathbb{R}$.

This implies that the connections are only formed between density matrix components with the same $\kappa_2$ value. Hence, the flow/exchange of density between different density components through Eq. (6.2) will occur only if they reside in the same equivalence class with respect to $\kappa_2$. So we see that the space of all components of $\hat{\mathcal{Q}}$ gets subdivided into equivalence classes based on their $\kappa_2$ values. In our present treatment, we only consider systems evolving from the thermodynamic ground state. Since only variables with $\kappa_2(\cdot) = 0$ are non-zero in the ground state, variables with all other values of $\kappa_2$ will remain zero throughout the entire evolution of the system. This leads to the following simple linear relation which effectively removes one of the variables and hence one cavity photon

number state dimension from the analysis,

$$\kappa_2 = (n_{01} - n_{10}) - (k - p) = 0. \tag{7.13}$$

In a general plasmon subspace density matrix, the different elements are indexed by $p$ and $k$. The values of $k$ and $p$ range from 0 to $M-1$ such that each value of $k$ is coupled to $M$ different values of $p$. This results in $M \times M = M^2$ total size of the plasmon subspace of the density matrix. This is the origin of the $M^2$ portion of the size in Eq. (7.10). But Eq. (7.13) demonstrates that, given $n_{01}$ and $n_{10}$, only one density matrix element indexed by a distinct value of $p$ couples to each $k$ value non-trivially. All other elements of the density matrix denoted by the other $p$ values are identically zero throughout the evolution of the system. This unique value of $p$ is determined by the values of $k$, $n_{01}$ and $n_{10}$ through Eq. (7.13). So, instead of $M$ different values of $p$ that coupled to the system in the method afore mentioned, we can recover the full dynamics of the system by only considering the density matrix element associated with the unique non-trivial value of $p$. Thus, using the convenience of Eq. (7.13), the form of the modified density matrix reduces from Eq. (7.6) to,

$$\hat{\mathcal{Q}}[n_{11}, n_{01}, n_{10}; k]. \tag{7.14}$$

Due to this relation, the Algorithm 1 for the Mapper function gets modified to Algorithm 3.

Also due to Eq. (7.13), Algorithm (1) for the Mapper function gets modified. Since we only need to consider one value of $p$ (determined by Eq. (7.13)), given the values of $n_{11}$, $n_{10}$, $n_{01}$ and $k$, we can unravel the loop in line 8 of the algorithm. This also implies that the total dimensions and complexity of the problem reduces

**Algorithm 3** Modified Mapper

**procedure** CREATE-MAP($N$, $M$) ▷ Calculate the index mapping for an $N$ chromophore system with a plasmon state cutoff of size $M$
  $Map \leftarrow$ Initial empty map
  $i = 0$
  **for** $n_{11}$=0 to $N$ **do**
    **for** $n_{01}$=0 to $N - n_{11}$ **do**
      **for** $n_{10}$=0 to $N - n_{01} - n_{11}$ **do**
        **for** $k$=0 to $M - 1$ **do**
          $p = n_{10} - n_{01} + k$
          $Map \leftarrow \{\{n_{11}, n_{01}, n_{10}, k, p\}, i\}$
          $i = i + 1$
        **end for**
      **end for**
    **end for**
  **end for**
  **return** $Map$ ▷ The final Map
**end procedure**

to $O(N^3 \times M)$ through Eq. (7.10) to,

$$C_{reduced} = \frac{N^3 + 6N^2 + 11N + 6}{6} \times M. \tag{7.15}$$

### 7.2.1 Analysis of the complexity reduction

In this section we will analyze the reason for the aforementioned splitting of the modified density matrix space into equivalence classes. We shall see that this property is a direct consequence of the form of the Lindblad contribution to the equations of motion and also, of the use of the RWA. We will investigate the action of the the Lindblad dissipators and the unitary evolution of the interaction Hamiltonian on a general density matrix element, $\hat{\mathcal{Q}}[n_{11}, n_{01}, n_{10}; k, p]$. This will shed light on the elements of the density matrix that is connected to $\hat{\mathcal{Q}}[n_{11}, n_{01}, n_{10}; k, p]$ i.e. the elements that dictate its time evolution through Eqs. (7.8). To begin the analysis, we first introduce the concept of "Excitations". An

excitation refers to either a two-level system in the excited state or a plasmon in a number state greater than **0**. The two-level systems contribute excitations equal to the number of them in state **1**. The plasmon state contributes excitations equal to the number of the state. For a general density matrix element expressed as $\hat{\rho} = |x\rangle \langle y|$, there are two sets of excitations in the ket-vector and the bra-vector. We will denote them by $Ex_x$ and $Ex_y$ respectively. Figure (7.3) expresses how to calculate the number of excitations for a generic density matrix element.

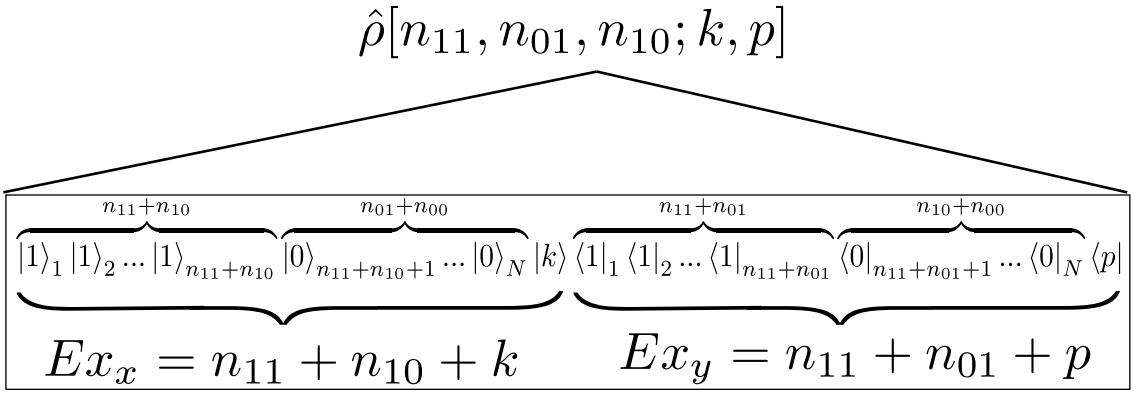


Figure 7.3: The left ($Ex_x$) and right ($Ex_y$) excitation counts of a general density matrix element. Here we only consider a density matrix element where the 1's and 0's are arranged in a specific way. But due to the aforementioned symmetry, any density matrix element can be made equivalent to a density matrix element of this form. The total left and right hand excitation values can be counted off easily using the values $n_{11}$, $n_{01}$, $n_{10}$, $k$ and $p$. All excited chromophores contribute exactly a single excitation while excited plasmons contribute a number equal to the number state the plasmon is in.

### Lindblad Dissipator Contribution

The Lindblad dissipator contribution to the equations of motion is given by Eq. (6.4). The $\hat{A}_j$ in these equations are linear combinations of $\hat{\sigma}_{uv}$ operators or $\hat{a}$, $\hat{a}^\dagger$ operators. Each of these operators contribute three types of terms. For linear combinations of $\hat{\sigma}_{uv}$ operators, the three terms contributed will always be of the form of Table (A1) rows 3-5. This implies that the Lindblad action of the $\hat{\sigma}_{uv}$ op-

erators always result in changing the $Ex_x$ and $Ex_y$ values by the same amount, through their action on the chromophore vectors. Hence they always make connections between $\hat{\mathcal{Q}}$ components whose $Ex_x - Ex_y$ values are the same. For $\hat{a}$ variables (and similarly for $\hat{a}^\dagger$), as seen from rows 10-13 of Table (A1), connections are again formed between between $\hat{\mathcal{Q}}$ components that have the same $Ex_x - Ex_y$ values. This is because they transform the plasmon contributions to the excitations on both sides of the density matrix by the same amount.

**Interaction Hamiltonian Contribution**

In the part of the equations arising from the interaction hamiltonian, it can be seen that the reason for the validity of the relation is due to the energy-conserving nature of the RWA interaction hamiltonian. For any general component of the density matrix, this property translates into a "conservation of excitations" (excitations being either plasmonic or excitonic) among connected density components. i.e. $Ex_x$ and $Ex_y$ are preserved. Rows 14 and 15 of Table (A1) demonstrate this. Both of the two terms of the RWA Hamiltonian contain one exciting operator ($\hat{\sigma}^k_{10}$ or $\hat{a}^\dagger$) and one de-exciting operator ($\hat{\sigma}^k_{01}$ or $\hat{a}$). Since the Interaction Hamiltonian portion originates as a commutation bracket, the Hamiltonian acts on both sides of the density matrix $\hat{\rho} = |x\rangle \langle y|$ separately. So, the total excitation values in both the bra-vector and ket-vector portions remain intact. So, $Ex_x$ and $Ex_y$ are conserved by the interaction hamiltonian within a connected group of density variables.

**Combining the three properties**

From the above analysis it is clear that we have a set of three properties that determine connected density matrix components. The union of density components that satisfy these three properties form the set of all density components

Table A1: **Analysis of the transformations on a general density matrix element $\hat{\rho}$ by operators acting to the left and/or right of the matrix. Notice how earlier rows of the table enable calculating the later rows of the table. For example, it is the composite action of lines 1 and 2 that generates line 3.**

| | Left Operator | Right Operator | Excitations | |
|---|---|---|---|---|
| | | | $Ex_x$ | $Ex_y$ |
| 1 | $\hat{\sigma}^n_{10}$ | - | $\uparrow$ | - |
| 2 | - | $\hat{\sigma}^n_{01}$ | - | $\uparrow$ |
| 3 | $\hat{\sigma}^n_{10}$ | $\hat{\sigma}^n_{01}$ | $\uparrow$ | $\uparrow$ |
| 4 | $\hat{\sigma}^n_{11}$ | - | - | - |
| 5 | - | $\hat{\sigma}^n_{11}$ | - | - |
| 6 | $\hat{a}$ | - | $\downarrow$ | - |
| 7 | $\hat{a}^\dagger$ | - | $\uparrow$ | - |
| 8 | - | $\hat{a}$ | - | $\uparrow$ |
| 9 | - | $\hat{a}^\dagger$ | - | $\downarrow$ |
| 10 | $\hat{a}\hat{a}^\dagger$ | - | - | - |
| 11 | - | $\hat{a}\hat{a}^\dagger$ | - | - |
| 12 | $\hat{a}^\dagger$ | $\hat{a}$ | $\uparrow$ | $\uparrow$ |
| 13 | $\hat{a}$ | $\hat{a}^\dagger$ | $\downarrow$ | $\downarrow$ |
| 14 | $\hat{\sigma}^n_{10}\hat{a}$ | - | - | - |
| 15 | - | $\hat{\sigma}^n_{01}\hat{a}^\dagger$ | - | - |

connected to a component $\hat{\mathcal{Q}}[n_{11}, n_{01}, n_{10}; k, p]$.

- The emitter chromophore based Lindblad terms only forming connections between $\hat{\mathcal{Q}}$ components whose $Ex_x - Ex_y$ values are the same (through changing excitations in the chromophore system). This amounts to connecting components which only differ in $n_{11}$ values.
- The plasmon based Lindblad dissipator terms forming connections between $\hat{\mathcal{Q}}$ components whose $Ex_x - Ex_y$ values are the same (through changing excitations in the plasmon system). These first two properties can be seen as increasing or decreasing the number of "excitations" in the left and right hand side portion of the density matrix by the same value.
- The interaction hamiltonian connecting components that have the same $Ex_x$ and $Ex_y$ values. Note that it is only the interaction Hamiltonian that forms connection between components with different off diagonal values, i.e., components with different $n_{10}$ and $n_{01}$ values.

Combining these three properties, we see that all elements of the density matrix connected to $\hat{\mathcal{P}}[n_{11}, n_{01}, n_{10}; k, p]$ have the same value for the following expression,

$$\begin{aligned} \kappa_2(\hat{\mathcal{Q}}) &= Ex_y - Ex_x \\ &= n_{11} + n_{01} + p - (n_{11} + n_{10} + k) \\ &= (n_{01} - n_{10}) - (p - k). \end{aligned} \tag{7.16}$$

This implies that $\kappa_2$ is a conserved quantity among connected density matrix variables.

### 7.2.2 Extension to 3- and 4-Level Systems

Whilst the 2-Level model is extremely useful, motivated by the historical development of the LASER, higher order systems (3- or 4-Level systems) have the

potential to be practically more useful and theoretically more robust in spasing setups. In [59], 3-Level systems coupled to two external electromagnetic fields were shown to exhibit improved spasing characteristics. We also use a 3-Level gain chromophores for the spaser we model in Chapter 9. Anticipating the usefulness of such systems, we present the theoretical consequences of our method for 3- and 4-Level systems. Following the exact arguments as given above, it can be shown that 3- or 4-level systems with incoherent pumping can be reduced to have linear size complexity in the plasmon-number-state size. Consider a 3-level system with levels indexed by **0**, **1** and **2**. Level **0** acts as the ground state and the spasing transition occurs between levels **0** and **1**. The chromophores are incoherently pumped up to level **2** after which they undergo a fast transition to level **1**. Excitation conservation implies,

$$\begin{aligned}\kappa_3 &= Ex_y - Ex_x \\ &= (2 \times (n_{22} + n_{12} + n_{02}) + n_{21} + n_{11} + n_{01} + p) \\ &\quad - (2 \times (n_{22} + n_{21} + n_{20}) + n_{11} + n_{10} + n_{12} + k) \\ &= 2 \times n_{02} + n_{12} + n_{01} + p - (2 \times n_{20} + n_{21} + n_{10} + k).\end{aligned} \tag{7.17}$$

Next, we apply the same reasoning we did to derive the excitation conservation based equations, to level **2** of the chromophores. Since level **2** is not one of the spasing levels, all excitations to level **2** on both the left and right hand side of the density matrix should be conserved within the chromophore system itself. Hence, we can write the following conserved quantity,

$$\kappa_3^{L2} = 2 \times n_{02} + n_{12} - (2 \times n_{20} + n_{12}). \tag{7.18}$$

Using Eq. (7.18) in Eq. (7.17), we get the following conserved quantity,

$$\begin{aligned}\kappa_3 &= n_{01} + p - (n_{10} + k) \\ &= (n_{01} - n_{10}) - (k - p).\end{aligned} \tag{7.19}$$

This equation implies a total dimensional size of $O(N^4 \times M)$ of the problem. For a 4-level system with ground state at level **0** and spasing occurring between levels **1** and **2**, the conservation of excitations results in the following conserved quantity,

$$\begin{aligned}\kappa_4 &= Ex_y - Ex_x \\ &= 3 \times n_{03} + 2 \times (n_{13} + n_{02}) + n_{12} + n_{23} + n_{01} + p \\ &\quad - (3 \times n_{30} + 2 \times (n_{31} + n_{20}) + n_{21} + n_{32} + n_{10} + k).\end{aligned} \tag{7.20}$$

Since levels **3** and **0** do not partake directly in the spasing actions, we can derive the following conserved quantities as well,

$$\kappa_3^{L3} = 3 \times n_{03} + 2 \times n_{13} + n_{23} - (3 \times n_{30} + 2 \times n_{31} + n_{32}), \tag{7.21}$$

$$\kappa_3^{L0} = 3 \times n_{03} + 2 \times n_{02} + n_{01} - (3 \times n_{30} + 2 \times n_{20} + n_{10}), \tag{7.22}$$

Since both levels **1** and **2** are separate from the spasing levels, the quantities $n_{30}$ and $n_{03}$ are not modified through the interaction Hamiltonian portion of the equations. Since they are not of the form $n_{uu}$, neither do they get affected through the Lindblad dissipator terms. Hence they are both conserved quantities. Using this information together with Eqs. (7.20), (7.21) and (7.22), we arrive at the following conserved quantity which results in a dimensional size of $O(N^5 \times M)$ for the 4 level emitter chromophore problem,

$$\begin{aligned}\kappa_4 &= n_{12} + p - (n_{21} + k) \\ &= (n_{12} - n_{21}) - (k - p).\end{aligned} \tag{7.23}$$

### 7.2.3 Improvement of solver efficiency

The dimensions of various incoherently pumped, coupled chromophore-plasmon system solution schemes are given in Table (A2). As can be seen, the formalism we have presented in this chapter results in a significant reduction in the dimensions of the problem. This results in both the reduction of the space complexity as well as the time complexity. The table also demonstrates the magnitude of complexity reduction our formalism offers without compromising the exactness of the numerical program. We have also carried out numerical simulations to

Table A2: **Dimensions of the Density Matrix $\rho$ in various formalisms. The Actual Dimension values are calculated for $N = 100$ and $M = 80$, under the system parameters as used in [56].**

| Formalism | Dimensions | Actual Dimensions |
|---|---|---|
| Full Density Matrix | $O(4^N \times M^2)$ | $\approxeq 10^{64}$ |
| Richter *et al.* [52] | $O(N^3 \times M^2)$ | $\approxeq 10^{10}$ |
| Our method | $O(N^3 \times M)$ | $\approxeq 10^{8}$ |

test the time efficiency of our method as compared to using the complete modified density matrix along with the Eqs. (7.8). The simulations used the Order 4/5 Cash-Karp Adaptive Runge-Kutta scheme as the solution method. We calculated the evolution of incoherently pumped chromophore-plasmon systems with chromophore numbers ranging from 10-100. We have used the same parameters and decay/dephasing rates reported in [56]. We performed the same calculations using two methods.

The first method, which we will refer to as the "full" method, uses the full $O(N^3 \times M^2)$ dimensions as described in [52]. The second method, which we will refer to as the "reduced" method utilises the dimensionality reduction arising from the relations derived in this chapter. We performed the simulations on a setup consisting of two Intel Xeon E5-2690v4 (Broadwell) 2.6GHz processors with 28 cores in total. We utilised shared memory parallelism on this system to extract the best performance out of our numerical algorithms. The numerical algorithms

for both methods were coded in C++ using efficient data structures for performing the calculations needed. More details on the elements of our quantum solver and the techniques used, are summarised in Appendix E.

We compared the performance by measuring the execution speed of the algorithms. We observed that the total convergence time of both methods depended heavily on the pumping rate and other system parameters. But the average time of a single adaptive Runge-Kutta step remained constant with respect to varying system parameters, given that $N$ and $M$ remained constant. Hence we use the average time of a single Runge-Kutta time step as a measure of the time performance of the algorithm. The results are shown in Fig. (7.4). We also indicate the system sizes comparison of both methods in the same graph. We also measured the space performance of the algorithm by tracking the amount of memory usage of each of the simulations. While memory usage is heavily implementation dependent, we have endeavoured to keep the memory usage patterns within both of the algorithm implementations similar and hence the memory usage of both methods at the same system configuration will be a indicator of relative performance of the algorithms. Figure (7.5) display these results.

Both sets of time and space efficiency measurements indicate that the dimensionality reduction attained with our direct formalism has significant impact on the performance of the algorithm. We have been able to show that, with the reduced method, we can handle systems more than twice the size as with the full method, with the same amount of time and memory resources.

The Eqs. (7.13), (7.19) and (7.23) as derived in the previous section effectively couples just one $k$ dimension to each $p$ dimension and hence results in the reduction in size from $M^2$ to $M$. Due to the existence of this exact relation, programming such a reduction of dimensions into a numerical code becomes quite straightforward. The density matrix can be built from the ground up using this relation without the need to follow a connectivity analysis scheme (effectively a

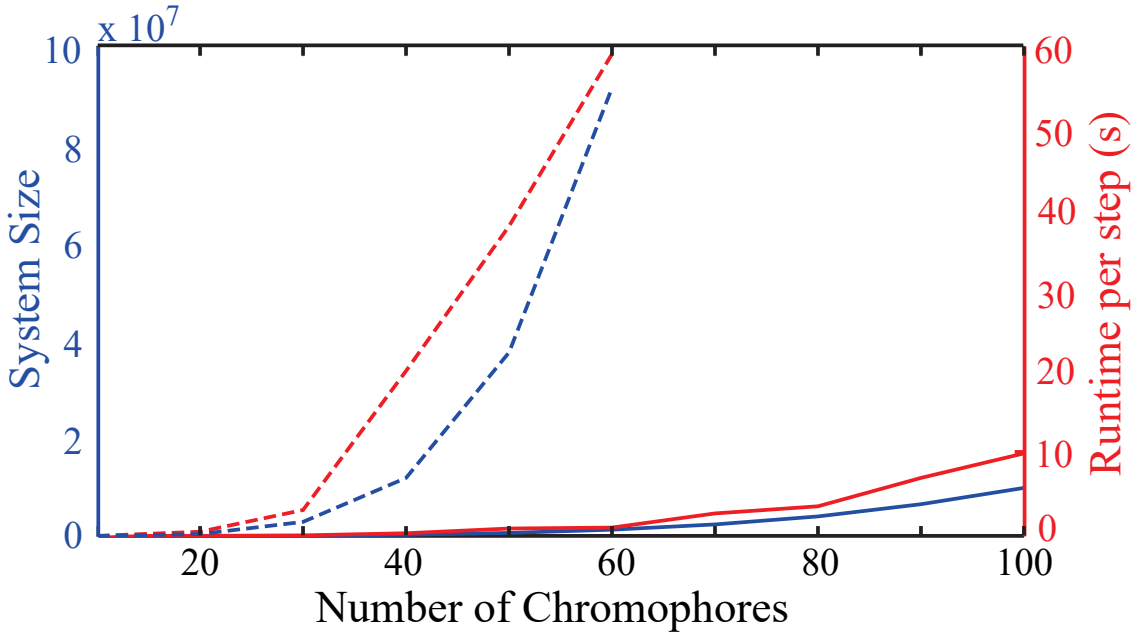


Figure 7.4: The figure shows the total system size and time performance of a single Runge-Kutta step for the two methods described in the text. The full method data are displayed in dashed line format while the reduced method is displayed in solid lines. The red curves display the timings while the blue curves display system sizes for both methods. The full method takes a greater length of time per step as expected and the increase in time seem to increase exponentially. The Both algorithms were coded in C++ with efficient use of shared memory parallelism. The simulations were run on a single computing node consisting of 28 computing cores.

breadth-first search) between connected variables in order to squeeze the dimensions down only after building the full quantum density matrix. This approach considerably reduces the space requirements of the numerical calculation. Additionally, Eq. (7.15) together with Eq. (7.11a) implies a total $O(N^4)$ size for identical two-level chromophore based, incoherently pumped, spaser setups.

The reduction in dimensions of the plasmon space size can be graphically seen in Fig. (7.6). In the full method, the plasmon subspace consists of all the variables represented by the dots in the matrix. But in the reduced method, only one diagonal of the whole matrix, generally represented by the green bounding box, is non-zero which enables us to discard the rest of the matrix entirely.

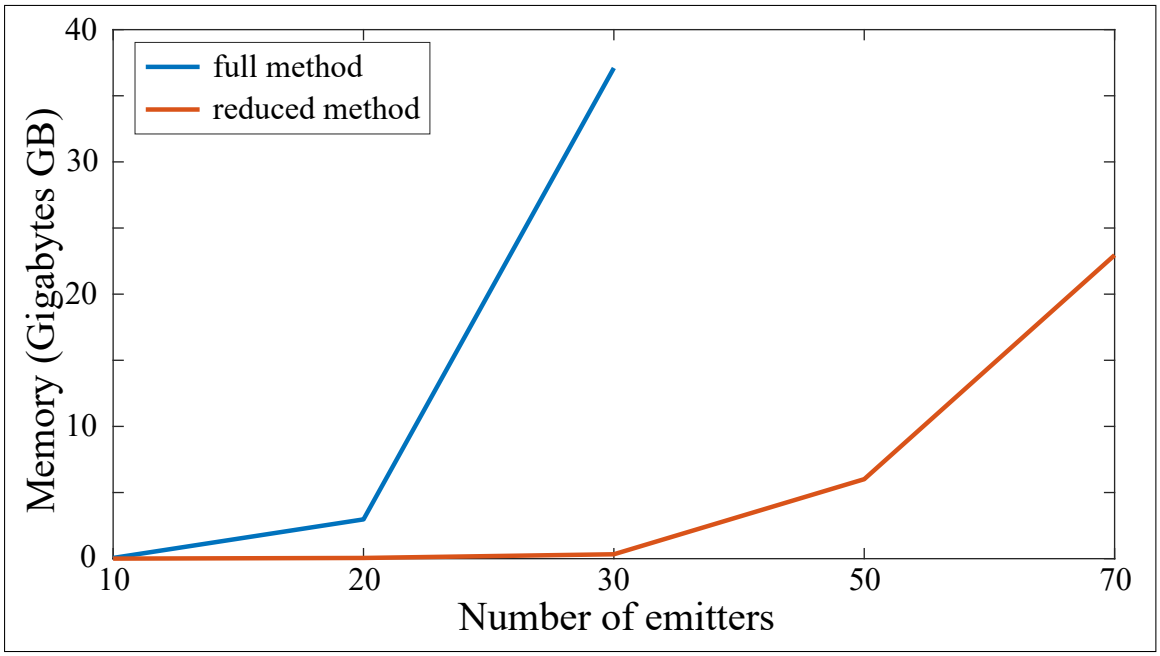


Figure 7.5: The figure shows the memory performance of the two methods described in the text. The reduced method vastly outperforms the full method which consumes orders of magnitudes less memory. Both algorithms were coded in C++ with efficient use of shared memory parallelism. The simulations were run on a single computing node consisting of 28 computing cores.

In the reduction in the dimensions of the problem as implemented in [52, 60], a general element of the plasmon subspace of the density matrix can be expressed in the form $|k\rangle \langle p|$ where $k, p = \{0, 1, ....M - 1\}$ . Here $M$ is the number of plasmon number states considered in the numerical model.The total number of such density matrix elements is $M^2$. This gives rise to the $M^2$ dimensions of the cavity subspace. But [52, 60] proposes a method of only using the diagonal elements, i.e. elements with $k = p$, and a specific number of off-diagonal elements closest to the diagonal, in the numerical solution and checking for convergence of the calculation to assess whether enough off diagonals have been included. The only density matrix elements considered non-zero in this scheme are framed with the blue bounding box in Fig. (7.6), where the plasmon subspace of the density matrix is depicted by a matrix. The diagonal elements are always included in

the analysis and the bounding box is expanded along the red arrows until convergence is reached. The reasoning behind this approach of bracketing density matrix elements near the diagonal whilst discarding the rest outside is that as we go away from the diagonals in the directions depicted by the two red arrows, the values of the densities decrease and hence most of them can be excluded from the analysis with only a very minute sacrifice in precision. This could typically result in an $O(M)$ sized plasmon subspace density matrix. But the relations we

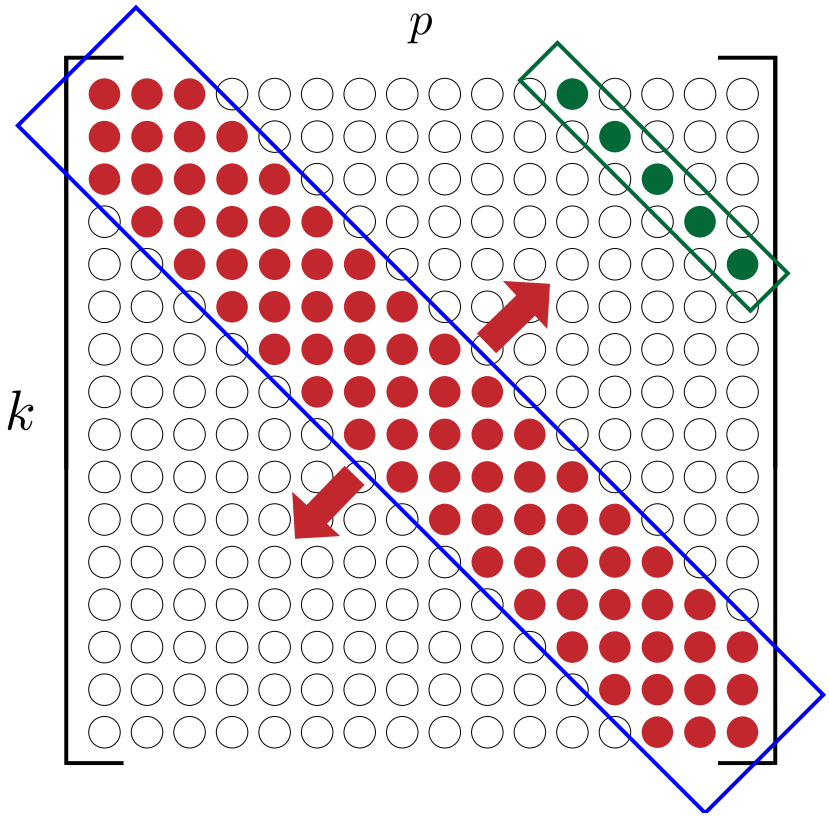


Figure 7.6: The matrix form of the plasmon-subspace of the density matrix $|k\rangle\langle p|$. According to the results of this chapter, there is no guarantee that the main-diagonal will be non-zero. It is exactly one of the main, super or sub-diagonals that will be non-zero (shown within the green bounding box).

have derived imply that the only non-zero non-diagonal elements of the cavity subspace density matrix form either a main, sub or super-diagonal similar to the

green-box-bounded super-diagonal depicted in Fig. (7.6). So a scheme that only considers the diagonal and a few super/sub-diagonals of the cavity space density matrix instead of the full dimensions may not be appropriate since such a scheme may very well leave out the only non-zero contribution to the equations in favour of a few contributions that are guaranteed to remain identically zero during the evolution of the system. The fact that the number of diagonals included in the calculation need to be adjusted until the density values converge also implies that multiple simulations may need to be run serially to attain the steady state. Our method also bypasses this inconvenience.

We also note that the dimensionality reduction as we have derived here applies to any coupled emitter-cavity setup modelled using an RWA-approximated interaction hamiltonian, Lindblad term based dissipators and incoherent pumping. A similar analysis can be applied to the case of coherent pumping but that only results in the reduction of the size of the problem by a factor of 2 for 2-level gain elements.

## 7.3 Summary and conclusion

In this chapter, we have presented the theoretical details of the quantum solver we built to solve the coupled nanoresonator-emitter model. We applied it in the context of spasing showed that it achieves orders of magnitude higher efficiency in terms of time and space utilisation. We have also described the efficient algorithmic techniques and data structures used in constructing the solver. Further details are available in Appendices C, D and E. This solver has already been used to analyse the behaviour of spasing systems previously intractable in order to compare with the classical analyses [61]. These analyses have shown vital differences in the quantum treatment. It can also be used to validate approximate numerical schemes.

We note here that the solver as we have described here have certain limitations. Primarily, the solver is only useful when the emitters are identical. In addition to that, the interactions between emitters and the bleaching of emitters are not included. The inclusion of these effects would vastly improve the impact of the current solver. While these extensions are by no means not trivial, we envisage future versions of our solver being useful not only in analysing spasing setups, but also countless other photonic setups where the exact same paradigm of a cavity coupled to emitters is used.

The results of this chapter were published in the Journal of the Optical Society of America B [61].

# Chapter 8

# Quantization of plasmonic nanoparticles

In our everyday life, quantum mechanical effects remain hidden and almost none of our basic interactions with the world are affected by quantum mechanics; or so we think. Almost every advance of modern technology is made on the back of quantum mechanics and the peculiarities it bring. From electronics, to computers, chemistry and pharmacology, materials science and some of the modern transportation systems are heavily rooted in quantum mechanics. However, we do not observe these effects first hand. This is due to the fact that quantum effects only come to light at very small length scales or very high energy scales.

Contrary to us, nanoparticles feel the effects of quantum mechanics as a rule of usual existence. This is due to the size of the space they live in. The world according to nanoparticles is a probability driven world full of Schrödinger cat paradoxes. Hence, the proper analysis of these particles require a fully quantum mechanical picture of it. In this chapter, we will go through the basic mechanism for "quantizing" the plasmonic response of nanoparticles.

It has been known for a while that plasmons behave similar to bosons and hence follow Bose-Einstein statistics. The quantization procedure for such particles is already well established and only require technical difficulties to be overcome in performing the calculations. In general, these procedures would require computer-based numerical calculations. But, in an effort to grasp the actual effect

of various parameters, we will strive for an analytical approach here. To keep the analysis analytical we will make use of the so-called dipole approximation which describes the plasmon as a pure dipole. In the context of working with purely linear external excitations this approach remains valid. This is due to the fact that linear excitations only excite dipole active bright modes and these modes may be effectively described as dipoles. We will use the results we already derived in Chapter 4 for this.

The first section of the chapter will present the quantization procedure for the transverse dimer bright mode. Next, we will derive the same quantization for the longitudinal dimer configuration. Finally we will derive the coupling strengths of the quantized dimers to gain media chromophores.

## 8.1 Quantization of the plasmonic bright mode of a transverse dimer

We start with the result we derived in Chapter 4 for the total electrical energy of a transverse dimer bright mode,

$$W = \frac{\beta^2}{8\pi} \sin^2(\omega_0 t) \mathcal{W}(D), \tag{8.1}$$

where,

$$\mathcal{W}(D) = \int |\mathbf{G}(\mathbf{r};\mathbf{r}_1) + \mathbf{G}(\mathbf{r};\mathbf{r}_1)|^2 \,\mathrm{Re}\left\{ \frac{d}{d\omega}(\omega\epsilon)\bigg|_{\omega=\omega_0} \right\} d^3\mathbf{r}, \tag{8.2}$$

The integral is over infinite space. The extra derivative factor in the expression precisely accounts for the energy in dispersive media [24]. Next we make the following definitions for normalisation factor $N$ and normalised amplitude $A$,

$$N = \sqrt{\frac{8\pi\hbar\omega_0}{\mathcal{W}(D)}}. \tag{8.3}$$

$$B = \frac{\beta}{N}. \tag{8.4}$$

This enables us to write the total potential energy stored in the electric field as,

$$W = \hbar\omega_0 B^2 \sin^2(\omega_0 t). \tag{8.5}$$

This expresses the potential energy of the electric field in a form reminiscent of electric field energy of an electromagnetic field. If we were quantizing a general electromagnetic field, the next step would be to compute the energy stored in the magnetic field and form the complete Hamiltonian. The magnetic and electric components of the electromagnetic field would then act as conjugate operator variables of a harmonic oscillator system. But in the near-field of the dimer setup, the magnetic field is close to zero. A significant portion of the energy is actually stored in the kinetic motion of the electron cloud composing the plasmon [62]. However, estimating this proportion of energy stored outside of the electric field is not a trivial task.

We handle this difficulty by considering the fact that, disregarding the dissipations, the total energy stored in the system should be constant and hence the energy stored in the electric field and the energy in the kinetic portions of the system including the current flows within each sphere must add up to a constant value [63]. For total energy to be conserved at all times $t$, the kinetic energy term must be of the form [22],

$$K = \hbar\omega_0 B^2 \cos^2(\omega_0 t). \tag{8.6}$$

This implies that our system is identical to a harmonic oscillator system with potential energy and kinetic energy being continually converted to each other in a periodic manner. Introducing the variable $A(t) = B \sin \omega_0 t$ , the total Hamilto-

nian thus takes the form,

$$H = \frac{\hbar}{\omega_0}(\omega_0{}^2 A^2 + \dot{A}^2). \tag{8.7}$$

This Hamiltonian takes the exact form of the quantum harmonic oscillator with conjugate variables $A$ and $2\hbar A/\omega$. Making the identification $\hat{x} = A$ and $\hat{p} = 2\hbar A/\omega$, we can transform to the position and momentum picture of the simple harmonic oscillator. $\hat{x}$ and $\hat{p}$ obey the usual commutation relations,

$$[\hat{x}, \hat{p}] = i\hbar. \tag{8.8}$$

Then we can define the bosonic annihilation operator as,

$$\hat{a} = \hat{x} + \frac{i}{2\hbar}\hat{p}. \tag{8.9}$$

Using this, the Hamiltonian can finally be put in the form,

$$H = \hbar\omega_0(\hat{a}^\dagger\hat{a} + \frac{1}{2}). \tag{8.10}$$

Using the newly defined creation and annihilation operators, we can cast the electric field in the from,

$$\mathbf{E}_{\text{dimer}}(\mathbf{r}) = \frac{1}{2}N[\mathbf{G}(\mathbf{r};\mathbf{r}_1) + \mathbf{G}(\mathbf{r};\mathbf{r}_2)](\hat{a}^\dagger + \hat{a}). \tag{8.11}$$

Next we turn towards the question of the coupling between the dimer plasmon system and a dipole degree of freedom of a nearby chromophore. The interaction energy of a dipole interacting with an electric field $\hat{\mathbf{E}}$, can be given by $H_{\text{int}} = -\hat{\mathbf{P}} \cdot \hat{\mathbf{E}}$, where $\hat{\mathbf{P}}$ is the dipole moment operator of the chromophore. Assuming the dipole to originate from a two-level electronic transition, we could express the dipole moment operator as $\hat{\mathbf{P}} = \mu(\sigma_{10} + \sigma_{01})\hat{\mathbf{z}}$, where $\mu$ is the transition dipole moment and $\sigma_{10}$, $\sigma_{01}$ are the raising and lowering operations for the

electronic transition. Using (8.11) and applying the rotating wave approximation to consider only the energy conserving terms bring us to the final expression for the interaction Hamiltonian,

$$H_{\text{int}}(\mathbf{r}) = \hbar g(\mathbf{r})(\sigma_{10}\hat{a} + \hat{a}^{\dagger}\sigma_{01}), \tag{8.12}$$

where the coupling constant $g(\mathbf{r})$ can be expressed as,

$$g(\mathbf{r}) = -\frac{1}{2}\mu N[\mathbf{G}(\mathbf{r};\mathbf{r}_1) + \mathbf{G}(\mathbf{r};\mathbf{r}_1)], \tag{8.13}$$

## 8.2 Quantization of the plasmonic bright mode of a longitudinal dimer

Now we turn to the question of longitudinal dimers. The equations and formulas applying to the longitudinal dimers remain approximately equal to the transverse. Using Eq. (4.21), we can express the total electrical energy in the longitudinal dimer mode as,

$$W = \frac{\beta^2}{8\pi}\sin^2(\omega_0 t)\mathcal{W}(D). \tag{8.14}$$

Here, all quantities have the same meaning as in the transverse case except for the redefinition of the center coordinates of the nanospheres. Using the same arguments as for the transverse setup, this expression can be used to quantize the longitudinal dimer and finally we find the coupling constant $g(\mathbf{r})$ as,

$$g(\mathbf{r}) = -\frac{1}{2}\mu N[\mathbf{G}(\mathbf{r};\mathbf{r}_1) + \mathbf{G}(\mathbf{r};\mathbf{r}_2)]. \tag{8.15}$$

Using these forms derived for the quantized field operators for the transverse and longitudinal bright modes, it is straightforward to derive the corresponding quantization procedure and coupling strength values for a singlet nanosphere as

well.

# Chapter 9
# Nanosphere dimer based spaser

In the previous chapters, we have completed the analysis of the plasmons on nanospherical dimers and performed the quantization as a precursor to the quantum analysis. In this chapter we will perform full calculations needed to analyse the dimer spasing system as a coupled gain-resonator system. We use the open Dicke model as described in Chapter 6.

## 9.1 The gain medium

We model the gain medium as a collection of three-level chromophores. This allows one of the electronic transitions to couple to the pumping field and the other transition to couple to the dimer plasmons, giving us control over the two transitions independently. The structure of the electronic levels is depicted in Fig. 9.1. The pumping electric field is coupled to the $0-2$ transition while the $0-1$ transition is coupled to the plasmons.

We assume that a rapid non-radiative decay takes place from level 2 to level 1. We also assume all the dipole moments of the chromophores to be aligned in the $\hat{\mathbf{z}}$ direction and the dipole transitions to be in resonance with the corresponding plasmons. For a chromophore indexed by $n$, we define the quantum state by a ket vector $|u:n\rangle$, with $u=0,1,2$ depending on the level. The transition operator from level $v$ to $u$ can then be defines as, $\sigma_{uv}^{n}=|u:n\rangle\langle v:n|$. The $0-2$ electronic

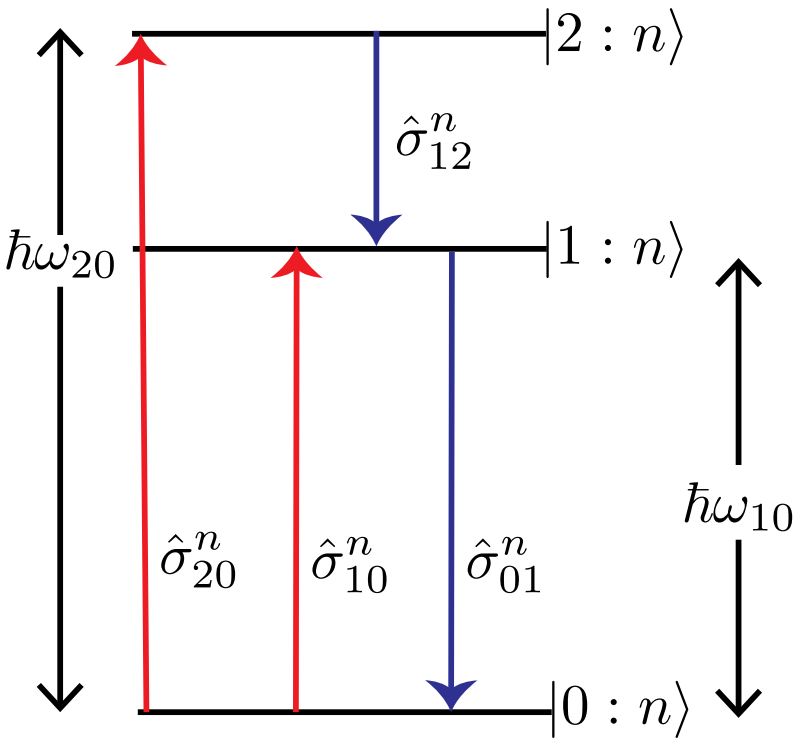


Figure 9.1: The energy level diagram for a single three-level gain medium chromophore is shown. The operators shown perform the transitions between the levels as indicated by the arrows.

transition has a dipole moment of 16 Debye and the $0-1$ transition has moment 14.4 Debye in all results presented in this chapter. We assign a non-radiative decay rate of 0.1 eV between levels 3 and 2, following similar theoretical analyses done on three-level spasing models [57]. We assume all other decay channels within the gain chromophores to be negligibly weak.

## 9.2 Dimer-gain coupling strength

The coupling strength between the plasmon setup and the gain medium dictates much of the characteristics of spasing including the threshold. Next we investigate the strength of the coupling between the dimer setups and a gain chro-

mophore placed at different locations. The separate configurations we study are elucidated in the inset of Fig. 9.3.

For a singlet setup with a chromophore placed along the sphere axis in the direction of the dipole moment (commonly referred to as the longitudinal placement of the chromophore), the coupling strength variation can be given by [22],

$$g_{\text{sing}}^{\text{long}} = N_{\text{sing}} g_s(\mathbf{r}), \tag{9.1}$$

where $g_s(\mathbf{r}) = \left|\frac{R}{r-\frac{D}{2}}\right|^3$. The same chromophore placed along a sphere axis perpendicular to the dipole moment would have a coupling strength,

$$g_{\text{sing}}^{\text{tr}} = \frac{1}{2} N_{\text{sing}} g_s(\mathbf{r}), \tag{9.2}$$

For dimer setups, we place the origin at the midpoint of the axis joining the spheres. Using Eq. (8.13), coupling strength for a chromophore placed along the dimer axis for a transverse dimer setup can thus be calculated to be,

$$g_{\text{tr}} = \frac{1}{2} N_{\text{tr}} g_d(\mathbf{r}), \tag{9.3}$$

with $g_d(\mathbf{r}) = \left(\left|\frac{R}{r+\frac{D}{2}}\right|^3 + \left|\frac{R}{r-\frac{D}{2}}\right|^3\right)$, while Eq. (8.15) gives,

$$g_{\text{long}} = N_{long} g_d(\mathbf{r}), \tag{9.4}$$

for a longitudinal dimer.

All these quantities are plotted in Fig. 9.2 for silver spheres of radii 10 nm and 20 nm and separation values $D = 25$ nm, 40 nm and $D = 45$ nm, 60 nm respectively. As can be seen, when the spheres in a dimer are close enough(low $D$ values), the field confinement in between the two spheres is great enough to support coupling strengths exceeding the singlet setup. We also observe that the larger spherical nanoparticles support the greater enhancement of the coupling

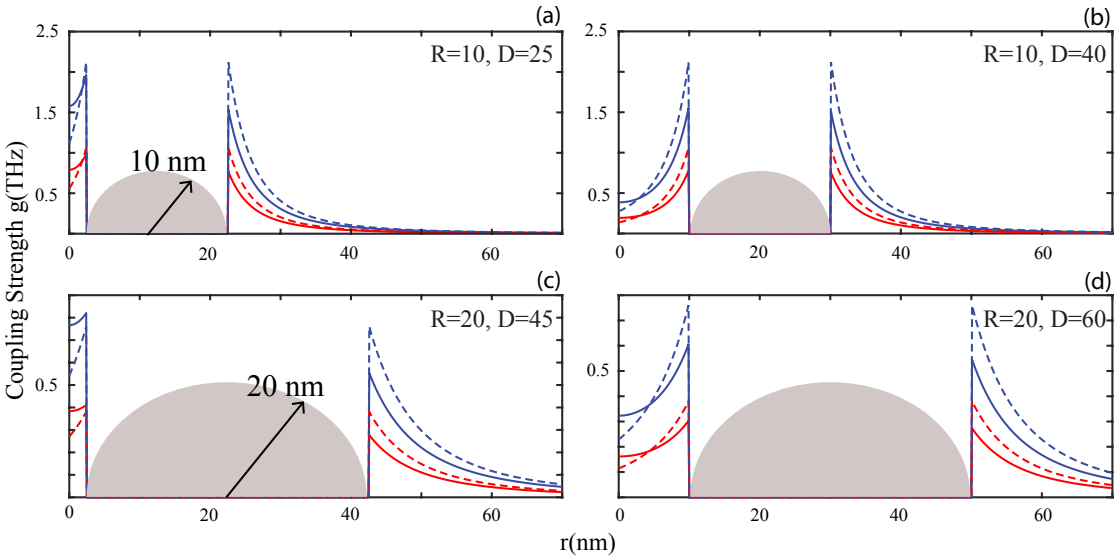


Figure 9.2: Coupling strengths for a chromophore with 1 Debye moment along the z-axis, placed at different distances from singlet and dimer plasmon setups. Solid lines plot the two dimer setups, transverse(red) and longitudinal(blue) with the chromophore placed on the dimer axis. The dashed lines represent the singlet with the chromophore placed along the metal nanoparticle dipole moment(blue) and placed perpendicular to the dipole moment(red).

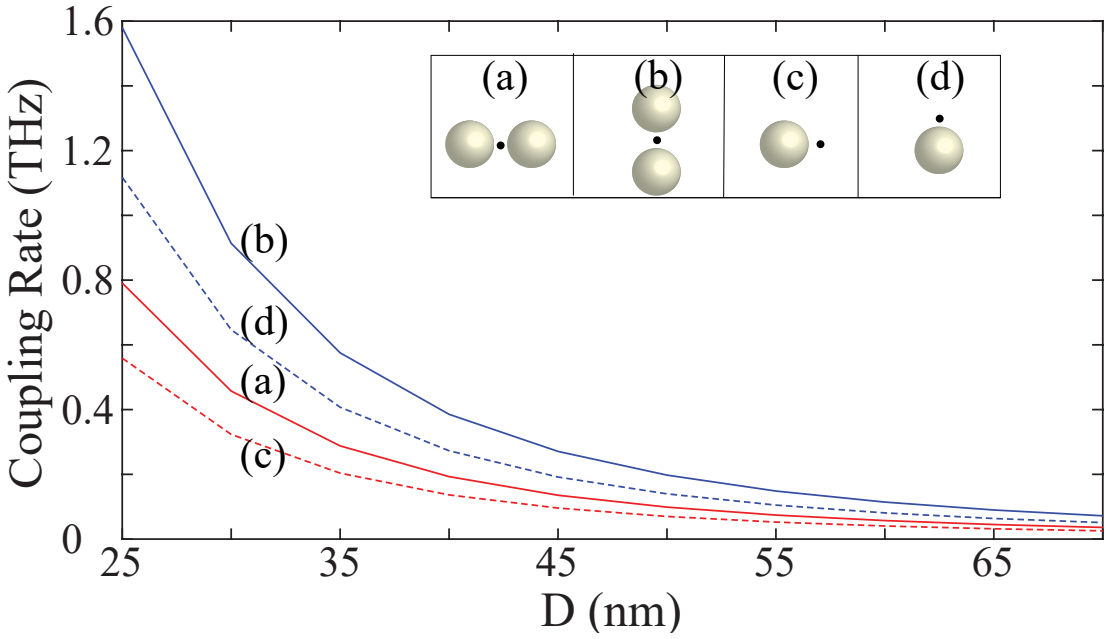


Figure 9.3: The coupling strength(g) of the dimer longitudinal and transverse setup to a chromophore placed at the midpoint of the dimer axis(solid lines) for various dimer separation values(D). The radius of the nanospheres are set at $R = 10\,\text{nm}$. The singleton coupling strengths for chromophores placed at the same distance are shown by the dashed lines. The inset depicts the placement of the gain chromophore(black circle) in each case.

relative to the singlet setup while the smaller nanomparticles have higher absolute values of the coupling strength. Figure 9.2 also indicates that the longitudinal dimer setup has the better coupling characteristics and has the potential to form the basis for better spasing setups.

Next we study the impact of the separation $D$ on the coupling. Figure 9.3 plots the variation of the coupling strength of a chromophore of moment 1 Debye placed at the midpoint of a dimer setup consisting of metal nanospheres of radius $R = 10\,\text{nm}$. As can be seen, the longitudinal setup again has greater coupling strength at the mid-point as compared to the transverse setup. For reference, we have also included the coupling constants for a chromophore placed at the same distance away from a singlet setup. As we discovered earlier, the longitudinal chromophore placement in the singlet configuration performs much

better as compared to the transverse placement, but not as well as the longitudinal dimer configuration. This again demonstrates the benefits of the dimer setup as compared to the singlet as far as spasing is concerned.

## 9.3 Dissipation in the spasing setup

Next we turn to the question of calculating the plasmon decay rate $\gamma_{pl}$. The decay is due to two main causes: the ohmic dissipations within the metal $\gamma_0$, and the radiative dissipation caused by radiation into the far field $\gamma_r$. The ohmic dissipation is a property of the metal and can be extracted from the permittivity of the metal. In this work, we use the dissipative rate as predicted by the Drude dielectric model [64] for silver. The radiative dissipations on the other hand depends on the electric fields in the system and hence needs to calculated.

We first focus on the singlet setup. The radiative decay rate can be calculated using the radial component of the Poynting vector in the far field. The time averaged power radiated per unit solid angle per unit time can be given by [21],

$$\begin{aligned}\frac{d\langle W\rangle}{d\Omega} &= \frac{c}{8\pi}\,\mathrm{Re}[r^2\mathbf{n}\cdot(\mathbf{E}\times\mathbf{H})]\\ &= \frac{c}{8\pi}k^4|(\mathbf{n}\times\mathbf{P})\times\mathbf{n}|^2, \qquad (9.5)\\ &= \frac{c}{8\pi}k^4|\mathbf{P}|^2\sin^2(\theta), \qquad (9.6)\end{aligned}$$

where $\mathbf{n}$ is the normal vector in the direction of the solid angle $d\Omega$. This can be integrated to give the total power radiated per unit time to be,

$$\frac{d\langle W\rangle}{dt} = \frac{ck^4}{3}|\mathbf{P}|^2. \qquad (9.7)$$

Finally, the dissipation rate for a singlet can be calculated as,

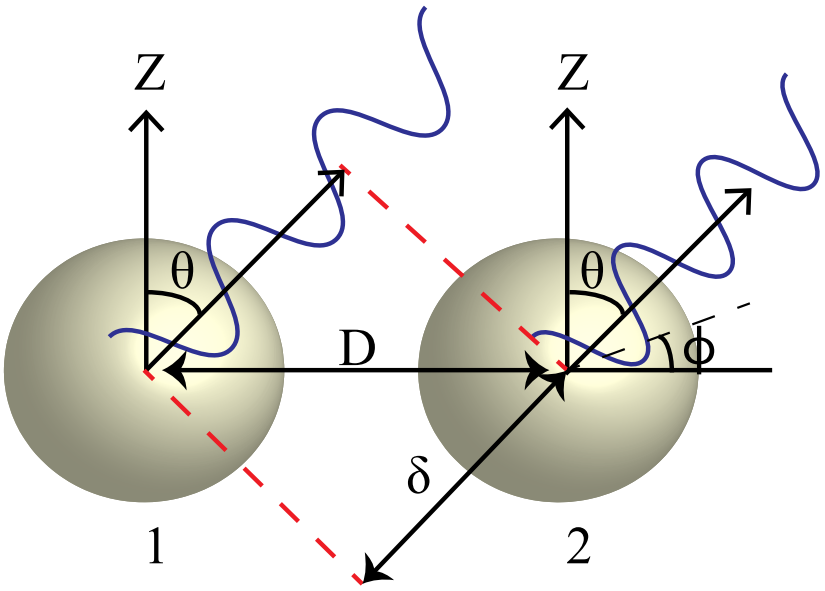


Figure 9.4: The phase lag between the electromagnetic radiation emitted by the two sphere dipoles in a general polar angle direction $\theta$ and azimuthal angle $\phi$.

$$\gamma_r = \frac{1}{\langle W \rangle} \frac{d\langle W \rangle}{dt}. \tag{9.8}$$

Here, $\langle W \rangle$ is the time averaged power of the electrical field.

For a transverse dimer the above derivation should be modified due to the existence of contributions from both spheres. Sufficiently far from the dimer system, for $D \ll |\mathbf{r}|$, the field lines from both spheres appear parallel and hence we could consider the vector sum of the two dipole moments. i.e. we can substitute $\mathbf{P}$ in Eq. (9.8) with $2\frac{\alpha R^3 E_0}{1+\frac{\alpha R^3}{D^3}}$. But this approach would not be correct since it does not take into account the interferences generated by the two dipoles. To account for this, we follow a slightly different approach and consider the phase differences between the radiation waves emitted by the two spheres at a specific polar angle $\theta$, and azimuthal angle $\phi$.

As seen in Fig. 9.4, the radiation emitted in the direction $(\theta, \phi)$ by sphere number 2 is exactly $\delta$ distance ahead of the radiation emitted by sphere 1, where

$\delta$ is given by,

$$\delta = D\sin(\theta)\cos(\phi). \tag{9.9}$$

This corresponds to a phase difference $\phi_{tr}$ of,

$$\phi_{\text{tr}} = k\delta = \frac{2\pi D\sin(\theta)\cos(\phi)}{\lambda}. \tag{9.10}$$

Hence the radiated electric field of sphere 2 in a certain radial direction with respect to sphere 1 can be written as,

$$\mathbf{E}_2^{\text{rad}}(\theta,\phi) = \mathbf{E}_1^{\text{rad}}(\theta,\phi)e^{i\phi_{\text{tr}}}. \tag{9.11}$$

The total radiated electric field can thus be written,

$$\mathbf{E}^{\text{rad}}(\theta,\phi) \quad = \mathbf{E}_1^{\text{rad}}(\theta,\phi)(1+e^{i\phi_{\text{tr}}}). \tag{9.12}$$

This radiation, in the far field, can be interpreted as emanating from a dipole placed at the position of dipole 1, but with a dipole moment scaled by the factor $(1+e^{i\phi_{\text{tr}}})$. Using this interpretation, we can write the effective dipole moment in the direction $(\theta,\phi)$ as,

$$P^{\text{eff}}(\theta,\phi) = P(1+e^{i\phi_{\text{tr}}}). \tag{9.13}$$

Going back to Eq. (9.5), the rate of radiative power dissipation per solid angle can be modified to,

$$\frac{d\langle W\rangle}{d\Omega} = \frac{c}{8\pi}k^4|\mathbf{P}|^2\sin^2(\theta)\left|(1+e^{i\phi_{\text{tr}}})\right|^2, \tag{9.14}$$

Noting that,

$$|1+e^{i\phi_{\rm tr}}|^2 = (1+e^{i\phi_{\rm tr}})(1+e^{-i\phi_{\rm tr}}) \tag{9.15}$$

$$= 2[1+\cos(\phi_{\rm tr})] \tag{9.16}$$

$$= 4\cos^2\left(\frac{\phi_{\rm tr}}{2}\right), \tag{9.17}$$

we can write Eq. (9.14) as,

$$\frac{d\langle W\rangle}{d\Omega} = \frac{c}{2\pi}k^4|\mathbf{P}|^2\sin^2(\theta)\cos^2\left(\frac{\pi D\sin(\theta)\cos(\phi)}{\lambda}\right). \tag{9.18}$$

Integrating this over all solid angles gives us the final value for the energy radiated per unit time. Then we can use Eq. (9.8) to calculate the radiative dissipation rate.

We can follow the exact same argument to calculate the radiative dissipation rate for the longitudinal setup. The phase difference turns out to be, $kD\cos(\theta)$ and the expression for the energy radiated per unit solid angle per unit time is,

$$\frac{d\langle W\rangle}{d\Omega} = \frac{c}{2\pi}k^4|\mathbf{P}|^2\sin^2(\theta)\cos^2\left(\frac{\pi D\cos(\theta)}{\lambda}\right). \tag{9.19}$$

Using Eqs. (8.1), (9.18), (8.14), (9.19) we can present the radiative dissipation rate for dimer setups with resonance wavelength $\lambda$ as,

$$\gamma_r = \frac{32\pi^4 cR^6}{\mathcal{W}(D)}\frac{\mathcal{I}(D/\lambda)}{\lambda^4}, \tag{9.20}$$

where, $\mathcal{I}(D/\lambda) = \int\int 4\sin^3(\theta)\cos^2(\frac{\pi D\sin(\theta)\cos(\phi)}{\lambda})d\theta d\phi$ for transverse configurations and $\mathcal{I}(D/\lambda) = \int\int 4\sin^3(\theta)\cos^2(\frac{\pi D\cos(\theta)}{\lambda})d\theta d\phi$ for longitudinal configurations with $\mathcal{W}(D)$ given by Eq. (8.2). The $\mathcal{I}$ terms can be associated with the effects of interference between the two dipoles and $\mathcal{W}$ term is proportional to the total average power of the dimer system. We plot $\mathcal{W}$ against dimer sep-

aration for 10 nm and 20 nm dimer setups in Fig. 9.5(c-d). As can be seen, the proportional changes in power is extremely small and hence can be considered negligible. To understand why this is justified, consider the electrical energy of an isolated sphere $W_s$. For spheres placed close by in transverse configuration, the interaction energy $W_I \propto W_s R^3/D^3$ [21]. Hence the proportional change in $\mathcal{W}(D)$ between two spheres placed at infinity and spheres placed at distance $D$ can be given by, $\Delta\mathcal{W} = R^3/2D^3$. As we saw earlier the proportional change in $\lambda^{-4}$, $\Delta\lambda^{-4} = (1 + R^3/D^3)^2 - 1$. Since $2R^3/D^3 + R^6/D^6 \gg R^3/2D^3$, we conclude that the change in $\mathcal{W}(D)$ is negligible. A similar argument can be followed for the longitudinal case.

The key factors governing the dissipation rate hence is the interference $\mathcal{I}$ and the resonance wavelength $\lambda$.

We plot the change in radiative dissipation rate for transverse and longitudinal dimers with dimer separation in Fig. 9.5(a-b). We first notice that the radiative dissipation rates for the sizes of nanospheres we consider, dominate the ohmic losses. At the smallest dimer gap we study(5 nm), the transverse dimer shows higher radiative dissipation as compared to the longitudinal.

However, more interestingly, the interference and resonance frequency shifts manifest interesting properties as spacing between the nanospheres is increased. In general, the transverse setups display a steady decline for the range of spacings we study. The longitudinal setup on the other hand goes through a maximum and starts declining. As can be seen for both 10 nm and 20 nm dimer setups, in the extremely close configurations(small $D$), the transverse dimer radiates energy at a higher rate as compared to the longitudinal dimer. But at a certain separation, the transverse setup dips steeply below the longitudinal curve and continues downwards. This implies the reduction of the transverse dimer radiative dissipation at larger separations. This can be understood in terms of the two key terms in Eq. (9.20). The $\mathcal{I}(D/\lambda)$ term diminishes for larger values of $D$ while the $\lambda^{-4}$ term

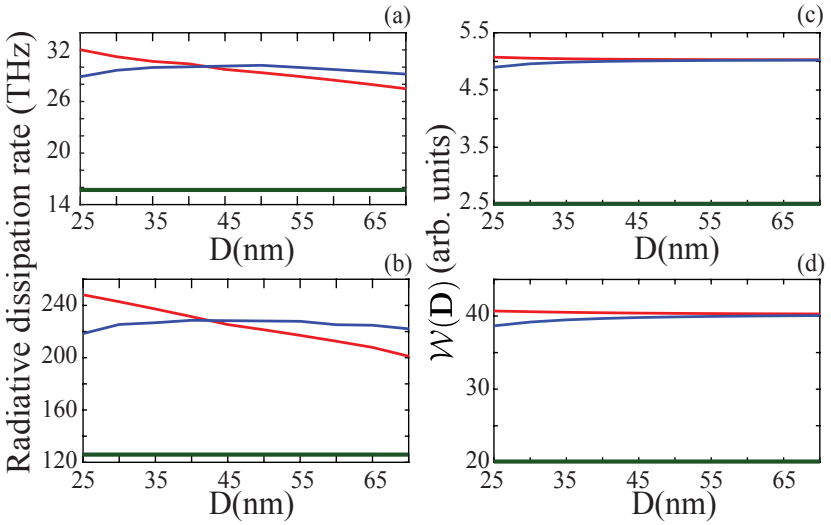


Figure 9.5: The radiative dissipation rates(a-b) and mean power (c-d) for transverse(red) and longitudinal(blue) dimer setups composed on nanospheres of radii 10 nm and 20 nm at various dimer separations. (a) and (c) display the data for the 20 nm nanosphere setups while (b) and (d) represent data for the 20 nm setups. In all graphs, the solid green line indicates the level for a singlet with the same radius.

also diminishes due to the red shift of the resonance frequency for larger separations. These two effects combine to account for the reduction in transverse dimer dissipation rate.

For the longitudinal dimer, while $\mathcal{I}(D/\lambda)$ diminishes for larger separations, the resonance frequency experiences a blue shift, causing the $\lambda^{-4}$ term to actually dominate for smaller separations causing the peaked behaviour we observe. For larger separations however, the interference term dominates causing reduction of dissipation. Hence, heuristically, we can say that the radiation interference and resonance frequency shifts cooperatively cause reduction in radiative dissipation in transverse dimers, while for longitudinal dimers, those two effects act in opposition resulting in a peaked behaviour for intermediate dimer separations before interference dominates to bring down total dissipations.

We note that a similar analysis was performed in [65] but the interference effects were neglected resulting in a radiative dissipation that only depended on

hybridized resonance wavelength $\lambda$. [66] also performs a similar analysis by calculating the linewidth of scattered spectra of dimers. The results there agree with our predictions qualitatively but the analysis therein is performed approximately which results in a prediction of $\lambda^{-2}$ dependence of the radiative dissipation. We attribute this discrepancy to the fact that only the kinetic energy of oscillating charges were considered in [66], whereas detailed energy balance in plasmonic systems require the consideration Electrical Energy = Kinetic Energy + Magnetic Energy [62].

## 9.4 Solving the open Dicke model

Now we turn to question of actually solving the open Dicke model equations we derived earlier for spasing systems. To consider how to solve this system of equations, let us first consider the size of a wave-vector that describes the system. Assuming the plasmon modes may be truncated at a highest possible occupation number value of $M$, there are $M+1$ different possible values of the plasmon occupation number. For $N$ chromophores each with 3 energy levels, there are $3^N$ possible configurations. This implies that a wave-vector describing the system will have a size equal to $3^N(M+1)$. The density matrix in turn will have dimensions $6^N(M+1)^2$. This is a computationally impossible bound to handle and solve exactly. As shown in Chapter 7, if the assumptions of identical chromophores and incoherent pumping of chromophores are valid, the problem could be cast into a problem of size $O(N^4M)$ and numerically exactly solved. But in many realistic setups, these assumptions may be too restrictive. Another practically useful and faster method of approximately solving the system involves using the Reduced Density Matrix(RDM) approach [56]. It obtains a closed set of equations for the steady state density matrix of the system using some reasonable approximations. The main equation solved is the reduced density matrix for plasmon

number states $\rho_{\mu,\nu}$, in terms of coupled individual chromophore density matrices $\rho^n_{u\mu,v\nu}$, where $n$ identifies the particular chromophore and $u, v = 0, 1, 2$ denote the energy level of the electron of that chromophore.

$$\begin{aligned}\frac{\partial}{\partial t}\rho_{\mu\nu} \quad &= -i(\mu-\nu)\omega_{pl}\rho_{\mu\nu} - \gamma_{pl}\frac{\mu+\nu}{2}\rho_{\mu\nu} \\ &+\gamma_{pl}\sqrt{(\mu+1)(\nu+1)}\rho_{\mu+1\nu+1} \\ &-\sum_{n=1}^{N} ig_n(\sqrt{\mu}\rho^n_{1\mu-1,0\nu} - \sqrt{\nu}\rho^n_{0\mu,1\nu-1}) \\ &+\sum_{n=1}^{N} ig_n(\sqrt{\nu+1}\rho^n_{1\mu,0\nu+1} - \sqrt{\mu+1}\rho^n_{0\mu+1,1\nu}).\end{aligned} \tag{9.21}$$

This method has shown to provide approximately useful values for the density matrix equations for a three level gain medium in a wide range of parameters with just $O(NM)$ time complexity [57]. In this chapter, we use the RDM approach due to the convenience and also its ability to handle heterogeneous gain media. We refer the reader to [57] for a complete treatment on the method and the associated derivation of equations.

## 9.5 Bright mode spasing curves

Next we approach the question of modelling the action of a spaser, the plasmonic component of which is formed by a dimer setup composed of 10 nm radius silver nanospheres. As previous results demonstrated, the main characteristics of a dimer setup is the the higher coupling rate to gain chromophores in the dimer gap and the higher radiative dissipations. We present results that demonstrate the effects of these two key differences between the two dimer configurations as well as between the dimer setups and the singlet setup.

Non-linear quantum effects come into play when the dimer gap is extremely

small due to to the quantum nature of the electrons, non-local screening effects and tunnelling of electrons [67]. In addition to that, as we observed earlier in the hybridized resonance frequency calculations, the dipole approximation fails to account for the resonance frequency shifts in a dimer for extremely small separations. Hence in all our simulations, we maintain a gap of at least 5 nm between the metal spheres.

The main setup we use for the simulation and characterisation of the spasing properties are shown in the inset of Fig. 9.6 as an example for the transverse spasing setup. We study the singlet setup, transverse dimer setup, and the longitudinal dimer setup, each of which is surrounded by a cuboid shaped discrete gain medium distribution and we maintain a gain chromophore number density of $0.125\,\mathrm{cm}^{-3}$. For gain chromophores with molecular sizes spanning the Angstrom range, this value is realistic and it also allows us to make the sparsity assumption for the gain medium. We take the lengths of the gain medium extent in the three directions to be $L_x$, $L_y$ and $L_z$ with the chromophores stationed at the grid points. Note that the gain medium cuboid is always centered at the midpoint of the dimer axis. We assume that the chromophore 0-1 transition is exactly in resonance with the plasmons in each of our simulations with the $2^{nd}$ electronic level lying a further 0.1 eV higher from level 1 of the chromophores. This value allows the $1-2$ electronic transition to be decoupled from the higher order multipoles for the plasmons we consider and also is commensurate with values used in similar theoretical investigations done on 3 level spasing models [57].

The two main metrics we use to analyse spasing behaviour is the mean plasmon number which quantifies the strength of the spasing and the second order coherence of the plasmon distribution, which quantifies the quality of the spasing as a measure of coherence of the plasmons created. Solving for the plasmon density matrix grants us access to the full probability distribution of plasmon excitation and hence the calculation of both quantities are quite straightforward.

The mean plasmon number, $N_{pl} = \langle \hat{a}^\dagger \hat{a} \rangle$, can be calculated using the reduced density matrix elements solutions from Eq. (9.21) as,

$$N_{pl} = \sum_{\mu} \mu \rho_{\mu\mu}. \tag{9.22}$$

A higher mean plasmon number is indicative of higher intensity spasing. Similarly, the second order coherence, $g^2_{pl} = \frac{\langle \hat{a}^\dagger \hat{a}^\dagger \hat{a} \hat{a} \rangle}{\langle \hat{a}^\dagger \hat{a} \rangle^2}$, can be calculated as,

$$g^2_{pl} = \frac{\sum_{\mu} \mu(\mu - 1)\rho_{\mu\mu}}{N^2_{pl}}. \tag{9.23}$$

A second order coherence value of 1 signifies a perfectly coherent stimulated emission output while it reaches values of 2 for random noise. Hence ideally, values closer to 1 are preferred in spasing.

We start off by comparing three spasing curves for spasers made of chromophore setups with $L_x = L_y = L_z = 50\,\text{nm}$ for 10 nm silver spheres in Fig. 9.6. The three curves are: longitudinal setup with $D = 25\,\text{nm}$, transverse setup with $D = 25\,\text{nm}$ and a singlet setup. We also plot the second order coherence values in the same graphs.

As we can clearly see, the singlet setup outperforms the dimer setups both in terms of quantity(mean plasmon number) and quality(second order coherence) at almost all simulated pumping power values. We also observe that in general, the longitudinal spasing setup has higher intensity spasing output as compared to the transverse setup. However, in terms of second order coherence, the transverse configuration seems to consistently have the more ideally coherent output.

Looking closer, we see that for small pumping values, the singlet performs best, followed by the transverse dimer and the longitudinal dimer respectively. At this early stage, the spasing output seems to increase linearly with the pump-

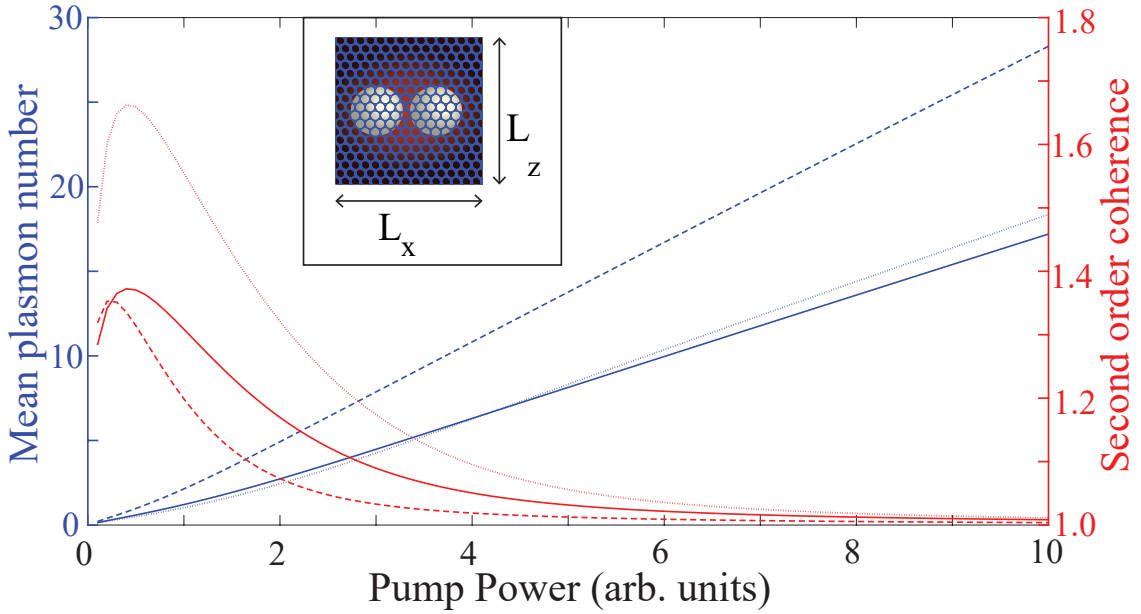


Figure 9.6: The mean plasmon numbers(blue) and the second order coherence values(red) for dimer and singlet configurations consisting of 10 nm nanospheres. The transverse dimer curves are denoted by the solid lines, the longitudinal dimers by the dotted lines and the singlet configurations by the dashed lines. The dimer separation is maintained at 5 nm. Inset shows the distribution of chromophores for a transverse dimer setup. The chromophore distribution extents along the x- and z-directions are shown as $L_x$ and $L_z$.

ing power while, more interestingly, the second order coherence increases as well. This increase in second order coherence is indicative of the fact that actual stimulated emission has not set in as of yet in the system and that the emission in that range corresponds only to amplified spontaneous emission. This also demonstrates that the linear increase in spasing output by itself is not a reliable indicator of spasing.

However, at a certain pumping value we observe a sudden decrease of second order coherence for all three setups. This occurs at an electric field strength of $E_0 = 4 \times 10^4\,\mathrm{Vm}^{-1}$ for the dimer setups and at $E_0 = 2 \times 10^4\,\mathrm{Vm}^{-1}$ for the singlet. This decline of second order coherence is soon followed by a visible increase in the slope of the spasing curves. This visible "kink" in the spasing curve is much less pronounced as compared to conventional lasing systems. However, this may be considered a clear sign of the threshold of spasing systems due to the simultaneous decrease in the value of the second order coherence. A previous quantum study on the nature of spasing concluded that the spaser showed thresholdless behaviour due to the lack of a clear spasing transition from spontaneous and stimulated emission [52]. This difference is due to our assumption that the $1 - 0$ transition of the gain elements having negligible decay rates. For larger decay rates, the amplified spontaneous emission is suppressed by the chromophore decays causing less amplification along with less buildup of incoherent plasmonic population. Hence, for sufficiently low gain decay rates, spasing systems do display threshold behaviour. A similar behaviour of the second order coherence was predicted for lasing in the bad cavity limit using a Fokker-Planck approach [68]. Functionally, spasing systems and bad cavity lasers are similar due to the very high plasmonic dissipations in spasing setups.

Beyond threshold, singlet curve shows the steeper gradient while the longitudinal dimer curve, lagging behind the transverse dimer curve up until this point, increases with a higher gradient than the transverse setup. Concurrently, we see

the second order coherence values of all three setups decrease rapidly to reach values close to 1 for high pump powers.

## 9.6 Dark mode spasing

In addition to the bright modes, as we mentioned earlier, the dark modes may also be quantized by considering an appropriately polarised light source. Using that fact, and performing the same quantization procedures as for the bright modes, we can arrive at an exactly similar quantum model for bright modes. In Fig. 9.7, we present the spasing curves for all four of the fundamental modes of a nanospherical dimer consisting of sphere with radius $R10$ nm and separation $D = 25$ nm. The chromophores are distributed symmetrically around the dimer in a cubic shape with side length 100 nm.

As we can see, the bright modes perform much worse than the singlet while dark modes perform much better than the singlet. This is mainly due to the high radiative dissipation present in bright modes as compared to the singlet and the dimer dark modes.

We also present the second order coherence curves for the same setup in Fig. 9.8. As we expect from the spasing curves, the dark modes of the dimer setup perform the best as compared to both the singlet and bright mode setups.

## 9.7 Dimer separation dependent effects in spasing

Next we study the spasing output variation with dimer separation. Figure 9.9(a) displays the mean plasmon number of the spasing setups for transverse(red) and longitudinal(blue) configurations composed of 10 nm nanospheres pumped with an electric field $E_0 = 1 \times 10^5\,\mathrm{Vm}^{-1}$ with a cubic gain medium distribution of size 100 nm on each side. In general, we observe that the transverse setup exhibits

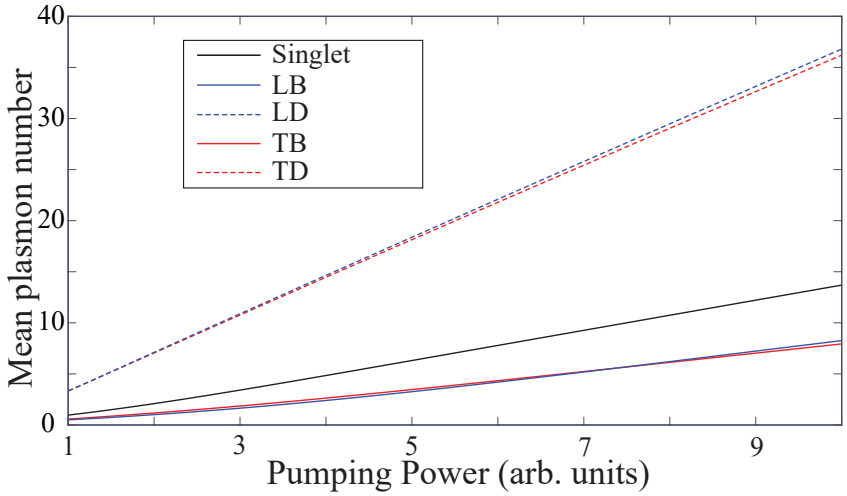


Figure 9.7: The mean plasmon numbers of dimer and singlet configurations consisting of 10 nm nanospheres. The various dimer modes are indicated in the inset The dimer separation is maintained at 25 nm. The chromophore distribution is cubic with side lengths of 100 nm each.

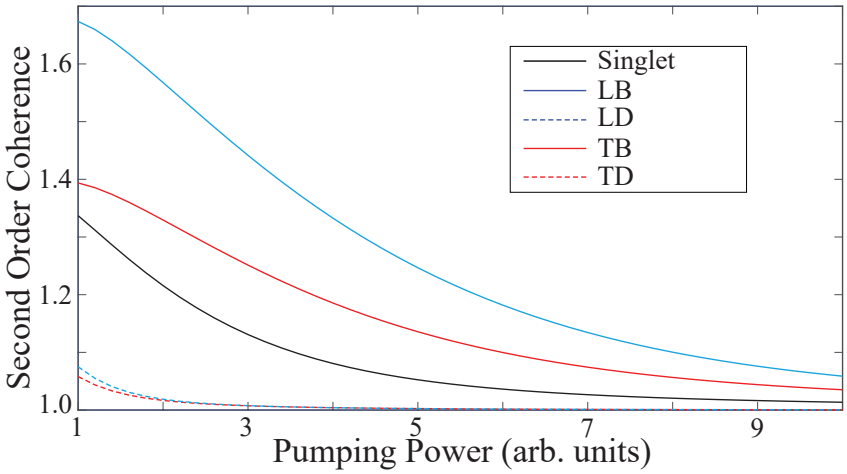


Figure 9.8: The second order coherence values of dimer and singlet configurations consisting of 10 nm nanospheres. The chromophore distribution is cubic with side lengths of 100 nm each.

higher intensity spasing. As the separation is increased, the transverse dimer shows a generally increasing behaviour. The longitudinal dimer on the other hand experiences a reduction in emissions before recovering for larger separation values. This can be understood by 3 key factors affecting the spasing output as separation is increased:

1. The change in radiative dissipation rate;
2. The reduction in field confinement in the dimer hotspot(electric field leakage);
3. The increase in the proportion of chromophores in the dimer hotspot;

For a transverse dimer, as discussed previously, interference effects and resonance frequency red shift causes the radiative dissipations to decrease with increasing dimer separation. This acts to increase spaser output. However, the increased dimer gap also allows a higher proportion of the gain medium to access the dimer hotspot and strongly couple to the plasmons generated. But this comes with the downside of the decrease in intensity of the hotspot due to leakage. Hence factors 2 and 3 act in opposition to each other. Figure 9.9 suggests that in general, the radiative dissipation rate and the increasing chromophores within the dimer gap dominates causing a general increase in spasing output for transverse dimers. However, for larger separations, the spaser output plateaus, showing the influence of the electric field leakage.

For longitudinal dimers, the radiative dissipation shows a peaked behaviour before reducing for large separations. Similar to the transverse case, the reduction in field confinement and increase in the proportion of gain chromophores strongly coupled to the plasmons act in opposition to one another when spaser output intensity is concerned. However, as shown in Fig. 9.9, the longitudinal dimer output first decreases and then recovers to increase with increasing separation. The lowest spaser output almost perfectly coincides with the radiative dissipation minimum(see Fig. 9.5), which indicates that radiative dissipation is

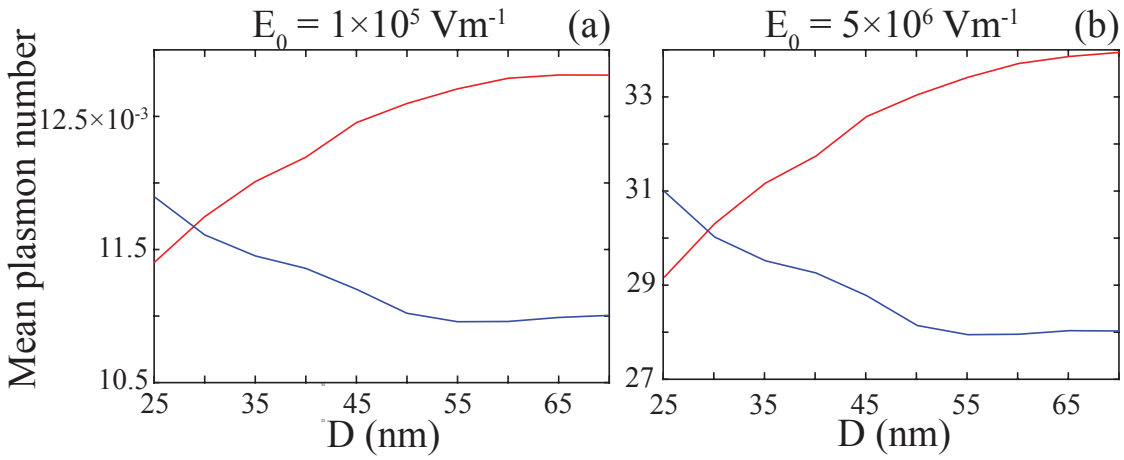


Figure 9.9: Variation of the mean plasmon number with the separation between dimers for transverse(red) and longitudinal(blue) configurations. The nanosphere radius is $R = 10\,\text{nm}$ and the gain medium distribution has $L_x = L_y = L_z = 100\,\text{nm}$.

the dominant force determining the spasing output for smaller separations. However, for larger separations, the longitudinal setup shows a plateauing behaviour similar to the transverse setup due to the reduction in electric field confinement.

We perform the same analysis for a dimer spaser setup pumped with a field $E_0 = 5 \times 10^6\,\text{Vm}^{-1}$ in Fig. 9.9(b). We again clearly see a similar pattern of behaviour for transverse and longitudinal configurations.

## 9.8 Spasing variation with gain medium extent

Finally, we present the variation of the spaser output with the size of the gain medium. Figure 9.10 displays the variation of the spaser emission intensity and second order coherence value for the two dimer configurations as well as the singlet configuration with the length of a cubic gain medium. The displayed size is the length of one side of the cube. We observe the dramatic increase in the spasing output intensity as well as the decrease of the second order coherence value to 1. It has been observed in other studies done on spasing in three-level gain media

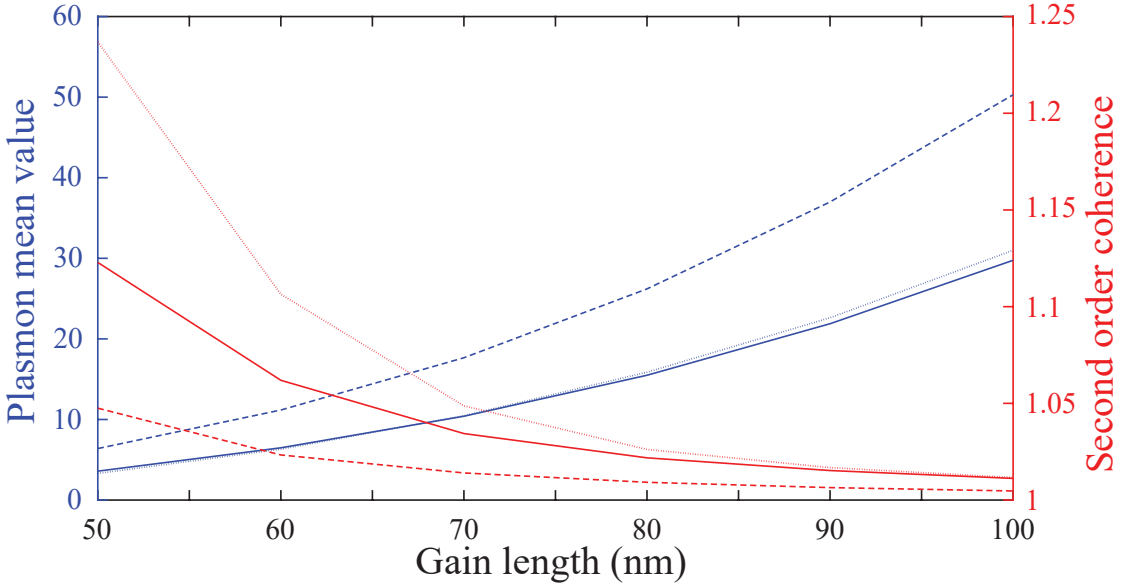


Figure 9.10: The variation of the mean plasmon number(blue) and second order coherence(red) for transverse dimer(solid line), longitudinal dimer(dotted line) and singlet(dashed line) setups with the size of the surrounding cubic gain medium. The shown size indicates the length of one side of the gain medium cube. The nanospheres are of 10 nm radius and the separation $D = 5\,\text{nm}$ for the dimer setups. The pump field is held constant at $E_0 = 5 \times 10^6\ \text{Vm}^{-1}$.

that the spasing output tends to follow a linear variation with the number of gain chromophores given that the gain chromophores are identical [57]. In our case, we observe that the spasing output displays a sub-cubic dependence on the gain medium length. This is due to the fact that while the number of chromophores grows as the cube of the length, the chromophores are not identical and the couplings of chromophores from further away is much weaker compared to the ones closer to the plasmon.

We also note that for smaller gain medium distributions the transverse dimer spaser output is higher than that of the longitudinal. But as the size of the gain medium and the number of chromophores increase, the longitudinal dimer overtakes the transverse.

## 9.9 Summary and conclusion

This chapter has presented our key findings on the spasing characteristics of a nanopshere dimer based spaser. We have shown that for low pumping, large separation scenarios, the transverse dimer outperforms a longitudinal dimer and vice versa for all other cases. We have shown that this behaviour is due exactly to the interference pattern of the radiation emitted by the two nanospheres. We have also shown that the spasing characteristics indicate the importance of the second order coherence of the generated plasmons as an indicator of the spasing threshold. These results suggest that, in hybrid structures, the spasing characteristics intimately depend upon the exact configuration of singlet elements. Longitudinal and transverse placements show vastly different behaviours. Our results also suggest that in lattice like setups, the optimum spasing is achieved by placing singlets as close as possible in the longitudinal direction while placing them at a certain optimal distance in the transverse direction. This has serious implications for designers of such spasing setups. We belive that our results will be the start-

ing point for investigations of lattice spasing structures with dimensions tuned to achieve maximal spasing.

The results of this chapter were published in Physical Review B [69].

# Chapter 10
# Contributions and Future work

## 10.1 Summary of Contributions

**Research objective 1 - Studying the response of hybridized plasmonic systems coupled to gain media**

In this stage, we semi-analytically modelled the quantized dimer-multiple emitter system and numerically solved the resulting master equation to high accuracy. We modelled the dissipations within the system using the Lindblad formalism and found that the interference of the radiative dissipations in the dimers cause the output to portray interesting behaviour based on the exact positioning of the nanospheres with respect to the pumping field. We also showed that the second order coherence of the dimer based spaser displays a very peculiar signature near spasing threshold that had been predicted earlier for lasing systems.

This stage was successfully completed and the results were published in the journal *Physical Review B*.

**Research objective 2 - Studying the plasmonic response of nano-tori**

At the completion of this stage, we managed to complete the analysis of the plasmonic modes on a nano-torus. We studied the poloidal spectrum of the torus

in the Neumann-Poincare(NP) operator formalism and showed that the poloidal modes may be described as resulting from the splitting of the transverse cylindrical modes on an infinite cylinder by the symmetry breaking that happens when the cylinder is folded. We showed that the spectrum actually consists of two branches, one with positive NP eigenvalues and another with negative eigenvalues, that converge to the cylindrical modes at low aspect ratio. We also show that it is the positive eigenvalue branch that actually dominates in terms of dipole response and that the negative eigenvalue branches become important at high aspect ratios when the symmetry breaking is significant enough for them to be distinguuished from each other.

This stage was successfully completed and the results have been accepted for publication at *Physical Review B*.

**Research objective 3 - Development of an exact and efficient quantum solver for the coupled resonator and identical emitter model**

In this stage, we built a quantum solver capable of exactly solving the coupled nanoresonator-emitter problem exactly. We leveraged a symmetry that we discovered within the master equation to significantly reduce the dimensionality of the problem. Employing the C++ programming language, we managed to create the solver using optimal data structures and efficient parallelised schemes for fastest possible convergence. The solver easily solved problems involving over 100 emitter chromophores within 24 hours, whereas the fastest available implementations previously were scarcely able to solve problems involving 10 chromophores within 24 hours. We also managed verify the validity of certain alternative approximations schemes such as the Reduced Density Matrix(RDM) approach and the Fokker-Planck equation approach by comparing the results to ones as predicted by our exact solver.

Upon successful completion of this stage, the findings were communicated in the journal *Journal of the Optical Society of America B*.

## 10.2 Suggestions for Future Work

The work presented in this thesis can be usefully extended in a number of theoretical and experimental pathways. We have outlined a few suggested directions below.

**Investigating spasing in multiple lattice-like plasmon structures**

We have completed the analysis of spasing in nanoparticle dimers. In our work, we found that based upon the longitudinal or transverse arrangement of the dimer setup, the spasing output has two completely different behaviours. Based upon this, we have postulated that lattice-like plasmon hybridized structures will display behaviour which would be a hybrid of the two. The investigation of this question would be of great value and interest. The modelling method we have used may be easily extended to precisely analyse this case.

**Investigating multi-mode spasing in hybrid structures**

While we have presented the full quantum treatment of the dimer spaser, there exist structures that require a description comprising of multiple interacting plasmonic modes. This description is beyond the simple dipole approximation and needs to be treated with other numerical methods such as the Quasi-normal mode(QNM) [70] approach or the Generalised Normal Mode approach(GENOME) [71]. These descriptions would implicitly contain the interaction effects of the plasmonic modes resulting in a coherent model for treating muti-modal spasers.

**Coupled nanoresonator-emitter model solver for interacting emitters**

One of the key interactions we have not considered in our quantum solver is the interaction effects between emitter chromophores. These effects may cause significant changes in the expected spasing output and may also result in slight frequency shifts. Including these effects in the quantum solver amounts to adding in extra terms to account for the energy exchange between chromophores. An analysis on the symmetry structures of the terms added would need to be also performed before adding the modifications into the model. This would result is far more accurate and useful results.

**Approximate solver for coupled nanoresonator-emitter model**

One of the possible extensions that would be highly impactful is modifying the current solver to be able to handle non-identical emitters within a certain approximation. This would allow the solver to be used for accurate modelling of the quantum systems without sacrificing efficiency. Ideally, we expect the model to be polynomial in it's complexity in contrast to the exponential complexity of the exact problem. This would require an analysis of the perturbations caused by non-identical emitters and correcting them using interaction terms.

**Poloidal modes in azimuthally symmetric structures**

As we have shown, the torus. as resulting from the rotation of the circular disk around an external fixed point results in a splitting of the modes of the disk into a dual infinity of modes. We suggest the extension of that work to cover other structures as generated by rotating different smooth 2D shapes. A first such example would be an ellipse and the structure generated by rotating the ellipse to generate a "squashed torus" shape. We would expect there to a splitting of the modes, and the resulting spectrum would be of great interest. The analysis would

also lay the groundwork for a discussion on the behaviour of plasmonic modes in 3-dimensional objects made by revolving a 2-dimensional shape around a fixed axis.

**Plasmonic modes on a Möbius strip and multiple twist structures.**

Another fascinating problem we are currently left with is the structure of the plasmonic modes on a Möbius strip structure. This structure is the same as a torsu, except for the breaking of the symmetry in the toroidal direction. We expect the structure to have an interesting modal structure that would be useful in applications. While the Möbius strip is composed of just one twist, higher number of twists produce structures that have discrete symmetry in the toroidal direction. The investigation of such structures would also be extremely valuable to our understanding of plasmonic modes on various structures.

# Appendix A
# The solution of the Laplace equation

## A.1 Laplace equation in Spherical coordinates

The Laplace equation can be given as,

$$\nabla^2 V = 0. \tag{A.1}$$

Let's assume the function $V$ is separable as,

$$V = R(r)\Theta(\theta)\Phi(\phi). \tag{A.2}$$

The Laplace operator can be expressed in spherical coordinates as,

$$\nabla^2 = \frac{1}{r^2}\frac{\partial}{\partial r}\left(r^2\frac{\partial}{\partial r}\right) + \frac{1}{r^2\sin^2(\theta)}\frac{\partial^2}{\partial\phi^2} + \frac{1}{r^2\sin(\theta)}\frac{\partial}{\partial\theta}\left(\sin(\theta)\frac{\partial}{\partial\theta}\right). \tag{A.3}$$

Plugging Eq. A.2 into this gives us,

$$\nabla^2 V = \left(\frac{r^2\sin^2(\theta)}{R}\frac{d^2R}{dr^2} + \frac{2r\sin^2(\theta)}{R}\frac{dR}{dr}\right) + \left(\frac{1}{\Phi}\frac{d^2\Phi}{d\phi^2}\right) + \left(\frac{\sin(2\theta)}{2\Theta}\frac{d\Theta}{d\theta} + \frac{\sin^2(\theta)}{\Theta}\frac{d^2\Theta}{d\theta^2}\right) = 0. \tag{A.4}$$

Since the $\phi$ dependent term is isolated in the sum, we can assume that term to

be constant with some $m$,

$$\left(\frac{1}{\Phi}\frac{d^2\Phi}{d\phi^2}\right) = -m^2. \tag{A.5}$$

The solutions to this can be given as,

$$\Phi(\phi) = A_m e^{im\phi}. \tag{A.6}$$

Plugging this in Eq. (A.4),

$$\left(\frac{r^2}{R}\frac{d^2R}{dr^2} + \frac{2r}{R}\frac{dR}{dr}\right) + \frac{1}{\sin^2(\theta)}\left(\frac{\sin(2\theta)}{2\Theta}\frac{d\Theta}{d\theta} + \frac{\sin^2(\theta)}{\Theta}\frac{d^2\Theta}{d\theta^2}\right) = 0. \tag{A.7}$$

Since the radial portion must also be constant for some $l$,

$$\left(\frac{r^2}{R}\frac{d^2R}{dr^2} + \frac{2r}{R}\frac{dR}{dr}\right) = l(l+1). \tag{A.8}$$

This Euler differential equation can be solved in a power series expansion and the solutions are known to be of the form,

$$R(r) = A_l r^l + B_l r^{-l-1}. \tag{A.9}$$

Plugging this into Eq. (A.7),

$$\frac{d^2\Theta}{d\theta^2} + \cot(\theta)\frac{d\Theta}{d\theta} + \left[l(l+1) - \frac{m^2}{\sin^2(\theta)}\right]\Theta = 0. \tag{A.10}$$

This is the associated Legendre differential equation and the solutions are known to be,

$$\Theta(\theta) = P_l^m(\cos(\theta)), \tag{A.11}$$

where the $P_l^m$ functions are the associated Legendre polynomials with $l =$

$0...\infty$ and $m = -l...l$.

The final solution can be expressed in terms of the complex spherical harmonics $Y_l^m(\theta,\phi) = P_l^m(\cos(\theta))e^{-im\phi}$ as,

$$V(r,\theta,\phi) = \sum_{l=0}^{\infty}\sum_{m=-l}^{m=l}\left(A_l r^l + B_l r^{-l-1}\right) Y_l^m(\theta,\phi). \tag{A.12}$$

## A.2 Laplace equation in Cylindrical coordinates

The Laplace equation can be solved in cylindrical coordinates similar to the spherical coordinate solution. The Laplace equation is exactly separable in cylindrical coordinates $(r,\theta,z)$. The Laplace operator in cylindrical coordinates can be given as,

$$\nabla^2 = \frac{1}{r}\frac{\partial}{\partial r}\left(r\frac{\partial}{\partial r}\right) + \frac{1}{r^2}\frac{\partial^2}{\partial\phi^2} + \frac{\partial^2}{\partial z^2}. \tag{A.13}$$

Similar to the spherical coordinates, assuming a solution of the form,

$$V = R(r)\Phi(\phi)Z(z), \tag{A.14}$$

we can expand the equation and derive three independent differential equations for each of the three variables,

$$\left(\frac{1}{\Phi}\frac{d^2\Phi}{d\phi^2}\right) = -m^2. \tag{A.15}$$

$$\left(\frac{1}{Z}\frac{d^2Z}{dz^2}\right) = k^2. \tag{A.16}$$

$$\frac{d^2R}{dr^2} + \frac{1}{r}\frac{dR}{dr} + \left[k^2 - \frac{m^2}{r^2}\right]R = 0. \tag{A.17}$$

All three of these differential equations are well-known in differential equation literature. The first equation has the solution,

$$\Phi(\phi) = A_m e^{im\phi}, \tag{A.18}$$

for integer $m$, while the second equation has,

$$Z = \sinh(kz). \tag{A.19}$$

The third equation is the well-known Bessel's equation with the Bessel functions $J_m(kr)$ as the solutions. Hence the general solution of the Laplace potential can be expressed as,

$$V(r, \phi, z) = \sum_{m=-\infty}^{\infty} A_m J_m(kr) e^{im\phi}. \tag{A.20}$$

## A.3 Laplace equation in Toroidal coordinates

The Laplace equation is only approximately separable in toroidal coordinates. We do not give the derivation here. The potential function can be expressed as,

$$\Phi(\xi, \eta, \phi) = \sqrt{1 - \xi\cos(\eta)} \sum_{m,n} \left\{ \begin{array}{c} T_{mn} \\ S_{mn} \end{array} \right\} \times \left\{ \begin{array}{c} \cos(m\eta) \\ \sin(m\eta) \end{array} \right\} \times \left\{ \begin{array}{c} \cos(n\phi) \\ \sin(n\phi) \end{array} \right\}, \tag{A.21}$$

where $T_{mn} = \xi^{-1/2} Q^n_{m-1/2}(1/\xi)$ and $S_{mn} = \xi^{-1/2} P^n_{m-1/2}(1/\xi)$ with $Q^\alpha_\beta$ and $P^\alpha_\beta$ as the associate Legendre functions. The curly braces indicate that any one of the functions within may be chosen to form a valid mode.

# Appendix B
# The toroidal coordinate system

## B.1 Transformation equations for toroidal coordinates

The toroidal coordinates and the natural coordinates can be depicted as shown in Fig. 5.2. The transformation equations from the toroidal coordinates $(x, y, z)$ to toroidal coordinates $(\xi, \eta, \phi)$ can be given as,

$$x = \frac{r_0\sqrt{1-\xi^2}\cos(\phi)}{1-\xi\cos(\eta)}, \tag{B.1a}$$

$$y = \frac{r_0\sqrt{1-\xi^2}\cos(\phi)}{1-\xi\sin(\eta)}, \tag{B.1b}$$

$$z = \frac{-r_0\xi\sin(\eta)}{1-\xi\cos(\eta)}. \tag{B.1c}$$

The inverse transformation can be given as,

$$\phi = \arctan\frac{y}{x}, \tag{B.2a}$$

$$\xi = \frac{2d_1d_2}{d_1^2+d_2^2}, \tag{B.2b}$$

$$\eta = \arccos\frac{d_1^2+d_2^2-4r^2}{2d_1d_2}, \tag{B.2c}$$

where $d_1^2 = (\rho+r)^2+z^2$, $d_2^2 = (\rho-r)^2+z^2$ and $\rho^2 = x^2+y^2$.

## B.2 The scale factors

The scale factors for the orthogonal toroidal coordinates can be given as,

$$h_\xi = \frac{r_0}{\sqrt{1-\xi^2}(1-\xi\cos(\eta))}, \tag{B.3a}$$

$$h_\eta = \frac{r_0\xi}{1-\xi\cos(\eta)}, \tag{B.3b}$$

$$h_\phi = \frac{r_0\sqrt{1-\xi^2}}{(1-\xi\cos(\eta))}. \tag{B.3c}$$

## B.3 The normal vector

The normal vectors to the surfaces of constant $\xi$ can be given by,

$$\mathbf{n} = \left\{ \frac{(\cos(\eta)-\xi)\cos(\phi)}{1-\xi\cos(\eta)}, \frac{(\cos(\eta)-\xi)\sin(\phi)}{1-\xi\cos(\eta)}, -\frac{\sqrt{1-\xi^2}\sin(\eta)}{1-\xi\cos(\eta)} \right\}. \tag{B.4}$$

## B.4 The inverse distance

The inverse distance between two points on a surface of constant $\xi$ is,

$$\frac{1}{|\mathbf{x_1}-\mathbf{x_2}|} = \frac{1}{\sqrt{2}r_0}\sqrt{\frac{(1-\xi\cos(\eta_1))(1-\xi\cos(\eta_2))}{1-\xi^2\cos(\eta_1-\eta_2)-(1-\xi^2)\cos(\phi_1-\phi_2)}}. \tag{B.5}$$

# Appendix C

# Computational techniques for solving large systems of coupled differential equations

As we saw in the main text, the main problem to be solved in the quantum description of coupled nano-resonator-gain systems can be formulated in the form of a set of coupled first order differential equations,

$$\dot{\hat{\mathcal{Q}}} = A\hat{\mathcal{Q}}. \tag{C.1}$$

Here, $\hat{\mathcal{Q}}$ is the linearised density matrix of the system. As mentioned in the text, the density matrix has size $4^N \times M^2$, where $N$ is the number of gain media chromophores and $M$ is the resonator mode cut-off. $A$ is a large, sparse, Hermitian matrix with constant, complex coefficients. The main objective is to solve for the steady state of the density matrix, given the evolution as dictated by $A$. In this appendix, we shall present some of the computational techniques available in literature for handling such large systems.

## C.1 Differential equations solution method

The most obvious technique we can use is the classical theory of numerical differential equations. This method is not specialised for the quantum domain and

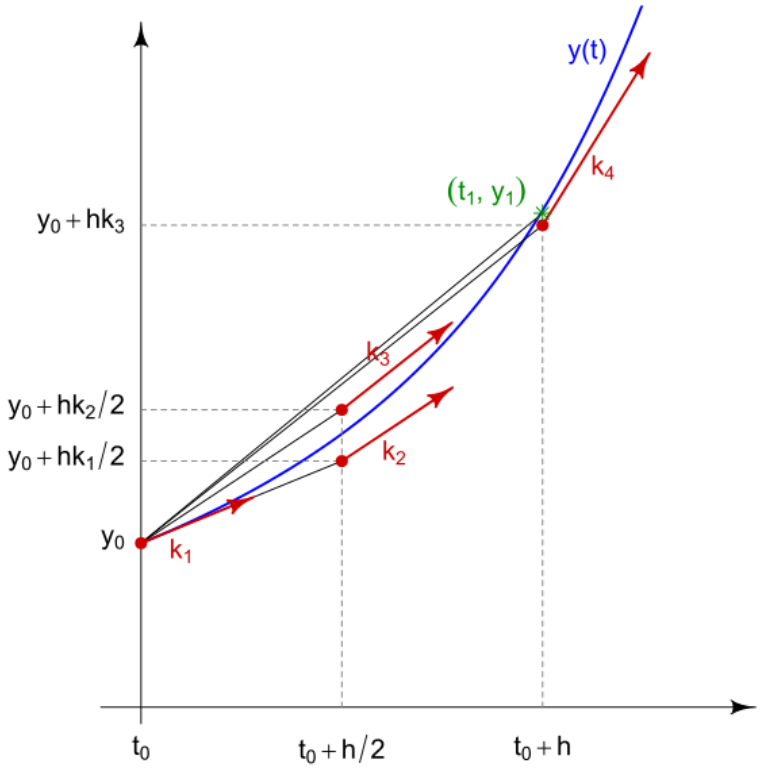


Figure C.1: An illustration of the order 4 Runge-Kutta method. Image available under the Creative Commons Attribution-Share Alike 4.0 International license.

can be freely used to solve such equations. We use such a scheme in the solver we devised. Runge-Kutta schemes are perhaps the most widely used among the methods used to solve differential equations and among these schemes, the order 4 Runge-Kutta algorithm is perhaps the most widely used. This method is illustrated in Fig. C.1. Using the initial value of the function at $t_0$, the value of the function at $t_0 + h$ is built up using the derivatives(slopes) at 4 intermediate points as labelled by $k_i$ where $i = 1 - 4$. Each step of the algorithm requires the evaluation of the derivative 4 times, which signifies the order of the Runge Kutta scheme. In such schemes, the step size is an arbitrary factor as determined by the user. The accuracy of the estimate of the function crucially depends on the size of the step and behaviour of the function near the estimation points. Hence, choosing a proper step-size is a somewhat important yet hard problem in Runge-Kutta schemes. There exists a special class of Runge-Kutta schemes that uses an internal error prediction to choose an appropriate step size internally. Such methods are termed adpative Runge-Kutta schemes and we use one of the adaptive schemes in our quantum solver. More information on adaptive Runge-Kutta schemes can be found in Appendix E.

## C.2 Linear algebra based solutions

Yet another method for solving Eq. (C.1) is to use the classical theory of linear algebra. The steady state solution implies,

$$\dot{\hat{\mathcal{Q}}} = 0. \tag{C.2}$$

This means that we need to find the density matrices $\hat{\mathcal{Q}}$ such that,

$$A\hat{\mathcal{Q}} = 0. \tag{C.3}$$

But the solution to this is furnished exactly by the null space of the matrix $A$. There exist many convenient algorithms and software for finding the null space of large sparse matrices [72]. Most of these involve one of the well-known decompositions like the QR-decomposition and the LU-decomposition.

A similar and related formulation of the problem is in terms of the eigenvalues of matrix $A$. The null space of the matrix is formed exactly by those eigenfunctions that have eigenvalue 0.

$$A\hat{\mathcal{Q}} = 0\hat{\mathcal{Q}}. \tag{C.4}$$

This problem can be solved by so-called Krylov-Schur algorithms [73] that can compute the eigenfunctions of asymmetric matrices near a specific eigenvalue.

The main drawback in this scheme is that the null space of $A$ could in general be multidimensional and hence we would need to choose the solution eigenvector corresponding to our initial conditions. This would impose an extra processing burden on solvers.

## C.3 Monte Carlo Simulation

Another, yet more specialised method of handling Eq. (C.1) is a Monte-Carlo method based on a probabilistic understanding of quantum states. We present a very simplified form here.

Start with the initial state vector of the system. Note that we do not start with an initial density matrix similar to the earlier methods. Hence the overall size of the problem is only $O(2^N \times M)$. This is a significant reduction is complexity to begin with. Next, we evolve the matrix according to the laws of continuous Hamiltonian evolution and the laws of random wave-function collapse as dictated by the Lindblad operators. While the Hamiltonian evolution is deterministic, the Lindblad evolution is stochastic, resulting in a different end state

vector in different runs of the algorithm. The algorithm can hence be run on the same initial vector multiple times resulting in a collection of possible end states. These end states can then be interpreted as samples from the possible statistical mixtures arising within the system at steady state. Hence, the mean values of the state vectors actually form the final state vector as expected from quantum evolution. The solution of Eq. (C.1) using this method has been implemented in solvers such as QuTiP [74].

# Appendix D

# Computational paradigms for solving quantum systems

An important concern in solving quantum master equations is the computational paradigm used. Smaller problems may utilise a single computer with one or few computational cores. Larger scale problems may require a more specialised computer with many nodes or many interconnected computers with multiple cores inside each. Another possible alternative is the use of Graphics Processing Units(GPUs) and the many specialised cores they offer.

## D.1 Single core computing

This form of computation is the direct, linear type of computation that utilises a single processing core. It is the simplest to understand and write code for. Most computations run on personal workstations would belong to this type of computation unless the software is explicitly specialised to use available multiple cores. The key feature in these types of computations is the existence of a single processor and a single memory system. Writing code for such systems is the simplest of all paradigms, and the code is executed serially.

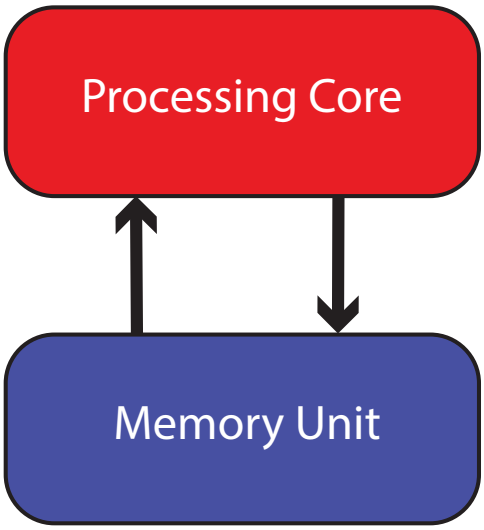


Figure D.1: The single core processing architecture. A single processing unit interacts with a single memory unit.

## D.2 Multi-core computing

In this method, the workload of computation is distributed among many workers(or cores) that jointly handle the computational load in parallel. They work on sub-problems of the initial problem and combine the answers to come up with the final answer. Based on the complexity of the problem, this type of paradigm requires attention to be paid to the inter-dependency between the operations performed by each of the workers and questions regarding the synchronisation of workers. Depending on the architecture of the memory system, multi-core systems are broadly divided into two categories.

- Shared-memory parallelism
- Distributed-memory parallelsim

In shared memory architecture, all of the workers share a common memory system and hence has simultaneous access to the memory space. Such a collection is usually referred to as a node. This allows the workers to perform operations on the same data without need of communication between them. This type of

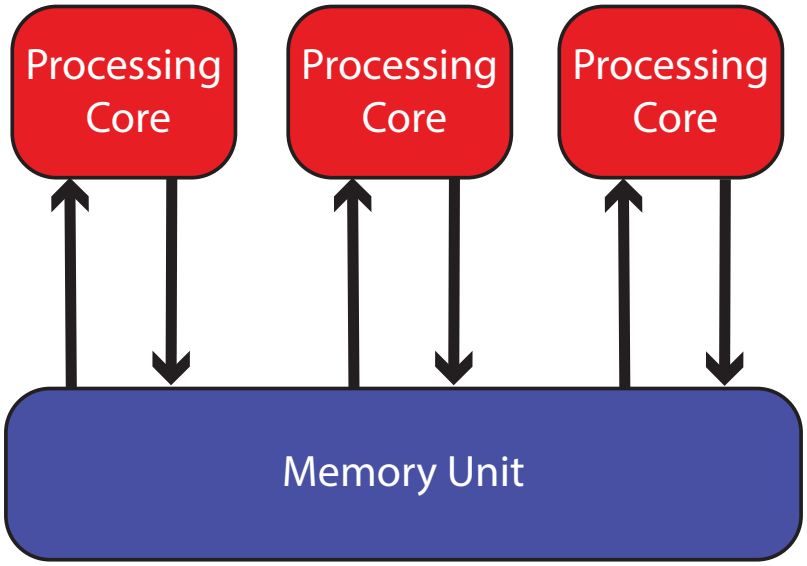


Figure D.2: A shared-memory parallelism architecture. Multiple cores operate independently of each other but share the same memory space.

parallelism is useful when the problem being solved has a computationally taxing operation that can be easily divided into non-overlapping sub-computations. The main downside of such systems s the fact that the sizes of problems solved is limited by both the number of workers that share a common memory space, and by the maximum memory available to all the worker. We use this paradigm in our quantum solver. An application programming interface allows users of such systems to transform serial code to shared-memory parallelised code. OpenMP is the most commonly used application programming interface to distribute computational work in such systems.

In distributed memory architecture, groups of workers have access to different memory spaces. The computational system is composed of mutiple nodes. This allows the computation to use as many workers as needed while adding as much memory as needed. Hence, there is no memory or worker limitations in this model. However, since the memory is not shared, it requires the explicit passing of information between workers in different groups to keep track of changes

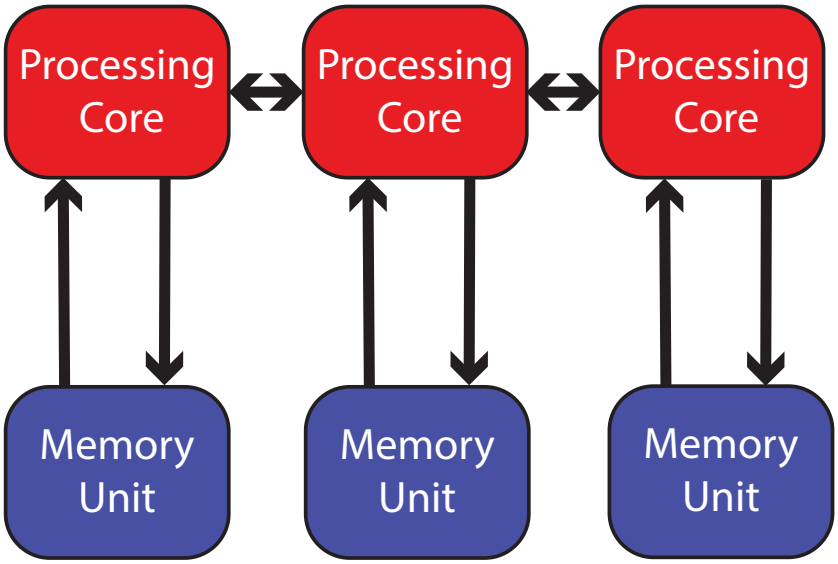


Figure D.3: A distributed-memory parallelism architecture. Multiple cores with their own memory units operate independently on sub-computations, with message passing between them to synchronise their operation.

taking place in other groups. This takes up a certain amount of computational time and may also lead to workers remaining idle waiting for responses from other workers. OpenMPI is an example of an application programming interface used to perform the communication between workers in a distributed memory system.

A majority of the software designed to handle various quantum systems are usually bolstered with the option to use either shared or distributed memory parallelised computing architectures [60,74].

## D.3 Many-core computing and GPUs

Many-core computing uses infrastructure designed specially and exclusively for parallel processing and has specialised circuitry and interconnections to allow for fast communication between workers. They also possess an extremely large num-


Figure D.4: A popular Graphical Processing Unit circuit.

ber of workers sharing a single circuit board. Graphics Processing Units(GPUs) are possibly the most popular variant of this type of system. Used to perform extremely complex calculations especially in the video image rendering space, GPUs have become a staple in many High Performance Computing(HPC) systems. The main downside of using such many-core systems is the need for extremely specialised design of software for solving problems, depending not only on the problem but also on the hardware platform being used.

# Appendix E
# Elements of the quantum solver

## E.1 Compressed Sparse Row(CSR) encoding

We used the CSR encoding scheme to efficiently store the sparse Jacobian matrix $A$. This storage scheme allowed a straightforward way to implement Matrix-Vector multiplication to calculate the derivative values as well as to parallelise the multiplication.

The CSR scheme takes an $n \times m$ sparse matrix $A$ and defines 3 separate vectors to represent the data within the matrix.

- $DataA$ - a vector containing all the non-zero elements of $A$ in row-major order
- $IA$ - a vector of length $(n+1)$, with $IA[i]$ indicating the index within $DataA$, of the first non-zero element in the $i^{th}$ row of $A$.
- $JA$ - a vector indicating the column index of each element in $DataA$

For example, consider the following matrix,

$$A = \begin{bmatrix} 0 & 0 & 0 & 0 & 0 \\ 0 & 5 & 0 & 9 & 0 \\ 0 & 0 & 3 & 0 & 0 \\ 0 & 8 & 0 & 7 & 0 \\ 0 & 0 & 6 & 0 & 0 \end{bmatrix}$$

.

This transforms into the following form in the CSR scheme,

$$DataA = \begin{bmatrix} 5 & 9 & 3 & 8 & 7 & 6 \end{bmatrix}$$
$$IA = \begin{bmatrix} 0 & 0 & 2 & 3 & 5 & 6 \end{bmatrix}$$
$$JA = \begin{bmatrix} 1 & 3 & 2 & 1 & 3 & 2 \end{bmatrix}$$

## E.2 Runge-Kutta Cash-Karp scheme

We used an adaptive Runge-Kutta scheme to solve the differential equation of our quantum solver. Adaptive Runge-Kutta schemes are superior to the regular Runge-Kutta schemes in that they contain an in-built mechanism to correct errors and adjust the step size depending on the error. The basic idea in each adaptive Runge-Kutta scheme can be illustrated by considering the following. Given the derivative of a function $\dot{y} = f(x, y)$, and the value of the function at some point $y(x_0) = y_0$, to estimate the value of the function at $x_0 + h$, we take two distinct routes.

In the first route, we calculate the function value at $x_0 + h$ using Euler's formula as,

$$y_1 = y(x_0 + h) = y_0 + f(x_0 + y_0) \times h. \tag{E.1}$$

In the second route,

$$y_2 = y(x_0 + h) = y_0 + f\left(x_0 + \frac{h}{2} + y_0 + \frac{hf(x_0, y_0)}{2}\right) \times h. \tag{E.2}$$

$y_1$ is a first order approximation while $y_2$ is a second order approximation. Since $y_2$ is more accurate an estimate as compared to $y_1$, we can use $(y_1 - y_2)$

as an estimate for the error of the integration. Using this, we can either decide to increase the step size $h$ or decrease it, depending on whether the error is less than our tolerance or greater. While this simple order $1-2$ method is not used in practice, it is the basis for all adaptive Runge-Kutta methods. We use the order $4-5$ Cash-Karp Runge-Kutta scheme. While in general this method would require $4+5=9$ derivative function evaluations, the Cash-Karp method has been designed to have overlapping intermediate derivative so that a single Cash-Karp estimate may be performed with only 6 evaluations of the derivative function. This is important to us, since the derivative evaluation portion of our algorithm involves a large matrix-vector multiplication which actually forms the bottleneck of our quantum solver. Further information regarding alternatives to the Runge-Kutta scheme are discussed in Appendix C

## E.3 Reverse Cuthill-McKee algorithm

The reverse Cuthill-McKee algorithm is useful in reducing the so-called bandwidth of square matrices. This is especially useful when a large a matrix multiplication needs to be distributed among different processors in order to make the multiplication more efficient. The reordering results in bringing the non-zeros elements of a matrix closer to the diagonal and operates by changing the order in which variables appear in the rows and columns of the matrix. This results in only a minimal amount of communication being needed between processors in order to perform the multiplications independently. The algorithm for a matrix $A$ is presented below.

**Algorithm 4** Reverse Cuthill-McKee algorithm

**procedure** RCM($A$) ▷ Calculate a reordering of $A$ to reduce bandwidth
    $Q \leftarrow$ empty queue
    $L \leftarrow$ array of zeros with length equal to number of rows
    $index \leftarrow 1$
    $D \leftarrow$ degree(number of non-zero elements) for each row
    **do**
        $I \leftarrow$ row index with min degree $D$, such that $L[I] = 0$
        $L[I] = index$
        $index = index + 1$
        $Q \leftarrow$ column indices of non-zero elements in row $I$, in order of increasing degree
        **do**
            $J \leftarrow Q$ pop from $Q$
            **if** R[J]=0 **then**
                $L[J] = index$
                $index = index + 1$
                $Q \leftarrow$ column indices of non-zero elements in row $J$, in order of increasing degree
            **end if**
        **while** $Q$ is non-empty
    **while** $L[K] = 0$ for some $K$
    $S \leftarrow$ indices of $L$ in reverse order of $L[.]$
    **return** $S$ ▷ Final ordering of the rows
**end procedure**

## E.4 Parallelised Matrix-Vector multiplication

The main bottleneck of the quantum solver for many-emitter nanoresonator systems was the matrix multiplication between the linearized density matrix vector $\hat{\mathcal{Q}}$ and the Jacobian matrix $A$. Due to this, an efficient multiplication strategy was needed that utilised multiple cores to improve the efficiency of the computation. Fortunately, due to CSR representation we used to store the matrix $A$, the parallelisation scheme was straightforward. Below, we give the algorithm for parallelising the multiplication. Matrix $A$ has dimensions $(n \times m)$.

**Algorithm 5** Multiplier($A$,$\hat{\mathcal{Q}}$)

**procedure** MULTIPLY($DataA$, $IA$, $JA$, $V$) ▷ Calculate multiplication between matrix $A$ in CSR form and vector $V$
    $Result \leftarrow$ vector of zeros
    **for** $i$=0 to $n-1$ **do** ▷ The outer loop will be executed in parallel
        $Result[i] \leftarrow 0$
        **for** $j$=$IA[i]$ to $IA[i+1]-1$ **do**
            $Result[i] \leftarrow Result[i] + V[j] \times DataA[JA[j]]$
        **end for**
    **end for**
    **return** $Result$ ▷ The final result
**end procedure**

## E.5 Computational infrastructure

The algorithms of the solver were implemented in C++. The solver was run on Raijin, the premier supercomputing cluster of the Australian National Computing Infrastructure(NCI), through a National computational Merit Allocation Scheme(NCMAS) grant awarded for the year 2018. The solver was designed to run on a system of two Xeon E5-2690v4(Broadwell) processors comprising of 28 total cores. The processor speed was at 2.6 GHz and consisted of 256 GB of shared memory. We used shared-memory parallelism and the OpenMP framework for

implementing parallelised elements. Further discussion on the various possible parallelisation schemes is available in Appendix D.

# Appendix F
# Resonance frequency of a transverse dimer

## F.1 Resonance frequency for a general Drude material

We derived the localised time domain electric field for a dimer under the assumptions of $\epsilon_b = \epsilon_{\text{core}} = 1$ in the main text Eq. (4.13). We now show that a similar form holds for general $\epsilon_b$ and $\epsilon_{\text{core}}$ values.

To begin, we first consider the polarizability of an isolated nanosphere. Using the Drude model as given in Eq. (4.10),

$$\begin{aligned} \alpha &= \frac{\epsilon_m - \epsilon_b}{(\epsilon_m - \epsilon_b)} \\ &= \frac{\epsilon_{\text{core}} - \epsilon_b - \frac{\omega_p^2}{\omega(\omega + i\gamma_0)}}{\epsilon_{\text{core}} + 2\epsilon_b - \frac{\omega_p^2}{\omega(\omega + i\gamma_0)}}. \end{aligned} \tag{F.1}$$

Setting $y = \epsilon_{\text{core}} - \epsilon_b$, we can rewrite this as,

$$\begin{aligned} \alpha &= \frac{y}{y + 3\epsilon_b} \frac{\omega^2 y + i\omega\gamma_0 y - \omega_p^2}{\omega^2(y + 3\epsilon_b) + i\omega\gamma_0(y + 3\epsilon_b) - \omega_p^2} \\ &= \frac{y}{y + 3\epsilon_b} - \frac{3\epsilon_b}{y + 3\epsilon_b} \frac{\omega_F^2}{\omega^2 - \omega_F^2 + i\omega\gamma_0}. \end{aligned} \tag{F.2}$$

Here we have defined $\omega_F = \frac{\omega_p}{\sqrt{y+3\epsilon_b}}$ to be the generalized Fröhlich frequency for the case of general core permittivity values of the metal. This can be further simplified using the approximation $\omega \sim \omega_F \gg \gamma_0$,

$$\begin{aligned} \alpha \quad &\approx \frac{y}{y+3\epsilon_b} - \frac{3\epsilon_b}{y+3\epsilon_b}\frac{\omega_F^2}{2\omega(\omega-\omega_F)+i\omega\gamma_0} \\ &\approx \frac{y}{y+3\epsilon_b} - \frac{3\epsilon_b}{y+3\epsilon_b}\frac{\omega_F/2}{\omega-(\omega_F-i\gamma_0/2)}. \end{aligned} \tag{F.3}$$

Thus the total electric field for the singlet sphere can be written using the single source Green's dyadic $\mathbf{G}(\mathbf{r};\mathbf{r}_1)$ as,

$$\mathbf{E}_{\text{sing}}(\mathbf{r},\omega) = \frac{1}{y+3\epsilon_b}\left(y - \frac{3\epsilon_b\omega_F/2}{\omega-(\omega_F-i\gamma_0/2)}\right)\mathbf{G}(\mathbf{r};\mathbf{r}_1). \tag{F.4}$$

In the time domain, for $t > 0$, we take the Fourier Transform to give,

$$\mathbf{E}_{\text{sing}}(\mathbf{r},t) = \frac{3\epsilon_b}{\epsilon_{\text{core}}+2\epsilon_b}\frac{\omega_F E_0}{2}\mathbf{G}(\mathbf{r};\mathbf{r}_1)\sin(\omega_F t)e^{-\gamma_0 t/2}. \tag{F.5}$$

This predicts a system with resonance frequency $\omega_F$ and dissipation parameter $\gamma_0$.

Next we derive the electric field of the transverse dimer. We start by considering the effective polarizability $\alpha_{\text{eff}}$. Using the frequency domain electric field from Eq. (4.9) and the Drude model as given by Eq. (4.10),

$$\alpha_{\text{eff}} \quad = \frac{\epsilon_m-\epsilon_b}{(\epsilon_m-\epsilon_b)(1+\frac{R^3}{D^3})+3\epsilon_b}. \tag{F.6}$$

Next we use the substitutions $\kappa = 1+\frac{R^3}{D^3}$ and $y = \epsilon_{\text{core}} - \epsilon_b$. We note that by the physical restrictions, $D > 2R$ and hence, $\kappa < 1.125$. Now we can simplify the earlier expression as,

$$\alpha_{\text{eff}} = \frac{y}{y\kappa + 3\epsilon_b} - \frac{3\epsilon_b}{\kappa y + 3\epsilon_b} \frac{\omega_F^2}{\omega^2 - \omega_0^2 + i\omega\gamma_0}. \tag{F.7}$$

Here we have used the approximation $\kappa \approx 1$, to write $\frac{\omega_p}{\sqrt{\kappa y + 3\epsilon_b}} \approx \frac{\omega_p}{\sqrt{y + 3\epsilon_b}} = \omega_F$ and also defined $\omega_0 = \omega_p \sqrt{\frac{\kappa}{\kappa y + 3\epsilon_b}}$. Using the usual approximations, $\omega \sim \omega_F \sim \omega_0 \gg \gamma_0$ which are valid for small resonance frequency shifts from the Fröhlich frequency $\omega_F$, we can write,

$$\begin{aligned} \alpha_{\text{eff}} &\approx \frac{y}{\kappa y + 3\epsilon_b} - \frac{3\epsilon_b}{\kappa y + 3\epsilon_b} \frac{\omega_F^2}{2\omega(\omega - \omega_0) + i\omega\gamma_0} \\ &\approx \frac{y}{\kappa y + 3\epsilon_b} - \frac{3\epsilon_b}{\kappa y + 3\epsilon_b} \frac{\omega_F/2}{\omega - (\omega_0 - i\gamma_0/2)}. \end{aligned} \tag{F.8}$$

This gives the electric near field of the transverse dimer as,

$$\mathbf{E}_{\text{dim}}^{\text{tr}}(\mathbf{r}, \omega) = \alpha_{\text{eff}}[\mathbf{G}(\mathbf{r}; \mathbf{r}_1) + \mathbf{G}(\mathbf{r}; \mathbf{r}_2)]. \tag{F.9}$$

In the time domain, for $t > 0$, we find,

$$\mathbf{E}_{\text{dim}}^{\text{tr}}(\mathbf{r}, t) = \frac{3\epsilon_b \omega_F E_0/2}{\kappa y + 3\epsilon_b}[\mathbf{G}(\mathbf{r}; \mathbf{r}_1) + \mathbf{G}(\mathbf{r}; \mathbf{r}_2)] \sin(\omega_0 t) e^{-\gamma_0 t/2}. \tag{F.10}$$

This is exactly a resonant system with resonance frequency,

$$\begin{aligned} \omega_0 &= \omega_p \sqrt{\frac{\kappa}{\kappa y + 3\epsilon_b}} \\ &= \sqrt{1 + \frac{R^3}{D^3}} \frac{\omega_p}{\sqrt{\kappa y + 3\epsilon_b}} \\ &\approx \sqrt{1 + \frac{R^3}{D^3}} \omega_F. \end{aligned} \tag{F.11}$$

# Bibliography


[1] Fakonas, J. S., Lee, H., Kelaita, Y. A. & Atwater, H. A. Two-plasmon quantum interference. *Nature Photonics* **8**, 317–320 (2014).

[2] Andersen, M. L., Stobbe, S., Sørensen, A. S. & Lodahl, P. Strongly modified plasmon–matter interaction with mesoscopic quantum emitters. *Nature Physics* **7**, 215–218 (2011).

[3] De Leon, N. P., Lukin, M. D. & Park, H. Quantum plasmonic circuits. *IEEE Journal of Selected Topics in Quantum Electronics* **18**, 1781–1791 (2012).

[4] Barnes, W. L., Dereux, A. & Ebbesen, T. W. Surface plasmon subwavelength optics. *nature* **424**, 824–830 (2003).

[5] Hatef, A., Sadeghi, S. M., Boulais, É. & Meunier, M. Quantum dot–metallic nanorod sensors via exciton–plasmon interaction. *Nanotechnology* **24**, 015502 (2012).

[6] Scholl, J. A., Koh, A. L. & Dionne, J. A. Quantum plasmon resonances of individual metallic nanoparticles. *Nature* **483**, 421 (2012).

[7] Sothmann, B., Sánchez, R. & Jordan, A. N. Thermoelectric energy harvesting with quantum dots. *Nanotechnology* **26**, 032001 (2014).

[8] Jin, S. *et al.* Distance-engineered plasmon-enhanced light harvesting in cdse quantum dots. *The Journal of Physical Chemistry Letters* **4**, 3527–3533 (2013).

[9] Ritchie, R. H. Plasma losses by fast electrons in thin films. *Physical review* **106**, 874 (1957).

[10] Gwon, H. R. & Lee, S. H. Spectral and angular responses of surface plasmon resonance based on the kretschmann prism configuration. *Materials transactions* **51**, 1150–1155 (2010).

[11] Kravets, V., Kabashin, A., Barnes, W. & Grigorenko, A. Plasmonic surface lattice resonances: a review of properties and applications. *Chemical reviews* **118**, 5912–5951 (2018).

[12] Mie, G. Beiträge zur optik trüber medien, speziell kolloidaler metallösungen. *Annalen der physik* **330**, 377–445 (1908).

[13] Neumann, C. *Über die methode des arithmetischen mittels...*, vol. 13 (S. Hirzel, 1887).

[14] Poincaré, H. *et al.* La méthode de neumann et le probleme de dirichlet. *Acta mathematica* **20**, 59–142 (1897).

[15] Mayergoyz, I. D., Fredkin, D. R. & Zhang, Z. Electrostatic (plasmon) resonances in nanoparticles. *Physical Review B* **72**, 155412 (2005).

[16] Yurtsever, A., van der Veen, R. M. & Zewail, A. H. Subparticle ultrafast spectrum imaging in 4d electron microscopy. *Science* **335**, 59–64 (2012).

[17] Enoch, S., Quidant, R. & Badenes, G. Optical sensing based on plasmon coupling in nanoparticle arrays. *Optics express* **12**, 3422–3427 (2004).

[18] Nordlander, P., Oubre, C., Prodan, E., Li, K. & Stockman, M. Plasmon hybridization in nanoparticle dimers. *Nano letters* **4**, 899–903 (2004).

[19] Jiang, Y., Pillai, S. & Green, M. A. Realistic silver optical constants for plasmonics. *Scientific reports* **6**, 30605 (2016).

[20] Johnson, P. B. & Christy, R.-W. Optical constants of the noble metals. *Physical review B* **6**, 4370 (1972).

[21] Jackson, J. D. *Classical Electrodynamics* (John Wiley & Sons, 1975).

[22] Waks, E. & Sridharan, D. Cavity qed treatment of interactions between a metal nanoparticle and a dipole emitter. *Physical Review A* **82**, 043845 (2010).

[23] Premaratne, M. & Stockman, M. I. Theory and technology of spasers. *Advances in Optics and Photonics* **9**, 79–128 (2017).

[24] Landau, L. D. *et al. Electrodynamics of continuous media*, vol. 8 (elsevier, 2013).

[25] Bohren, C. F. & Huffman, D. R. *Absorption and scattering of light by small particles* (John Wiley & Sons, 2008).

[26] Davis, T. J., Vernon, K. C. & Gómez, D. E. Designing plasmonic systems using optical coupling between nanoparticles. *Phys. Rev. B* **79**, 155423 (2009). URL `https://link.aps.org/doi/10.1103/PhysRevB.79.155423`.

[27] Aizpurua, J. *et al.* Optical properties of gold nanorings. *Physical review letters* **90**, 057401 (2003).

[28] Mary, A., Dereux, A. & Ferrell, T. L. Localized surface plasmons on a torus in the nonretarded approximation. *Physical Review B* **72**, 155426 (2005).

[29] Safford, F. Solution of laplace's equation in toroidal coördinates deduced by a method of imaginary inversion. *The Annals of Mathematics* **12**, 27–32 (1898).

[30] Love, J. D. Quasi-static modes of oscillation of a cold toroidal plasma. *Journal of Plasma Physics* **14**, 25–37 (1975).

[31] Avramov, K., Ivanov, T. & Zhelyazkov, I. High-frequency surface waves on a toroidal isotropic plasma. *Plasma physics and controlled fusion* **35**, 1787 (1993).

[32] Salhi, M. *Surface Plasmon Modes in Toroidal Nanostructures and Applications*. Ph.D. thesis, University of Tennessee, Knoxville (2016).

[33] Garapati, K. V., Salhi, M., Kouchekian, S., Siopsis, G. & Passian, A. Poloidal and toroidal plasmons and fields of multilayer nanorings. *Physical Review B* **95**, 165422 (2017).

[34] Dutta, C. M., Ali, T. A., Brandl, D. W., Park, T.-H. & Nordlander, P. Plasmonic properties of a metallic torus. *The Journal of chemical physics* **129**, 084706 (2008).

[35] Ando, K., Ji, Y.-G., Kang, H., Kawagoe, D. & Miyanishi, Y. Spectral structure of the neumann–poincaré operator on tori. In *Annales de l'Institut Henri Poincaré C, Analyse non linéaire* (Elsevier, 2019).

[36] Bates, J. W. On toroidal green's functions. *Journal of Mathematical Physics* **38**, 3679–3691 (1997).

[37] Ji, Y.-G. & Kang, H. A concavity condition for existence of a negative value in neumann-poincaré spectrum in three dimensions. *Proceedings of the American Mathematical Society* **147**, 3431–3438 (2019).

[38] Hohenester, U. & Trügler, A. Mnpbem–a matlab toolbox for the simulation of plasmonic nanoparticles. *Computer Physics Communications* **183**, 370–381 (2012).

[39] Lozovik, Y. E., Nechepurenko, I. A., Dorofeenko, A. V., Andrianov, E. S. & Pukhov, A. A. Spaser spectroscopy with subwavelength spatial resolution. *Physics Letters A* **378**, 723–727 (2014).

[40] Galanzha, E. I. *et al.* Spaser as a biological probe. *Nature communications* **8**, 15528 (2017).

[41] Rupasinghe, C., Rukhlenko, I. D. & Premaratne, M. Spaser made of graphene and carbon nanotubes. *ACS nano* **8**, 2431–2438 (2014).

[42] Sakurai, J. J. *Advanced quantum mechanics* (Pearson Education India, 1967).

[43] Dicke, R. H. Coherence in spontaneous radiation processes. *Physical Review* **93**, 99 (1954).

[44] Lindblad, G. On the generators of quantum dynamical semigroups. *Communications in Mathematical Physics* **48**, 119–130 (1976).

[45] Breuer, H.-P. & Petruccione, F. *The theory of open quantum systems* (Oxford University Press on Demand, 2002).

[46] Tavis, M. & Cummings, F. W. Exact solution for an n-molecule—radiation-field hamiltonian. *Physical Review* **170**, 379 (1968).

[47] Einwohner, T., Wong, J. & Garrison, J. Analytical solutions for laser excitation of multilevel systems in the rotating-wave approximation. *Physical Review A* **14**, 1452 (1976).

[48] Pagel, D., Alvermann, A. & Fehske, H. Nonclassical light from few emitters in a cavity. *Physical Review A* **91**, 043814 (2015).

[49] Milonni, P., Ackerhalt, J. & Galbraith, H. Chaos in the semiclassical n-atom jaynes-cummings model: Failure of the rotating-wave approximation. *Physical Review Letters* **50**, 966 (1983).

[50] Agarwal, G. Rotating-wave approximation and spontaneous emission. *Physical Review A* **4**, 1778 (1971).

[51] Zueco, D., Reuther, G. M., Kohler, S. & Hänggi, P. Qubit-oscillator dynamics in the dispersive regime: Analytical theory beyond the rotating-wave approximation. *Physical Review A* **80**, 033846 (2009).

[52] Richter, M., Gegg, M., Theuerholz, T. S. & Knorr, A. Numerically exact solution of the many emitter–cavity laser problem: Application to the fully quantized spaser emission. *Physical Review B* **91**, 035306 (2015).

[53] Sarkar, S. & Satchell, J. Optical bistability with small numbers of atoms. *EPL (Europhysics Letters)* **3**, 797 (1987).

[54] Carmichael, H. J. & Scully, M. O. Statistical methods in quantum optics 1: Master equations and fokker-planck equations. *Physics Today* **53**, 78 (2000).

[55] Hartmann, S. Generalized dicke states. *arXiv preprint arXiv:1201.1732* (2012).

[56] Zhang, Y. & May, V. Theory of molecule metal nano-particle interaction: Quantum description of plasmonic lasing. *The Journal of chemical physics* **142**, 224702 (2015).

[57] Zhang, Y. & Mølmer, K. Amplified emission and lasing in a plasmonic nanolaser with many three-level molecules. *Physical Review A* **97**, 013837 (2018).

[58] Cuthill, E. & McKee, J. Several strategies for reducing the bandwidth of matrices. *Sparse Matrices and Their Applications* **1**, 157–166 (1972).

[59] Dorfman, K. E. *et al.* Quantum-coherence-enhanced surface plasmon amplification by stimulated emission of radiation. *Physical review letters* **111**, 043601 (2013).

[60] Gegg, M. & Richter, M. Psiquasp–a library for efficient computation of symmetric open quantum systems. *arXiv preprint arXiv:1707.01079* (2017).

[61] Warnakula, T., Stockman, M. I. & Premaratne, M. Improved scheme for modeling a spaser made of identical gain elements. *JOSA B* **35**, 1397–1407 (2018).

[62] Khurgin, J. B. How to deal with the loss in plasmonics and metamaterials. *Nature nanotechnology* **10**, 2 (2015).

[63] Scully, M. O. & Zubairy, M. S. *Quantum Optics* (Cambridge University Press, 1997).

[64] Drude, P. Zur elektronentheorie der metalle. *Annalen der Physik* **306**, 566–613 (1900).

[65] Madoyan, K., Melikyan, A. & Minassian, H. Radiation damping of surface plasmons in a pair of nanoparticles and in nanoparticles near interfaces. *The Journal of Physical Chemistry C* **116**, 16800–16805 (2012).

[66] Dahmen, C., Schmidt, B. & von Plessen, G. Radiation damping in metal nanoparticle pairs. *Nano letters* **7**, 318–322 (2007).

[67] Marinica, D., Kazansky, A., Nordlander, P., Aizpurua, J. & Borisov, A. G. Quantum plasmonics: nonlinear effects in the field enhancement of a plasmonic nanoparticle dimer. *Nano letters* **12**, 1333–1339 (2012).

[68] Gnutzmann, S. Photon statistics of a bad-cavity laser near threshold. *The European Physical Journal D-Atomic, Molecular, Optical and Plasma Physics* **4**, 109–123 (1998).

[69] Warnakula, T., Gunapala, S. D., Stockman, M. I. & Premaratne, M. Cavity quantum electrodynamic analysis of spasing in nanospherical dimers. *Physical Review B* **100**, 085439 (2019).

[70] Kristensen, P. T., Ge, R.-C. & Hughes, S. Normalization of quasinormal modes in leaky optical cavities and plasmonic resonators. *Physical Review A* **92**, 053810 (2015).

[71] Chen, P. Y., Bergman, D. J. & Sivan, Y. Generalizing normal mode expansion of electromagnetic green's tensor to lossy resonators in open systems. *arXiv preprint arXiv:1711.00335* (2017).

[72] Hernandez, V., Roman, J. E. & Vidal, V. Slepc: A scalable and flexible toolkit for the solution of eigenvalue problems. *ACM Transactions on Mathematical Software (TOMS)* **31**, 351–362 (2005).

[73] Hernandez, V., Roman, J., Tomas, A. & Vidal, V. A survey of software for sparse eigenvalue problems. *Universidad Politecnica de Valencia, Valencia, Spain, SLEPc Technical Report STR-6, http://www. grycap. upv. es/slepc* (2009).

[74] Johansson, J. R., Nation, P. D. & Nori, F. Qutip 2: A python framework for the dynamics of open quantum systems. *Computer Physics Communications* **184**, 1234–1240 (2013).